THESIS APPROVAL

GRADUATE SCHOOL, KASETSART UNIVERSITY

Doctor of Engineering (Mechanical Engineering)

DEGREE

Mechanical Engineering — **FIELD**

Mechanical Engineering — **DEPARTMENT**

TITLE: Design of Humeral Nail based on Thai Morphometric Data

NAME: Mr. Panya Aroonjarattham

THIS THESIS HAS BEEN ACCEPTED BY

THESIS ADVISOR

(Associate Professor Thanya Kiatiwat, Ph.D.)

COMMITTEE MEMBER

(Professor Banchong Mahaisavariya, M.D.)

COMMITTEE MEMBER

(Mr. Kriskrai Sitthiseripratip, D.Eng.)

COMMITTEE MEMBER

(Associate Professor Santi Laksitanonta, D.Eng.)

COMMITTEE MEMBER

(Assistant Professor Supasit Rodkwan, Ph.D.)

COMMITTEE MEMBER

(Associate Professor Saeree Savetasareni, D.Eng.)

DEPARTMENT HEAD

(Associate Professor Chawalit Kittichaikarn, Ph.D.)

APPROVED BY THE GRADUATE SCHOOL ON _____

DEAN

(Associate Professor Gunjana Theeragool, D.Agr.)

THESIS

DESIGN OF HUMERAL NAIL BASED ON THAI MORPHOMETRIC DATA

PANYA AROONJARATTHAM

A Thesis Submitted in Partial Fulfillment of
the Requirements for the Degree of
Doctor of Engineering (Mechanical Engineering)
Graduate School, Kasetsart University
2009

Panya Aroonjarattham 2009: Design of Humeral Nail based on Thai Morphometric Data. Doctor of Engineering (Mechanical Engineering), Major Field: Mechanical Engineering, Department of Mechanical Engineering. Thesis Advisor: Associate Professor Thanya Kiatiwat, Ph.D. 187 pages.

The intramedullary nail fixation was widely accepted for minimal invasive technique with low morbidity, providing simultaneously rapid recovery and prompt return to work but Thai humerus has some geometric different from those Caucasian and it will has some clinical complication when use in Thai patient.

Computerized tomography, medical image processing, and reverse engineering was employed to analyze the geometric of humeral bone with non destructive specimens. A finite element method was employed to analyze the humeral bone that had the fracture gap on the mid-third region with standard humeral nail at normal and severe abduction with antegrade and retrograde insertion technique. The muscular force of rotator cuff and deltoid muscle were derived from magnetic resonance imaging and mechanical testing device which affected to the fracture gap.

The result showed that the ninety degree abduction had maximum strain at the lower gap between 15,422-57,727 microstrain with antegrade insertion. The new design of standard humeral nail with high mechanical performance reduced strain on the gap 84.40 % at lower range and 32.35 % at upper range from the standard humeral nail.

_____ _____ ___ / ___ / ___

Student's signature Thesis Advisor's signature

ACKNOWLEDGEMENT

The author would like to grateful thank to Assoc. Prof. Thanya Kiatiwat, Ph.D. my thesis advisor, Prof. Banchong Mahaisavariya, M.D., Kriskrai Sitthiseripratip, D.Eng., Assoc. Prof. Santi Luksitanonta, D.Eng, Asst. Prof. Supasit Rodkwan, Ph.D., and Assoc. Prof. Saeree Savetasareni, D.Eng. my committees for advice, encouragement and valuable suggestion for completely writing of thesis and Asst. Prof. Bancha Chernchujit, M.D. for his suggestion to find the muscular force.

The author would like to sincerely thank to my friends at the Medical rapid prototyping laboratory, National Metal and Materials Technology Center (MTEC), Mr. Pongnarin Jiamwatthanachai and Mr. Nattapon Chantarapanich for their assistance, Mr. Richard Goldrick for correcting this thesis, the Department of Anatomy, Faculty of Medicine Siriraj Hospital, Mahidol University for their kind support of providing cadaveric humeral bone specimens, the National Metal and Materials Technology Center (MTEC), Thailand for their kind support of providing the use of their facilities and the Department of Mechanical Engineering, Faculty of Engineering, Mahidol University for their kind support the author scholarship.

The author is especially appreciated my parents, who always support me everything, my sisters and brother for their continuing encouragement and Ms. Saowanee Changyongsuwan, who always gives me heartfelt love during my graduate study.

Panya Aroonjarattham

January 2009

TABLE OF CONTENTS

Page

LIST OF TABLES

LIST OF FIGURES

LIST OF FIGURES (Continued)

LIST OF FIGURES (Continued)

LIST OF FIGURES (Continued)

LIST OF FIGURES (Continued)

LIST OF FIGURES (Continued)

LIST OF FIGURES (Continued)

LIST OF FIGURES (Continued)

LIST OF FIGURES (Continued)

LIST OF FIGURES (Continued)

Appendix Figure **Page**

LIST OF ABBREVIATIONS

U	=	Displacement
R	=	Load vector
${}^{t}R$	=	External applied nodal point force
${}^{t}F$	=	Nodal point force
S	=	Shape function
u	=	Nodal displacement
v	=	Nodal displacement
w	=	Nodal displacement
V	=	Volume of tetrahedral element
$\vec{\delta}$	=	Displacement vector
σ_{xx}	=	Normal stress along x-axis
σ_{yy}	=	Normal stress along y-axis
σ_{zz}	=	Normal stress along z-axis
τ_{xy}	=	Shear stress in the x-y plane
τ_{yz}	=	Shear stress in the y-z plane
τ_{xz}	=	Shear stress in the x-z plane
ε_{xx}	=	Normal strain along x-axis
ε_{yy}	=	Normal strain along y-axis
ε_{zz}	=	Normal strain along z-axis
γ_{xy}	=	Shear strain in x-y plane
γ_{yz}	=	Shear strain in y-z plane
γ_{xz}	=	Shear strain in x-z plane
E	=	Young's Modulus
ν	=	Poisson's Ratio
G	=	Shear Modulus
L	=	Linear differential operator
Λ	=	Strain energy

LIST OF ABBREVIATIONS (Continued)

A	=	Surface
P	=	Pressure
Tesla	=	Unit of magnetic flux density
MPa	=	Mega Pascal (unit)
mm	=	millimeter (unit)
$\vec{i}$	=	Unit vector along x-axis
$\vec{j}$	=	Unit vector along y-axis
$\vec{k}$	=	Unit vector along z-axis
2D	=	Two-dimensional
3D	=	Three-dimensional
N	=	Newton
CT	=	Computerized Tomography
MRI	=	Magnetic Resonance Imaging
FEA	=	Finite Element Analysis
CAD	=	Computer Aided Design

DESIGN OF HUMERAL NAIL BASED ON THAI MORPHOMETRIC DATA

INTRODUCTION

1. Background

The high energy of a trauma, or impact, accident may cause fractures in any long bone of the human body. The incidence of humeral bone fracture among all fractures is about 3% in the U.S.A. and 4-5% in the UK. The goal of fracture treatment is early ambulation and complete return to function. There are three important processes in the mechanical aspect of fracture fixation: reduction, alignment and fixation.

Reduction is the process of apposing the fracture fragments. Reduction also describes the apposition of the fragments. It is usually described as anatomic reduction, near anatomic reduction, or non-anatomic reduction. None of these degrees of reduction is necessarily better than another; the one used is dependent on the specific fracture. Reduction should be undertaken as soon as the patient's condition permits. Delay typically results in a more difficult, traumatic reduction process.

Alignment refers to the relative orientation or position of the fragments, or more specifically, the joints above and below the fracture. Anatomic alignment is always strived for as this has a large bearing on function following healing. Alignment can be anatomic without anatomic reduction; however, anatomic reduction will always achieve anatomic alignment.

Fixation is the mechanism by which the fracture fragments are stabilized until sufficient healing occurs. The combination of the fixation device and the fracture

segments is called an osteosynthesis. In general, the fixation should allow near normal function during the healing process.

Humeral fractures have been variously treated, ranging from conservative treatments that use a splint as shown in Figure 1(A) to operative methods, the latter including open reduction and internal fixation with a plate and screws as shown in Figure 1(B) for fixing a humeral shaft fracture, and tension band wiring and an intramedullary nail as shown in Figure 1(C), where the nail is inserted in the medullary canal and prosthetic replacement.

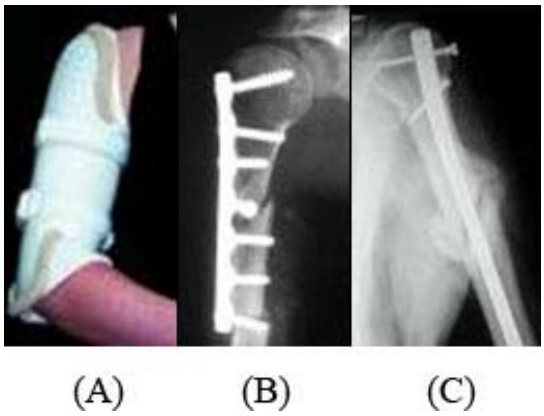

Figure 1 Three operative methods of humeral fracture fixation: (A) Splint, (B) Plate and screws, and (C) Intramedullary nail.

To preserve biological tissue, minimally invasive methods have become a new trend in treating bone fractures. Intramedullary fixation is widely accepted as a minimally invasive treatment technique with low morbidity, providing simultaneously rapid recovery and prompt return to work and daily life activities. The humeral nail is an intramedullary device to be use for fracture stabilization in the shaft region of the humeral bone. Nails differ in design depending on the surgical technique for which they are intended. They can be grouped into two general kinds:

1.1 Fixed humeral nails provide strong mechanical fixation of the fracture. They are made of either stainless steel or titanium, so their stiffness varies. Humeral nail products are shown in Table 1.

Table 1 Examples of fixed humeral nails.

Name	Company	Insertion technique	Reamed/unreamed
ACE humeral nail	De Puy	Antegrade/retrograde	Reamed
Austofix humeral nail	Austofix	Antegrade/retrograde	Reamed/unreamed
Flexible humeral nail	Synthes	Antegrade/retrograde	Reamed
Polarus nail (long version)	Acumed	Antegrade/retrograde	Reamed
Retrograde humeral nail	Biomet	Retegrade	Reamed/unreamed
Russell-Taylor humeral nail	Smith and Nephew	Antegrade	Reamed
T_2	Stryker	Antegrade/retrograde	Reamed/unreamed
Uniflex	Biomet	Antegrade	Reamed
Unreamed humeralnail	Synthes	Antegrade/retrograde	Unreamed

Source: Garnavos (2005).

The common characteristic is that locking screws provide both proximal and distal interlocks, and for that reason, axial and rotational stability at the

fracture site are good. Figure 2 shows a humeral nail in the medullary canal with a proximal and a distal screw.

Figure 2 Antegrade fixed-nail of a distal humerus fracture.
Source: Garnavos (2005).

1.2 Bio-nails are designed with attention to the biology and the anatomy of the arm. They are commonly made of either stainless steel or titanium. Bio-nail products are shown in Table 2.

Table 2 Examples of humeral bio-nails.

Name	Company	Insertion technique	Reamed/unreamed
Fixion nail	Disc-O-Tech medical technologies	Antegrade/retrograde	Reamed/undreamed
Halder nail	Corifix	Retrograde	Unreamed
Marchetti-Vicenzi nail	Zimmer	Retrograde	Semi-reamed
True-flex nail	Encore	Antegrade	Unreamed

Source: Garnavos (2005)

Their shared characteristic is the avoidance of locking screws at the tip of the nail. A unique, for each nail, feature or technique provides the ‘‘relative’’ stability needed for the fracture healing process. For example, the Marchetti nail consists of 4 or 5 spreading rods as shown in Figure 3 that abut firmly against the endosteum beyond the fracture and resist rotation.

Figure 3 Correct use of a retrograde bio-nail.
Source: Garnavos (2005).

2. Statement of Problem

The designs of prostheses have mostly been based on Caucasian morphometric data (Boileau and Walch, 1997, and Mahaisavariya *et al*., 2002). The Caucasian has a bigger anatomical structure than the Thai, and the lifestyles of the two are different. For example, Caucasian students carry their bags with a roller, but Thai students carry theirs with their hands although the bags are very heavy for them. An effect of this would be that the anatomy of the Thai humerus is different from that of the Caucasian, and thus prostheses made for Caucasians may not be proper for Thai patients (Leung *et al*., 1996, and Mahaisavariya *et al*., 2004). The humeral boundary condition differs from that of the femoral bone. It is held by muscles, and the weight of arm acts on the distal bone, but the load on the femur, i.e., the weight of the body, acts on the femoral head. While many researchers have investigated the femur, there are only a few studies of the humerus (Van der Helm *et al*., 1991, Wuelker *et al.*,

1993, and Kedgley *et al.*, 2007). For example, Debski *et al.* (1994) used a cadaveric model to find the abduction angle and muscular force magnitude but the direction of the muscular force could not be found. In this study, we use advanced techniques to find the direction and magnitude of muscular forces active in normal abduction conditions. FEA is used to find the stress distribution on the standard humeral nail when inserted in the Thai humerus.

3. Rationale

Clinical complications attending orthopedic implant relevant to size and shape not proper for Thai patients can be reduced by developments in biomechanical engineering. Revolutionary new techniques (computerized tomography, magnetic resonance imaging, computer-aided design, medical image processing, and finite element analysis) can be applied to design orthopedic implants in three dimensions, thus enhancing their performance.

4. Hypothesis

Differences between Caucasian and Thai anatomy will cause clinical complications when current commercial prostheses are used in Thai patients. This research aims to design a new humeral nail based on Thai morphometric data. It will cause fewer clinical complications and provide better mechanical performance due to less geometric mismatch between bone and implant than the current commercially available nails.

5. Objective of the Study

5.1 To determine the morphometric data of the Thai humerus using three-dimensional reverse engineering technique using data obtain from Thai humeral bone geometry.

5.2 To evaluate the geometric mismatch of the standard humeral nail in the Thai humerus.

5.3 To determine the muscular force in the shoulder joint based on special testing.

5.4 To conduct numerical simulation of the humeral nail in the Thai humerus.

5.5 To develop, based on the geometry of Thai humerus, a proper design for a humeral nail with the proper mechanical performance.

6. Scope and Limitation of the Study

The scope of the study is shown in Figure 4 from the three-dimensional morphometric study until the finite element analysis of the new humeral nail design and is defined by the following conditions:

6.1 The geometrical assessment results were based on the cadaveric dry bone, which may be slightly different from living bone tissue.

6.2 The muscle loading during abduction was obtained from mechanical testing to evaluate mechanical performance by means of a finite element method.

6.3 The prototyping and mechanical testing of the new standard humeral nail are beyond the scope of the study due to the time. However, both of them require further study.

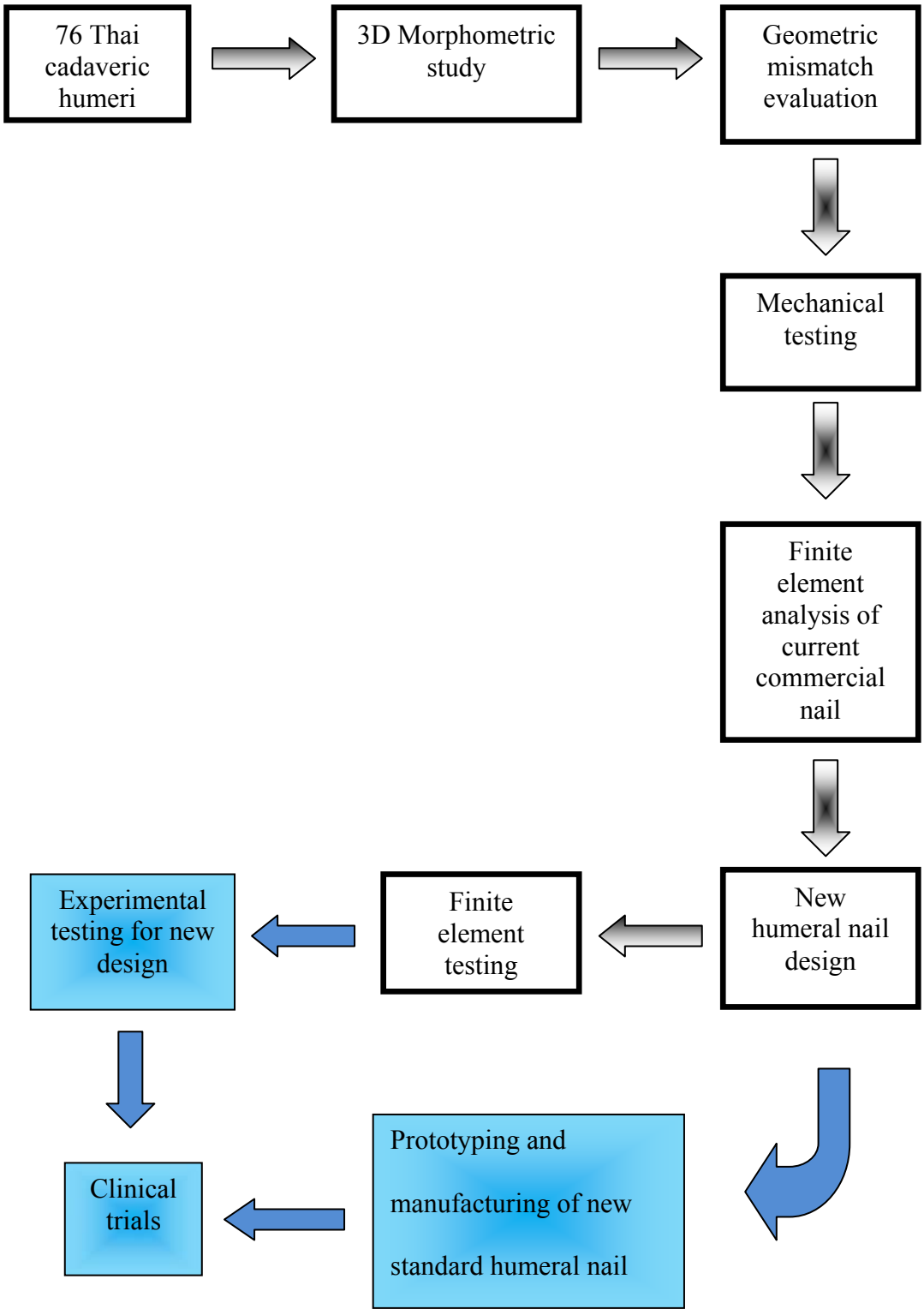

Figure 4 Methodology of development of a new standard humeral nail.

LITERATURE REVIEW

1. Related Research

1.1 Anatomy of the Humerus

Bones support and protect the human body. They transfer forces between joints and protect the underlying soft tissues (Boriani *et al*., 1991). Human bone is a dynamic biological tissue composed of metabolically active cells that are integrated into a rigid framework, which can be classified as a complex engineering material. It is a non-homogenous, anisotropic composite structure with viscoelastic properties. Moreover, its properties change with time, with the mechanical load exerted upon it, and with genetic and hormonal factors (Halder, 1992).

The humerus is the largest and longest bone of the upper extremity and connects the clavicle to the ulna and radius as shown in Figure 5. It is divided into a body and two extremities (Glenn, 2000).

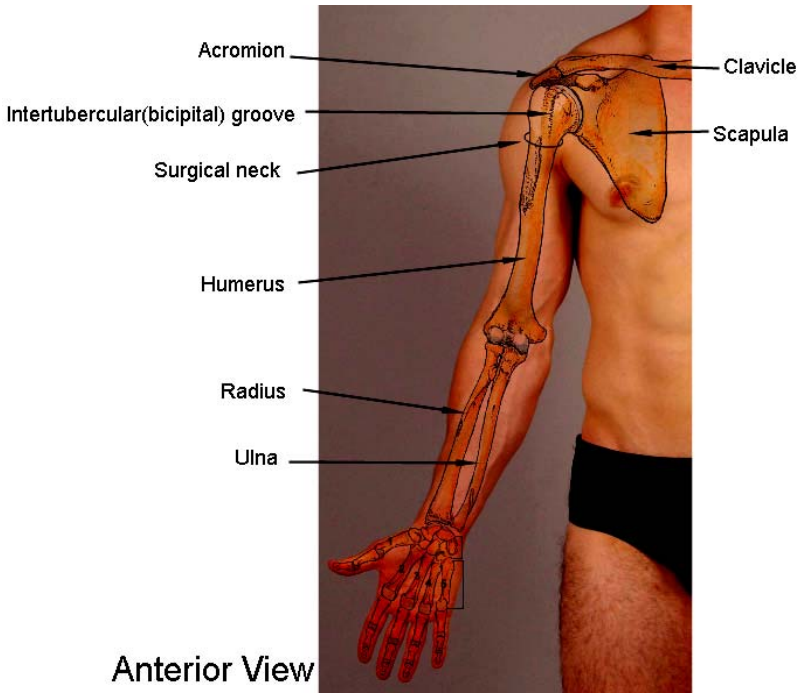

Figure 5 The bones of the upper extremity are the humerus, clavicle, scapula, ulna, and radius.

Source: Program dynamic human anatomy 2.0.

1.1.1 Upper Extremity

The upper extremity consists of a large rounded head joined to the body by a constricted portion called the surgical neck, and two eminences, the greater and lesser tubercles, as shown in Figure 6.

a) The Head, nearly hemispherical in form, is inclined relative to the shaft at the anatomical neck at an angle of 130° to 150°. The circumference of its articular surface is slightly constricted and is termed the anatomical neck, in contradistinction to a constriction below the tubercles called the surgical neck which is frequently the site of fracture.

b) The Anatomical Neck is obliquely directed, forming an obtuse angle with the body. It is best marked in the lower half of its circumference; in the

upper half it is represented by a narrow groove separating the head from the tubercles. It affords attachment to the articular capsule of the shoulder-joint, and is perforated by numerous vascular foramina.

c) The Greater Tubercle (greater tuberosity) is situated lateral to the head and lesser tubercle. It has three facets into which the tendons of the supraspinatus, infraspinatus, and teres minor insert. The lateral surface of the greater tubercle is convex, rough, and continuous with the lateral surface of the body.

d) The Lesser Tubercle (lesser tuberosity) is situated in front, and is directed medialward and forward. Above and in front it presents an impression for the insertion of the tendon of the subscapularis.

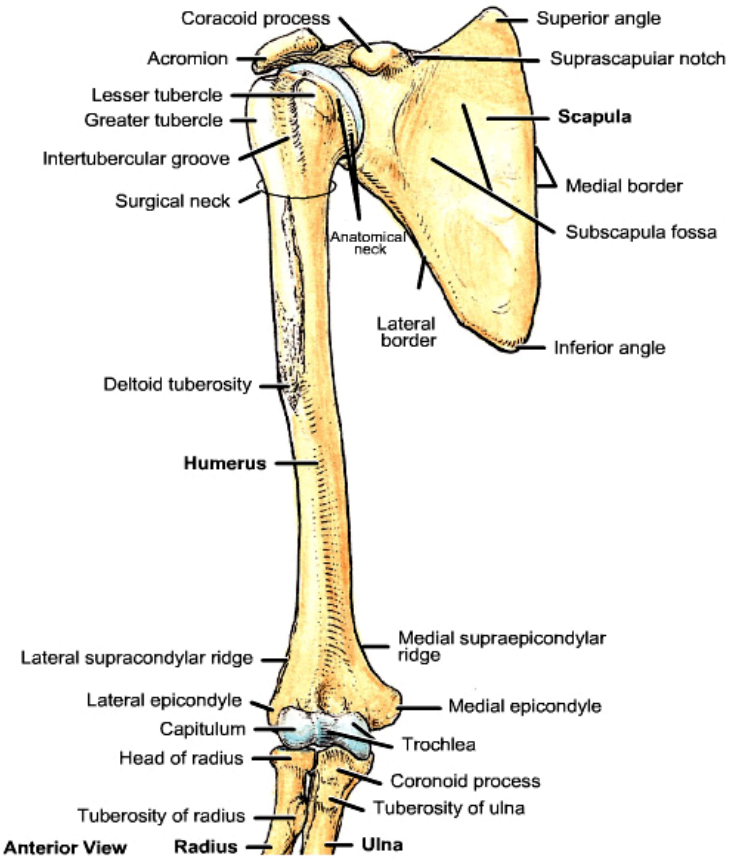

Figure 6 Structure of the humerus (Anterior view).

Source: Program dynamic human anatomy 2.0.

1.1.2 Body or Shaft

The body is almost cylindrical in the upper half of its extent, prismatic and flattened below, and has three borders and three surfaces.

a) The anterior border runs from the front of the greater tubercle above to the coronoid fossa below, separating the antero-medial from the antero-lateral surface.

b) The medial border extends from the lesser tubercle to the medial epicondyle.

c) The lateral border runs from the back part of the greater tubercle to the lateral epicondyle, and separates the anterolateral from the posterior surface.

1.1.3 The Lower Extremity

The lower extremity is flattened from before backward and curved slightly forward. It ends below in a broad, articular surface, which is divided into two parts by a slight ridge. Projecting on either side are the lateral and medial epicondyles. The articular surface extends a little lower than the epicondyles, and is curved slightly forward, while the medial extremity occupies a lower level than the lateral.

a) The lateral portion of this surface consists of a smooth, rounded eminence, named the capitulum of the humerus. It articulates with the cup-shaped depression on the head of the radius and is limited to the front and lower part of the bone. On the medial side of this eminence is a shallow groove, in which is received the medial margin of the head of the radius. Above the front part of the capitulum is a slight depression, the radial fossa, which receives the anterior border of the head of the radius when the forearm is flexed.

b) The medial portion of the articular surface is named the trochlea, and presents a deep depression between two well-marked borders. It is convex from before backward, concave from side to side, and occupies the anterior, lower, and posterior parts of the extremity. The lateral border separates it from the groove which articulates with the margin of the head of the radius. The medial border is thicker, of greater length, and consequently more prominent than the lateral.

The grooved portion of the articular surface fits accurately within the semi-lunar notch of the ulna. It is broader and deeper on the posterior than on the anterior aspect of the bone, and is inclined obliquely downward and forward toward the medial side. Above the front part of the trochlea is a small depression, the coronoid fossa, which receives the coronoid process of the ulna during flexion of the forearm. Above the back part of the trochlea is a deep triangular depression, the olecranon fossa, in which the summit of the olecranon is received in extension of the forearm. This fossa is separated from one another by a thin, transparent lamina of bone, which is sometimes perforated by a supratrochlear foramen.

The lateral epicondyle is a small, tuberculated eminence, curved a little forward, and giving attachment to the radial collateral ligament of the elbow-joint, and to a tendon common to the origin of the supinator and some of the extensor muscles. The medial epicondyle, larger and more prominent than the lateral, is directed a little backward; it gives attachment to the ulna collateral ligament of the elbow-joint, to the pronator teres, and to a common tendon of origin of some of the flexor muscles of the forearm; the ulna nerve runs in a groove on the back of this epicondyle. The epicondyles are continuous above with the supracondylar ridges.

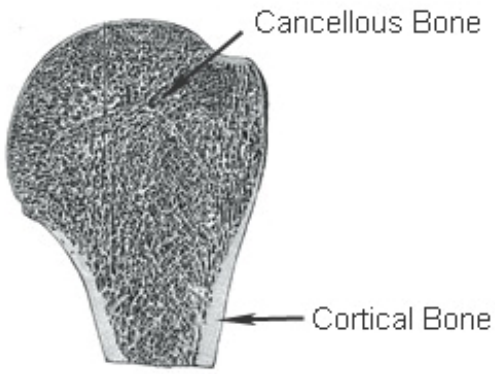

Figure 7 Section of humeral head.
Source: Henry (1918).

The extremities consist of cancellous tissue, covered with a thin, compact layer as shown in Figure 7. Cortical bone is a dense material, which is found mostly in the diaphysia region of long bone. It also called compact or lamellar bone. It is remodeled from woven bone by means of vascular channels that invade the embryonic bone from its periosteal and endosteal surfaces. It forms the internal and external tables of flat bones and the external surfaces of long bones. The primary structural unit of cortical bone is an osteon, also known as a haversian system. Osteons consist of cylindrical shaped lamellar bone that surrounds longitudinally oriented vascular channels called haversian canals. Horizontally oriented canals (Volkmann canals) connect adjacent osteons. The mechanical strength of cortical bone depends on the tight packing of the osteons.

Cancellous bone (trabecular bone) lies between cortical bone surfaces and consists of a network of honeycombed interstices containing hematopoietic elements and bony trabeculae. The trabeculae are predominantly oriented perpendicular to external forces to provide structural support (White and Hirsch, 1971, and Herron and Newman, 1989). Cancellous bone is continually undergoing remodeling on the internal endosteal surfaces. It is found in the extremities (epiphysial region) of long bone, where it is covered by a small layer of cortical bone

and with flat and short bones. The strength of trabecular bone is about 1/10 of cortical bone.

1.2 Muscles around the Shoulder Joint

The shoulder joint is a ball-and-socket joint that consists of the round head of the humerus and the shallow glenoid cavity of the scapula. The joint capsule of the shoulder is attached along the circumference of the glenoid cavity and the anatomical neck of the humerus as shown in Figure 8. Although it completely envelopes the joint, the capsule is very loose, and by itself is unable to keep the bones of the joint in close contact. However, muscles and tendons surround and reinforce the capsule, keeping together the articulating parts of the shoulder.

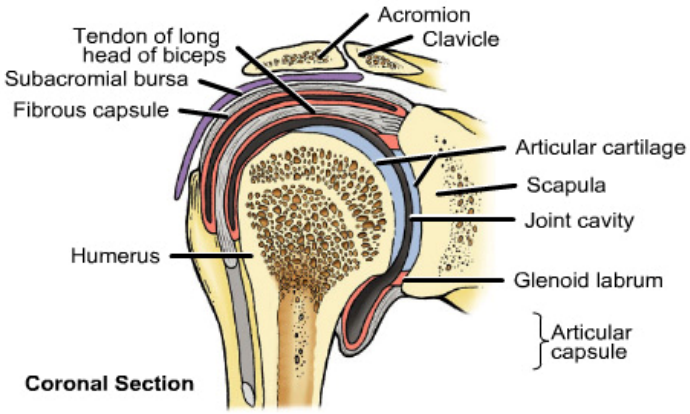

Figure 8 Cross section of the shoulder joint.
Source: Program dynamic human anatomy 2.0.

1.2.1 Muscles move the arm

The arm is one of the more freely movable parts of the body because muscles connect the humerus to regions of the pectoral girdle, ribs, and vertebral column. These muscles can be grouped according to their primary actions—

flexion, extension, abduction, and rotation. All muscle attaching around the humerus are shown in Figure 9.

Flexors	Abductors	Extensors	Rotators
Coracobrachialis	Supraspinatus	Teres major	Subscapularis
Pectoralis major	Deltoid	Latissimus dorsi	Infraspinatus
			Teres minor

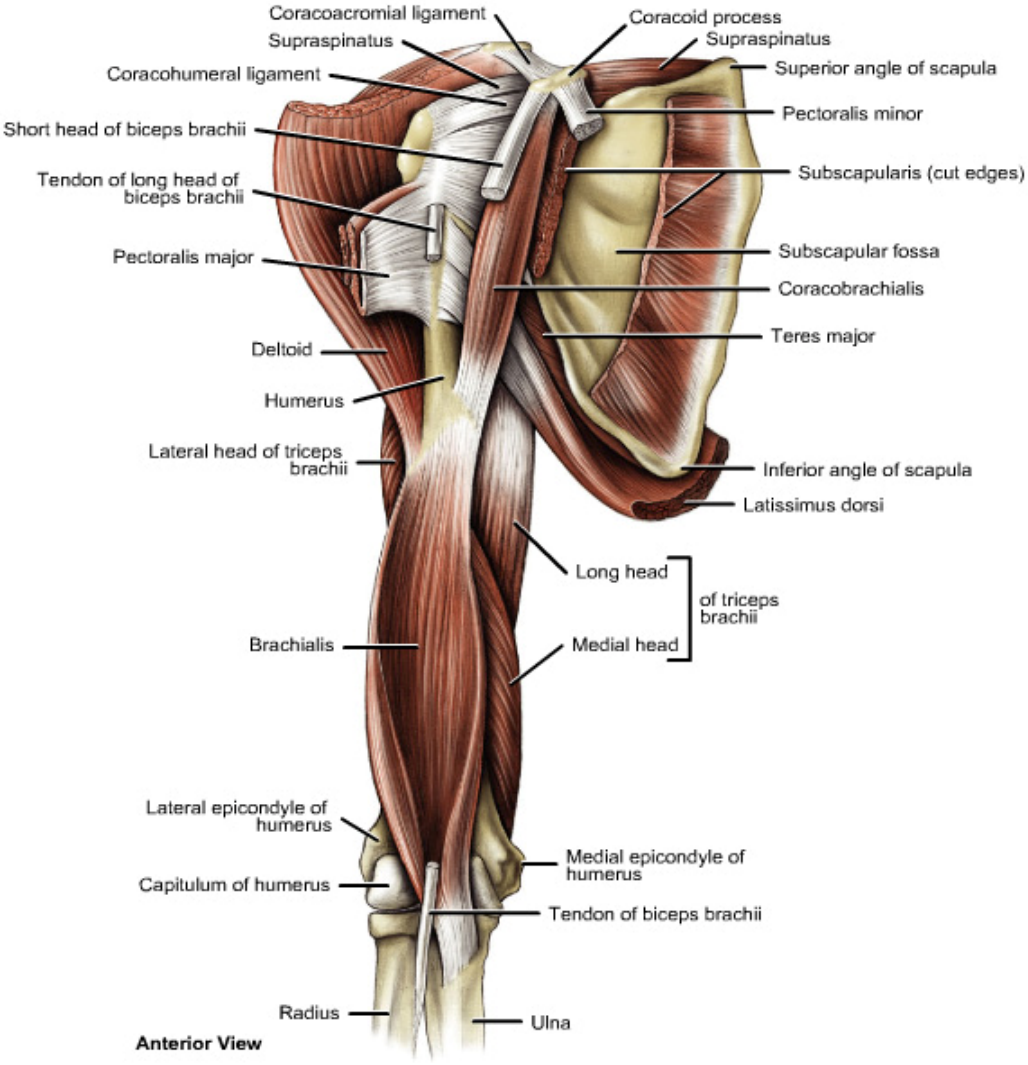

Figure 9 Muscles around the humerus.

Source: Program dynamic human anatomy 2.0.

a) The coracobrachialis extends from the scapula to the middle of the humerus along its medial surface. It flexes and adducts the arm.

b) The pectoralis major is a thick, fan-shaped muscle located in the upper chest. Its fibers extend from the center of the thorax through the armpit to the humerus. This muscle primarily pulls the arm forward and across the chest. It can also rotate the humerus medially and adduct the arm from a raised position.

c) The supraspinatus is located in the depression above the spine of the scapula on its posterior surface. It connects the scapula to the greater tubercle of the humerus and abducts the arm.

d) The deltoid is a thick, triangular muscle that covers the shoulder joint. It connects the clavicle and scapula to the lateral side of the humerus and abducts the arm. The deltoid's posterior fibers can extend the humerus, and its anterior fibers can flex the humerus.

e) The teres major connects the scapula to the humerus. It extends the humerus and can also adduct and rotate the arm medially.

f) The latissimus dorsi is a wide, triangular muscle that curves upward from the lower back, around the side, and to the armpit. It can extend and adduct the arm and rotate the humerus medially. It also pulls the shoulder downward and back. This muscle is used to pull the arm back in swimming, climbing, and rowing

g) The subscapularis is a large, triangular muscle that covers the anterior surface of scapula. It connects the scapula to the humerus and rotates the arm medially.

h) The infraspinatus occupies the depression below the spine of the scapula on its posterior surface. The fibers of this muscle attach the scapula to the humerus and rotate the arm laterally.

i) The teres minor is a small muscle connecting the scapula to the humerus. It rotates the arm laterally.

1.3 Fractures of the Humerus

1.3.1 Fracture Classification

The classification of humeral shaft fractures is based on the nature and location of the primary fracture line, an estimation of the kinematics of the injury, and associated soft tissue trauma.

a) Fracture personality (direction and character of the fracture)

[1]. Transverse fractures that are not internally splinted by the intravascular septa may be difficult to control.

[2]. Oblique fractures usually unite without difficulty.

[3]. Spiral fractures in the distal third may produce a radial nerve injury and its segmental injuries are also difficult to control.

[4]. Comminuted fractures are associated with soft tissue injury and difficult to manage by internal fixation, but unite well with non-operative fracture management.

b) Associated soft tissue injury

[1]. Open: Grade1 (low energy, wound less than 1 cm)
Grade2 (moderate energy and soft tissue damage, wound greater than 1 cm)
Grade3 (high energy, wound greater than 10 cm)

[2]. Periarticular injury: Glenohumeral, Elbow joint

[3]. Nerve injury: Radial nerve, Median nerve, Ulna nerve

[4]. Vascular injury: Brachial artery, Brachial vein

1.3.2 Humerus Fracture

a) Proximal Humerus Fractures occur near the shoulder joint as shown in Figure 10. The shoulder joint is a ball-and-socket joint, with the ball being the top of the humerus. Fractures of this ball are considered proximal humerus fractures. These fractures may involve the insertion of the important rotator cuff tendons. Because these tendons are important to shoulder motion, treatment may depend on the position of these tendon insertions.

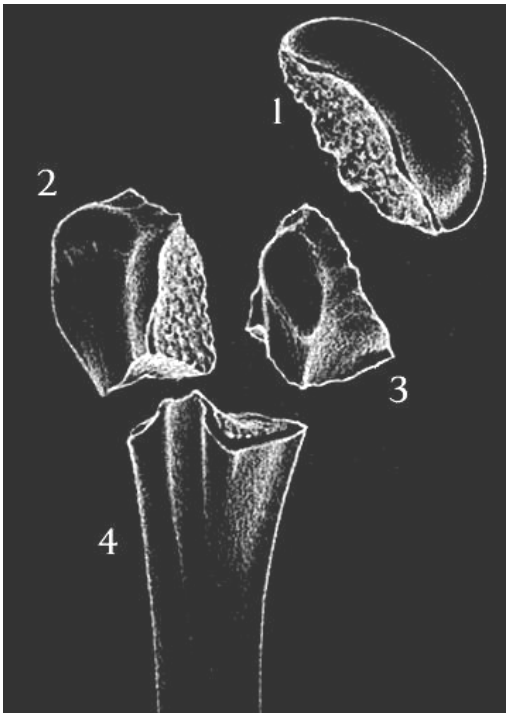

Figure 10 The Neer classification of the proximal humerus fracture, the proximal humerus is made up of four parts: (1) Humeral head, (2) Greater tubercle, (3) Lesser tubercle, and (4) Diaphysis (shaft).

b) Mid-Shaft Humerus Fractures occur away from the shoulder and elbow joints as shown in Figure 11. Most humeral shaft fractures will heal without surgery, but there are some situations that require surgical intervention. These injuries are commonly associated with injury to one of the large nerves in the arm, called the radial nerve. Injury to this nerve may cause symptoms in the wrist and hand.

Figure 11 Mid-shaft fracture of humeral bone.

c) Distal Humerus Fractures are uncommon injuries in adults. These fractures occur near the elbow joint as shown in Figure 12. These fractures most often require surgical treatment unless the bones are held in proper position. This type of fracture is much more common in children, but the treatment is very different in this age group.

Figure 12 Distal fracture of humeral bone.

1.3.3 Fracture Management

Historically, fractures of the humeral shaft have been associated with a high incidence of nonunion. On this very topic, Klenerman in 1982 wrote, “It is a pity that in some parts of the world a trend of recent years has been to operate more and more readily on recent fractures of the humerus, sometimes relying on totally inadequate techniques of internal fixation without sufficient external protection thus causing established nonunion of the fracture. However, during the past two decades, advances in operative stabilization techniques and optimization of fracture bracing have led to significant decline in nonunion rates.”

Several variables must be considered before formulating a treatment plan. The fracture pattern, degree of soft tissue injury, associated neurologic injury, patient age, comorbidity, and patient compliance should be considered together to optimize treatment success and limit the risk of complications. However, significant fracture deformity indicates a need for open reduction and operative stabilization. In all cases, fracture management is combined with early motion and rehabilitation of the injured extremity to limit problems associates with fracture disease.

a) Non-operative treatment

Most humeral shaft fractures can be managed non-operatively with expected union rates approaching 100%. The generally good outcomes with non-operative treatment may be due in part, to tolerance of malunion in the arm. Functional fracture bracing has largely replaced all other procedures as the treatment of choice for these injuries.

(a) Hanging arm casts. This technique, shown in Figure 13, remains a standard management technique for humeral shaft fractures. The indications for use of hanging arm cast include displaced mid-shaft humeral fractures with shortening, particularly fractures with an oblique or spiral pattern. Use of the hanging arm cast is not indicated for transverse fractures because of the potential for distraction and healing complications.

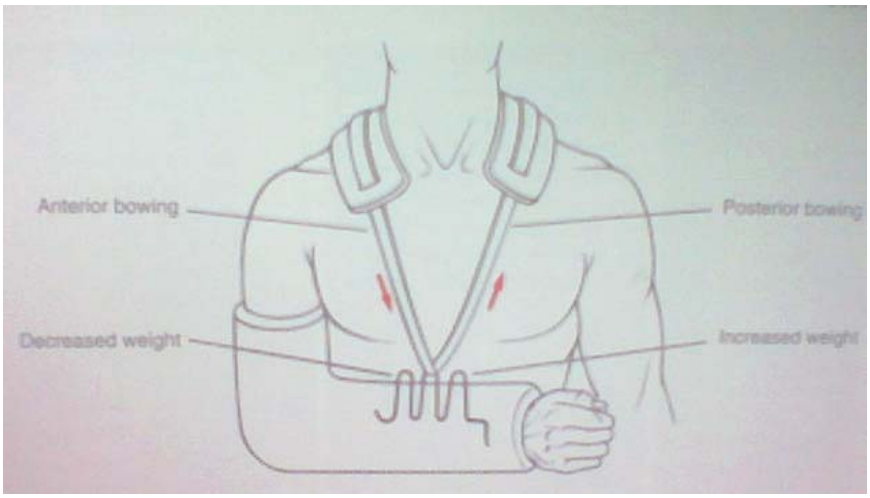

Figure 13 A hanging arm cast is used both to obtain reduction of the fracture and to allow union in this reduced position.

Most surgeons use the hanging arm cast to achieve reduction in the first week after the fracture and replace it with a functional brace until healing occurs. Over distraction of the fracture is always a risk with this technique. Patients should be allowed to begin active-assisted shoulder and hand exercises within the

tolerance of their pain. Isometric exercises for the remainder of the arm are also recommended for optimal results.

(b) Velpeau dressing/sling and swathe. An inexpensive, easily applied device for immobilization of the shoulder and humerus, but more restrictive device, is the sling and swathe dressing, which is most useful for non-displaced or minimally displaced fractures in children younger than 8 years or in elderly patients who are unable to tolerate other methods of management. Pads composed of various materials can be placed in the axilla to control the angulation of the fracture site. These splints serve as load-sharing devices and rely heavily on the inherent soft tissue integrity around the fracture to maintain stability.

(c) Coaptation splint. A coaptation splint supplemented with a collar and cuff is often used to acutely splint humeral shaft fractures that are minimally displaced or not suitable for a hanging arm cast. The arm should be covered with a stockinette and supplemental padding before plaster application. Care should be taken to ensure that the plaster extends over the deltoid, around the elbow, and up to the axilla. The patient can expect motion of the hand and wrist. Close follow-up is necessary to identify potential pitfalls such as axillary irritation, shortening of the fracture, displacement, and pain.

(d) Abduction Splint-Shoulder Spica Cast. A plaster or Orthoplast splint supporting the arm in abduction has been advocated for certain humeral shaft fractures. The primary indication may be for situations in which closed reduction of the fracture requires significant abduction and external rotation of the upper extremity. Disadvantages of these splints include the unusual and awkward position of the arm, immobilization of the shoulder, and pressure on the rotator cuff.

(e) Skeletal Traction. Skeletal traction is rarely indicated. However, it can be used in patients who must remain recumbent or have extensive soft tissue injuries requiring open wound care. When used, skeletal traction is applied through a transolecranon Kirschner wire or Steinmann pin.

(f) Functional Bracing. A functional brace is an orthosis that achieves fracture reduction through soft tissue compression. Though initially designed as a wraparound sleeve, current braces use an anterior shell with a contour for the biceps tendon and a posterior shell with a triceps contour to ensure adequate compression and support for the fracture. One of the shells is designed to fit inside the other, and Velcro straps hold the brace in proper position. These straps can be tightened as swelling decreases over time. Slings can be used initially but should be discontinued as soon as feasible because they lead to varus and internal rotation deformities. The distal sleeve of the brace is fashioned to avoid the medial and lateral epicondyles and permit free elbow motion. Abduction should be limited to 60° to 70° until fracture healing has progressed and is evident on radiographs. The brace should be worn for at least 8 weeks and can be discontinued if the patient exhibits pain-free abduction with radiographic evidence of fracture healing. Union rates of 96% to 100% have been reported with these devices.

b) Operative treatment

Given the relative propensity for delayed union in transverse or short oblique fractures managed non-operatively in an active individual, these fracture patterns may be relative indications for surgery. Alternatives to operative stabilization include intramedullary nailing, compression plating and screw osteosynthesis, and external fixation.

1.4 Material Properties of Bone

1.4.1 Cortical Bone

The mechanical properties of bone tissue are typically determined by measuring the deformation of small, uniform specimens during application of simple, well-defined loads. Figure 14 illustrates a typical test that involves subjecting a machined cortical bone specimen to tensile loads. Dumbbell-

shaped tensile specimens are typically used, so that failure occurs in a reproducible location.

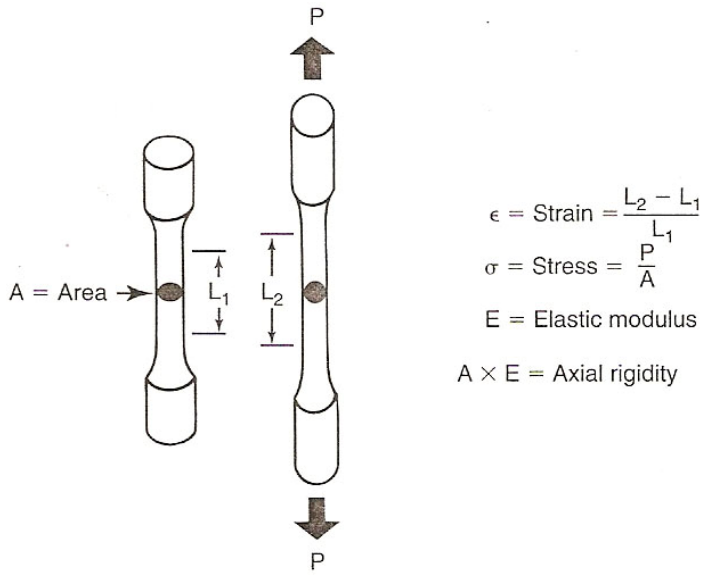

Figure 14 Simple uniaxial tensile test with a dumbbell-shaped specimen, P is the applied load and $(L_2\text{-}L_1)/L_1$ is the strain between two points along the specimen's axis.

Source: Browner *et al*. (1998).

Two parameters are monitored during the tensile test: the applied force and the displacement between two points along the long axis of the specimen. The resulting force displacement curve provides an indication of the stiffness and failure load of the bone specimen, but the data are useful only for specimens with the same geometry as the one tested. To provide material property data that can be applied to any specimen geometry, the force and displacement data are converted to stress and strain. This is a normalization process that eliminates the influence of specimen geometry. The stress in the bone specimen is calculated as the applied force divided by the cross-sectional area, and the strain is measured as the percentage change in length of a defined length of the specimen. A typical stress-strain curve for a tensile test of cortical bone is shown in Figure 15.

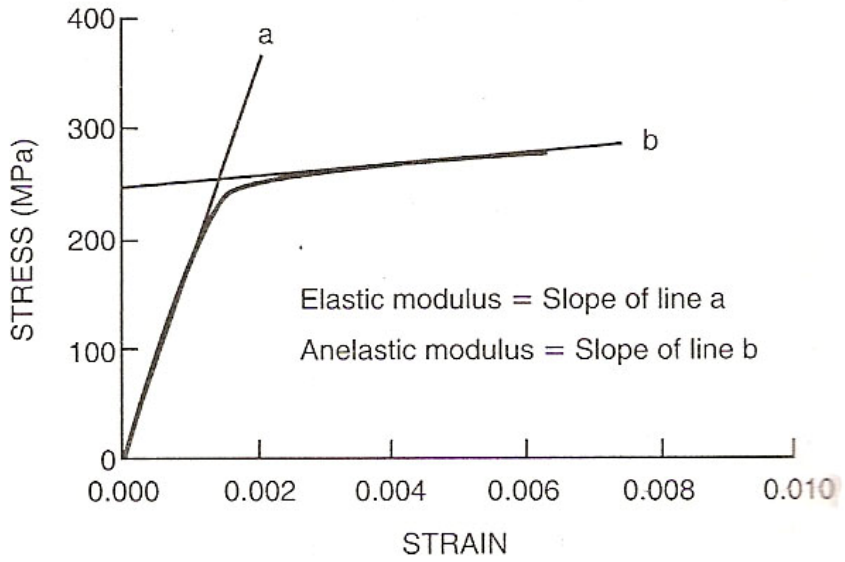

Figure 15 Typical stress-strain curve for human cortical bone showing the curve regions where the elastic and anelastic moduli are calculated.

Source: Browner *et al*. (1998).

The elastic modulus of bone tissue or structural materials such as stainless steel, titanium, or polymethyl methacrylate is determined from the slope of the initial, linear part of the curve. The point at which the slope of the stress-strain curve decreases is the yield point of the bone, and the maximal recorded stress is the ultimate strength of the tissue. After the bone has yielded, the slope of the stress-strain curve drops to a new value termed the anelastic modulus. The area under the stress-strain curve reflects the capacity of bone to absorb energy. The capacity to absorb energy increases with yield strength, but the greatest energy absorption is typically seen for bones with high ultimate strains, where substantial energy is absorbed during post yield deformation.

Bone is loaded cyclically during many activities of daily living, and the load required to cause bone to fail will be dramatically lower if that load is applied repeatedly. The number of cycles of stress that bone can tolerate decreases as the stress level increases. This property of bone is measured using stress-versus-number of cycles to failure (SN) curves. These curves depend on the type of loading

(axial, bending, or torsion), the loading rate, and the physical composition of the bone. The mechanisms in bone that determine its behavior under cyclical loading are beginning to be understood.

The stress-strain behavior of cortical bone is also strongly dependent on the orientation of bone microstructure with respect to the loading direction. Several investigators have shown that cortical bone is both stronger and stiffer in the longitudinal direction than in the transverse direction. Materials such as bone whose mechanical properties depend on the loading direction are said to be anisotropic.

1.4.2 Trabecular Bone

The major physical difference between trabecular bone and cortical bone is the increased porosity exhibited by trabecular bone. This porosity is reflected by measurements of the apparent density. In the human skeleton, the apparent density of trabecular bone ranges from approximately 0.1 g/cm^3 to 1.0 g/cm^3, whereas the apparent density of cortical bone is about 1.8 g/cm^3. A trabecular bone specimen with an apparent density of 0.2 g/cm^3 has a porosity of about 90%.

The compressive stress-strain properties of trabecular bone are markedly different from those of cortical bone and are similar to the compressive behavior of many porous engineering materials that absorb energy on impact. Stress-strain curves for trabecular bone in compression exhibit an initial elastic region followed by yield as shown in Figure 16. The slope of the initial elastic region ranges from one to two orders of magnitude less than that of cortical bone. Yield is followed by a long plateau region created as more trabeculae fracture. The fractured trabeculae begin to fill the marrow spaces at approximately 50% strain. Further loading of the specimen after the pores are filled is associated with a marked increase in specimen modulus.

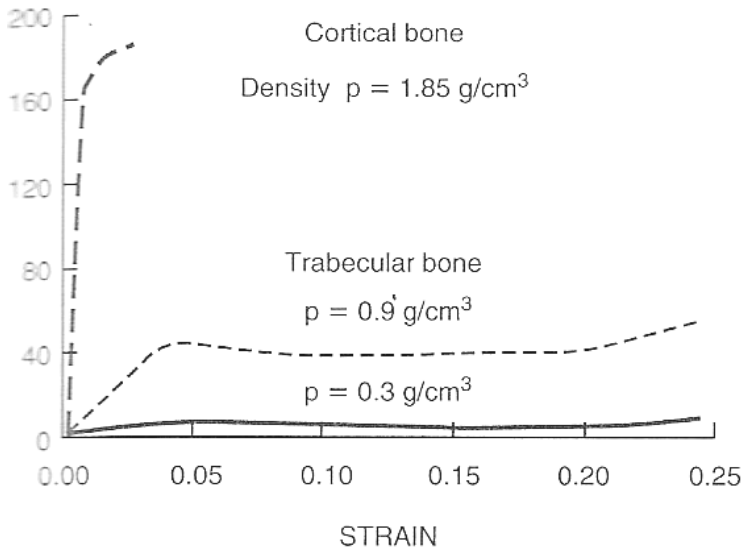

Figure 16 Compressive stress-strain curves for cortical and trabecular bone of different densities.

Source: Browner *et al*. (1998).

1.5 Bone Repair and Fracture Healing

The process of bone healing follows an ordered progression based on the material properties of the healing constituents. The tissues associated with healing are able to withstand a determined degree of internal motion or strain depending upon the tissue type. Granulation tissue is able to withstand 100% strain (it can increase in length 100%), cartilage 15% strain and bone 2% strain as shown in Figure 17(B) (Cross). Therefore cartilage, for example, will not form in the healing process until fibrous tissue has stabilized the fracture fragments to within 15% strain. Tissue is more effective at reducing strain the further it is from the center of the bone as shown in Figure 17(C), hence a large callus is seen with unstable fractures. By stabilizing fractures to varying degrees, we can skip or shorten the time required to reach a strain environment in which a given tissue can form. In the most stable repairs, we can skip all intermediate tissue types and progress to direct bone formation. All the processes are shown in Figure 17.

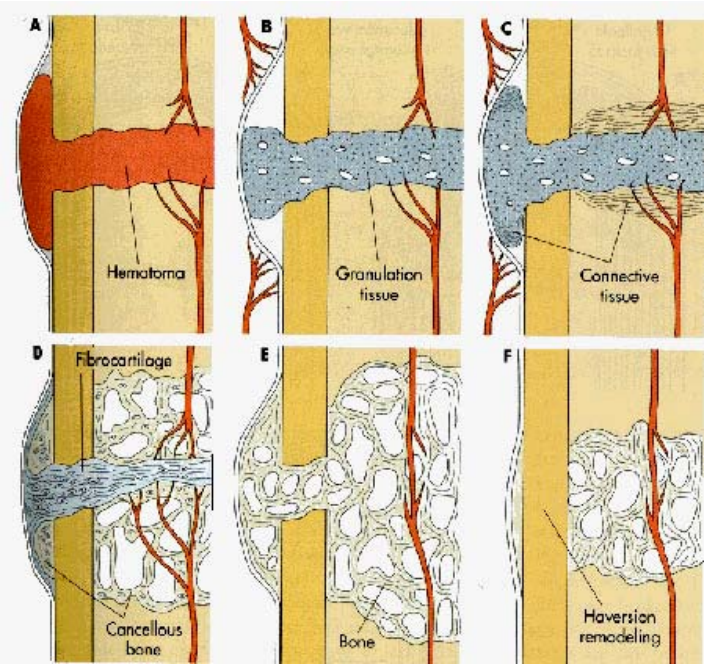

Figure 17 The processes of bone repair and fracture healing: (A) Hematoma, (B) Granulation tissue, (C) Connective tissue, (D) Cancellous bone, (E) Bone, and (F) Haversion remodeling.

Source: College of Veterinary Medicine.

There are two types of fracture healing: secondary bone healing and primary bone healing.

1.6 Secondary Bone Healing (with callus formation)

The type of union that occurs with spontaneous fracture healing and forms of immobilization or fixation that do not provide rigid stabilization of a fracture is called a secondary bone healing. This type of fracture healing occurs in three distinct but overlapping stages: 1) the early inflammatory stage; 2) the repair stage; and 3) the late remodeling stage (DePalma *et al*., 1972, Burchardt and Enneking, 1978, and Kalfas, 2001).

In the inflammatory stage, a hematoma develops within the fracture site during the first few hours and days. Inflammatory cells (macrophages, monocytes, lymphocytes, and polymorphonuclear cells) and fibroblasts infiltrate the bone under prostaglandin mediation. This results in the formation of granulation tissue, ingrowth of vascular tissue, and migration of mesenchymal cells. The primary nutrient and oxygen supply of this early process is provided by the exposed cancellous bone and muscle.

During the repair stage, fibroblasts begin to lay down a stroma that helps support vascular ingrowth. It is during this stage that the presence of nicotine in the system can inhibit this capillary ingrowth (Rubenstein *et al*., 1991, Daftari *et al*., 1994, Riebel *et al*., 1995, and Silcox *et al*., 1995). A significantly decreased union rate had been consistently demonstrated in tobacco abusers (Brown *et al*., 1986, Blumenthal *et al*., 1988, and Bishop *et al*., 1996). As vascular ingrowth progresses, a collagen matrix is laid down while osteoid is secreted and subsequently mineralized, which leads to the formation of a soft callus around the repair site. In terms of resistance to movement, this callus is very weak in the first 4 to 6 weeks of the healing process and requires adequate protection in the form of bracing or internal fixation. Eventually, the callus ossifies, forming a bridge of woven bone between the fracture fragments. Alternatively, if proper immobilization is not used, ossification of the callus may not occur, and an unstable fibrous union may develop instead.

Fracture healing is completed during the remodeling stage in which the healing bone is restored to its original shape, structure, and mechanical strength. Remodeling of the bone occurs slowly over months to years and is facilitated by mechanical stress placed on the bone. As the fracture site is exposed to an axial loading force, bone is generally laid down where it is needed and resorbed from where it is not needed. This is subjected to the Wolff's law (1892) of structural adaptation of bone, noting that bone placed under compressive or tensile stress is remodeled. Bone is formed where stresses require its presence and resorbed where stresses do not require it (Recker, 1992, and Wolff, 1986). Adequate strength is typically achieved in 3 to 6 months.

1.7 Primary Bone Healing (without callus formation)

Primary bone healing occurs with anatomic reduction and rigid (generally internal) fixation. As in secondary healing, there is interruption of the bone's blood supply and necrosis of the fracture ends. Remember this affects the cellular components (osteocytes) of the bone, but has little effect on the material components. There are two components to primary bone healing: gap healing and contact healing (Kalfas, 2001).

1.7.1 Gap Healing

On a microscopic level (Kalfas, 2001), even a fracture that is perfectly reduced has irregular surfaces and this creates gaps between fragments. In the first stage of gap healing, gaps less than 200-500 microns (possibly up to 1000 microns) in width will be filled by direct bone formation. This means that neither connective tissue nor fibrocartilage preceded bone formation. In the second phase of gap healing, this disorganized woven bone is longitudinally reconstructed by Haversian remodeling. It should be stated that even with rigid internal fixation, gaps greater than 1 mm are partially filled with fibrous tissue, which is subsequently replaced by bone in a process similar to secondary bone healing.

1.7.2 Contact Healing

Contact healing (Kalfas, 2001) occurs in areas where the fracture fragments are in direct apposition and results in union through direct ingrowth of Haversian systems across the fracture. Osteoclasts form cutting cones that advance across the fracture line forming a resorption cavity. This is followed by the growth of a capillary loop down the center of the resorption cavity. Mesenchymal cells and osteoprogenitor cells accompany these capillaries, become osteoblasts and produce osteoid closing cone. The conical shape of these bone forming units is accounted for by the relative speeds of the cutting and closing cones. The osteoclasts

are approximately 10 times faster than the osteoblasts and this has important implications on the timing of implant removal.

1.8 Biomechanics of Fracture Treatment

Many techniques are currently available for treatment of skeleton fracture, and many factors are important in choosing the best fixation. Each method of fixation imparts a specific level of stability to a fracture and thus directly influences fracture healing biology. When evaluating a fracture treatment method, the healing bone and the fracture treatment device should be considered as a mechanical system, with both the tissue and the device contributing to biomechanical behavior. The biomechanical behavior of the system can thus be altered by changes in tissue properties, changes to the fracture treatment device, or changes to the mechanical connection between device and tissue.

1.8.1 Internal Fixation

a) Intramedullary Rods have several advantages in fracture treatment, including restoration of bony alignment and early recovery of weight bearing. The good clinical results and low rates of nonunion suggest that many current clinical applications of these devices provide a mechanical environment that facilitates fracture repair for selected fractures. Intramedullary rods are intended to stabilize a fracture by acting as an internal splint as shown in Figure 18, forming a composite structure in which both the bone and the rod contribute to fracture stability. This load-sharing property of rods is fundamental to their design and should be recognized when they are used for fracture treatment.

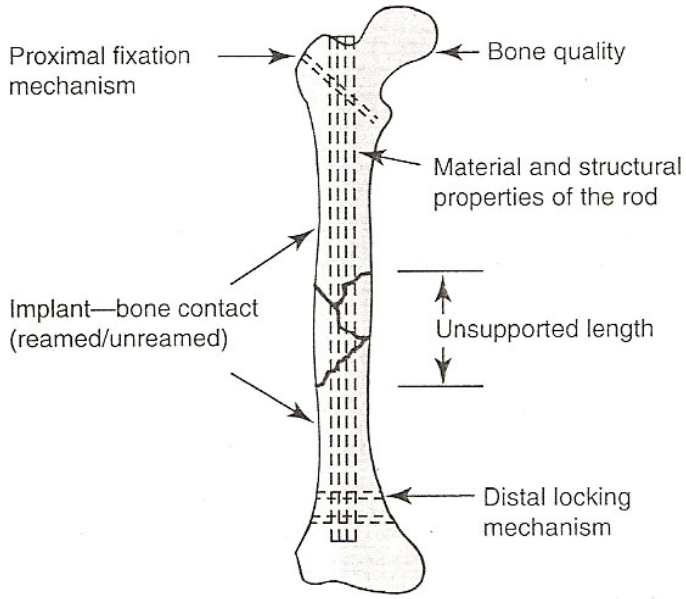

Figure 18 Factors important in intramedullary fracture fixation.
Source: Browner *et al*. (1998).

b) Bone Plate, Several basic biomechanical principles are important to fracture fixation using bone plates. Figure 19 illustrates some important parameters. It is crucial to realize that the plate and the bone together form a mechanical construct, with some load supported by the plate and some load passing between bone fragments. The interaction between plate and bone is also load-dependent; the plate may improve stability for one type of loading much more than for other types of loads.

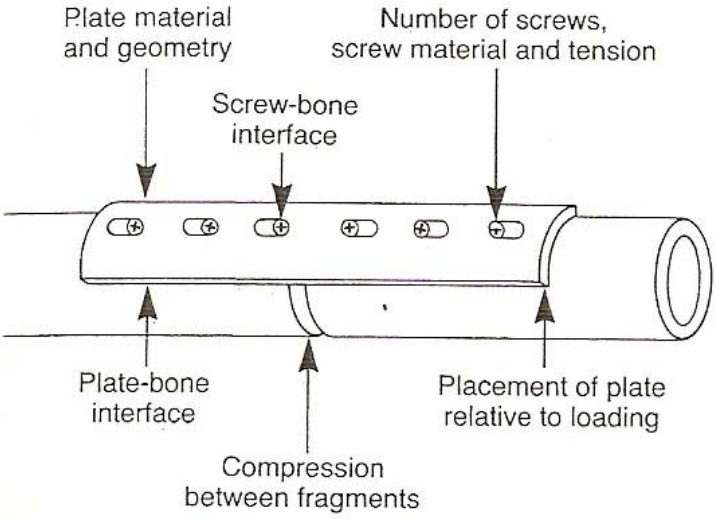

Figure 19 Factors affecting the stability of a plated fracture.
Source: Browner *et al*. (1998).

1.8.2 External Fixation

Current external devices provide a wide range of frame configurations and fracture stability options, making external fixation adaptable to many clinical situations. External fixation devices also provide a convenient way to alter fixation rigidity during the course of healing and offer potential for monitoring the biomechanical progression of fracture healing. The stability provided by an external fixation device depends on both the frame configuration and the interaction between frame and bone fragments. As shown in Figure 20, several geometric, material and technical factors, as well as loading directions, can play a role in the biomechanics of external fixed fractures.

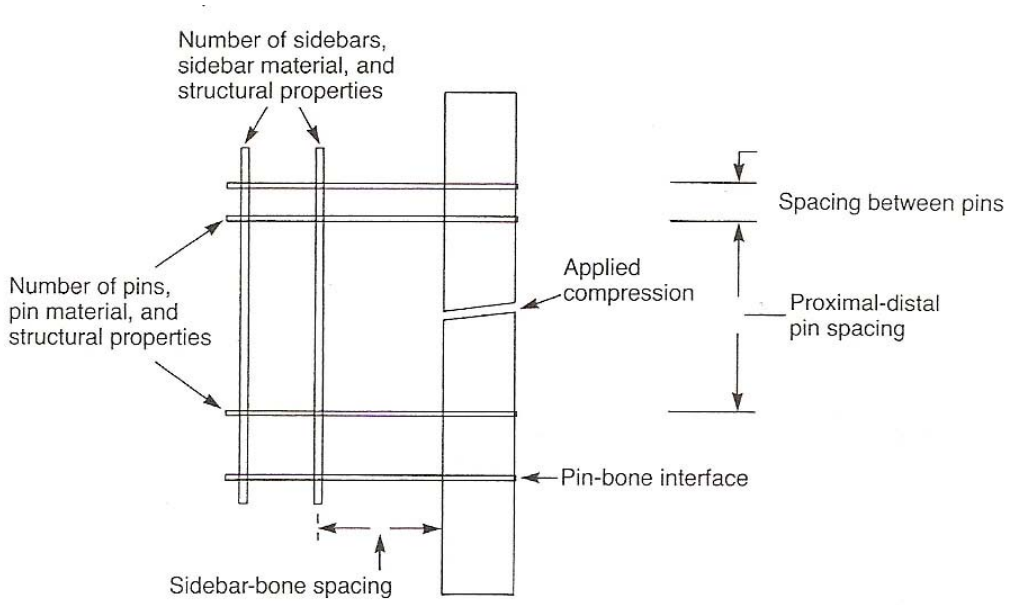

Figure 20 Factors affecting the stability of an externally fixed fracture.
Source: Browner *et al*. (1998).

1.9 Three-dimensional Morphometric Study of the Thai Proximal Humerus: Anatomical Study

The variation in geometrical data on the proximal humerus shows that the Thai humerus is relatively different from the Caucasian. A previous study reported that small changes in anatomy may have important biomechanical consequences (Michael and Sam, 1999). There is, therefore, some likelihood that using a shoulder arthroplasty that is based on the Caucasian design in the Thai patient may not achieve the optimal clinical outcomes. Prosthetic arthroplasty of the shoulder is widely practiced for the treatment of glenohumeral arthritis (such as osteoarthritis, traumatic arthritis, osteonecrosis, rheumatoid arthritis, and cuff tear arthroplasty). It has been reported that 0.5-2% of primary shoulder prosthesis will be complicated by a post-operative periprosthetic fracture (Katsumi *et al*., 2004 and Kent *et al*., 2005). The aim of shoulder prosthesis replacement is to restore normal kinematics with anatomic location and orientation of the humeral and glenoid joint surfaces. Correcting soft tissue tensioning and muscle tendon balancing by accurate reconstruction of the

normal anatomy will optimize the outcome of total shoulder arthroplasty (Laurent *et al*., 2001 and Lieven *et al*., 2003). In the design of prosthetic replacements for the proximal part of the humerus, the importance of accuracy in the normal three-dimensional anatomy must be emphasized, as shown in Figure 21 when a high shoulder prosthesis is used in the humeral bone.

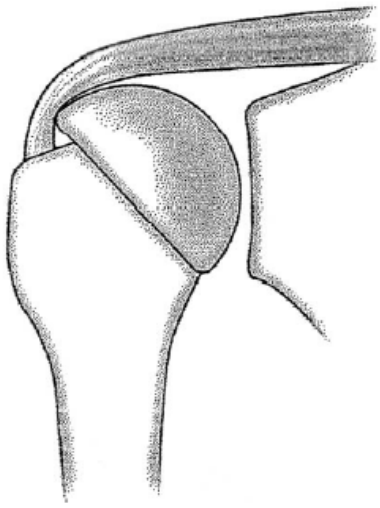

Figure 21 This shoulder prosthesis is too high, so the head rubs against the supraspinatus.

Source: Daniel *et al*. (2003).

This section is aimed at evaluating morphometric data on the Thai proximal humerus both intra- and extra-medullary. It uses the data obtained from computed tomography (CT). Advanced medical imaging and reverse engineering techniques were used to derive the internal geometry without destruction of the specimens.

1.10 Fit and Fill Analysis of Nail Insertion in the Thai Humerus: A Virtual Simulation Study

Humeral fractures as shown in Figure 22 have been treated variously ranging from conservative to operative methods, the latter including open reduction

and internal fixation with plate and screws, tension band wiring, intramedullary devices and prosthetic replacement.

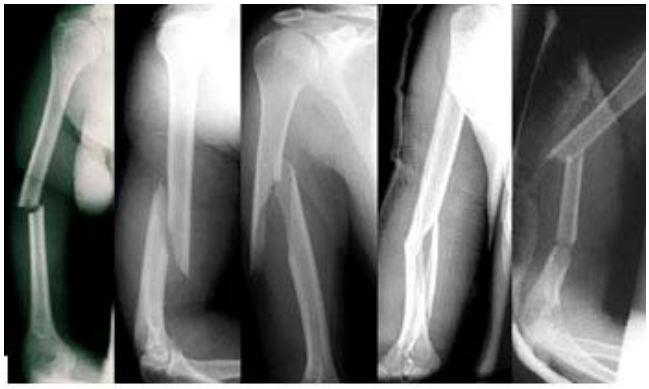

Figure 22 Type of humerus fracture: (A) transverse, (B) oblique, (C) spiral, (D) wedge, and (E) segmental.
Source: Flinkkila (2004).

The intramedullary fixation device is accepted as a minimally invasive treatment technique with low morbidity, providing simultaneously rapid recovery and prompt return to work and everyday life activities (Blum *et al*., 2000, Fernandez *et al*., 2003, Dimakopoulos *et al*., 2005, Reynolds and Jackson, 2005, and Verbruggen and Stapert, 2005). Intramedullary fixation of long bones has been increasingly preferred, especially following traumatic injuries and pathologic fractures. The fracture needs to be reduced and stabilized.

The morphometric study of the proximal Thai humerus showed that its dimensions were smaller and slightly different from those of the Caucasian humerus. This may create some clinical complications when implants are used in the Thai patient because the implant designs are mostly based on Caucasian morphometric data. This section aims to investigate the geometric mismatch of the standard humeral nail in the Thai humerus with the antegrade and retrograde insertion techniques using three-dimensional virtual simulation.

Antegrade insertion is a technique in which a humeral nail is inserted at the top margin of the anatomical neck of the humeral head, as shown in Figure 23, medial to the greater tuberosity, which is the best point for nail insertion (entry point).

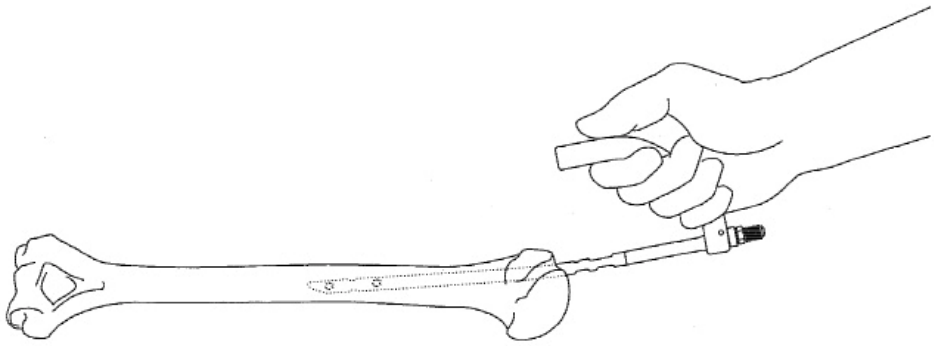

Figure 23 The nail is inserted after opening the medullary canal with antegrade insertion.

Source: Blum *et al*. (2000).

In retrograde insertion, the medullary canal was opened, and three holes were drilled perpendicular to the canal, as shown in Figure 24. The holes should form a triangle with its distal edge adjacent to the roof of the fossa. A nail was inserted from the distal to the proximal bone.

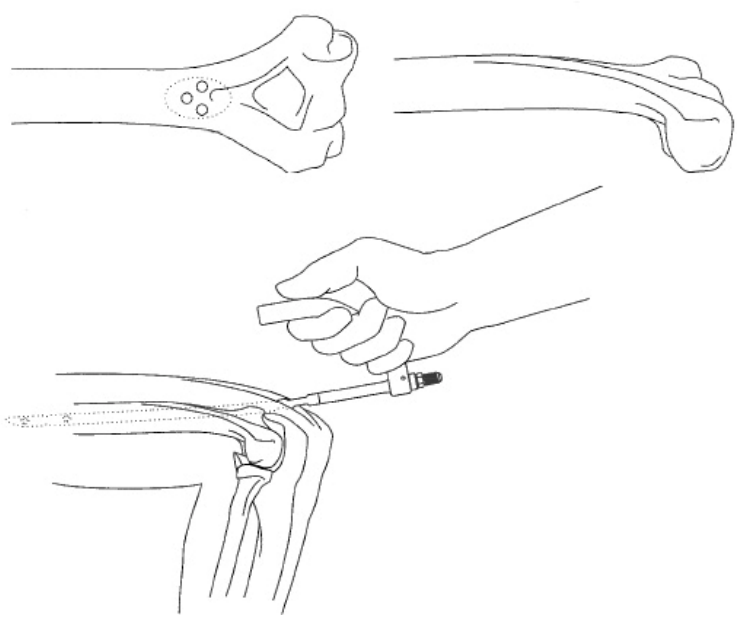

Figure 24 Three holes are drilled over the fossa (upper) and the nail is inserted in the medullary canal with retrograde insertion (lower).
Source: Blum *et al*. (2000).

1.11 An Advanced Method to Evaluate Three-dimensional Shape and Direction of the Rotator Cuff and the Deltoid Muscles: MRI 3 Tesla

The movement of shoulder represents a complex dynamic relationship of many muscular forces. It involves the scapula and the clavicle, which function as a stable base for the motions of the humerus. The stability of the shoulder joint must be effected through muscular action because the relevant joint capsule and ligaments are generally lax throughout the greater part of glenohumeral joint. The limitation of previous radiographic studies is that analysis has been restricted to one plane, although it is known that shoulder activation is a complex three-dimensional motion (Karlsson and Peterson, 1992, and Van der Helm and Pronk, 1995).

This section aims to analyze the three-dimensional shape of the rotator cuff (infraspinatus, subscapularis, and supraspinatus) and deltoid muscles, which are known to be primary movers in normal abduction (Kronberg et al., 1990) by using

magnetic resonance images (MRI) with normative data from a healthy volunteer to evaluate the direction of these muscles.

1.12 Measuring Muscle Force Active on the Thai Humerus Exerted by the Rotator Cuff and Deltoid Muscles

The glenohumeral joint is mainly stabilized by muscles, tendons and ligaments. The rotator cuff muscles oppose the superior pull of the deltoid muscle, maintaining the position of the humeral head in the glenoid socket during abduction (Hess, 2000). The first mechanical shoulder models were proposed at the end of the 19th century (Wuelker *et al*., 1993) using cadaveric specimens to test the muscular force (Wuelker *et al*., 1993, Debski *et al*., 1995, McMahon *et al*., 1995, Apreleva *et al*., 2000, Halder *et al*., 2000, Lee *et al*., 2000, Favre *et al*., 2005, Kedgley *et al*., 2007, Levasseur *et al*., 2007, Terrier *et al*., 2007, and Warner *et al*., 2007) as shown in Figure 25. A sling is used to represent the muscular force pulling the humerus and the effect on the implant (Walsh *et al*., 2006, Braunstein *et al*., 2007, and Seide *et al*., 2007). Any estimate of muscle force would depend on the biomechanical model chosen and the method used to measure such as an electromyographic (EMG) recording, the cross-sectional area of a muscle, mathematical predictions (Van der Helm and Veenbaas, 1991, Karlsson and Peterson, 1992, and Van der Helm, 1994), and direct measurements on the complex shoulder model.

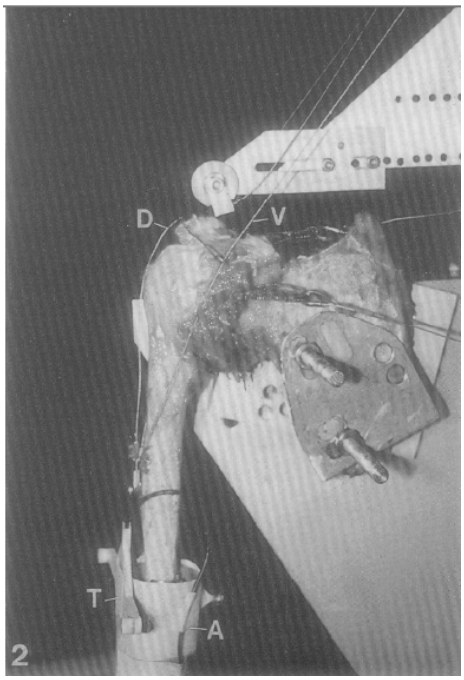

Figure 25 Cadaveric shoulder specimen mounted to a testing jig.
Source: Wuelker *et al*. (1993).

This section aims to measure the magnitude of muscular force exerted by the rotator cuff and deltoid muscles on the average Thai humeral bone model with static conditions at zero and ninety degrees abduction. The zero degrees abduction is the normal position of the upper extremity of the human being in any activity and the ninety degrees abduction is the most severe position.

1.13 Finite Element Analysis of the Thai Humerus at Zero and Ninety Degrees Abduction

When a humeral shaft fracture has occurred, fixation stability has been widely reported to influence the healing of the fracture, and by optimizing the mechanical conditions, it is believed that it may enhance healing (Einhorn, 1995, and Chao *et al*., 1998). New bone, required to stabilize and reunite the fragments, is formed either directly by intramembranous ossification or by way of a cartilage intermediate during endochondral ossification. For decades, nails have been the most

frequently used stabilizers for the surgical treatment for diaphyseal and metaphyseal fractures. They have been greatly improved in recent years and their indications have been widely extended (Hass *et al*., 1995). Many computational works, based on finite element analysis, have been made to determine the stress distribution on implants (Duda *et al*., 2001, Sitthiseripratip *et al*., 2002, Gupta *et al*., 2004, Gupta *et al*., 2004, J. Grasa *et al.*, 2005, and Perez *et al*., 2007) and bone (Buchler *et al*., 2002, Bitsakos *et al*., 2004, and Plausinis *et al*., 2005), and to determine the structure of bone healing (Claes and Heigele, 1998, Gardner *et al*., 1999, Gardner and Mishra, 2003, Gemez-Benito *et al.*, 2005, and Epari *et al*., 2006).

This section develops a three-dimensional finite element model of the humerus that consists of line action of rotator cuff and deltoid muscles to evaluate the stress distribution on the standard humeral nail and strain distribution on the Thai humerus with three gaps position in the mid-third region.

1.14 Design of a New Standard Humeral Nail Based on Thai Morphometric Data

Finite element analysis was used to test the Thai humerus with gaps simulating fractures at three levels and the standard humeral nail. We found that the standard humeral nail was strong enough to fix the fracture gap, but that the total strain on the gap in the most severe condition (ninety degrees abduction) was too high. So we developed a humeral nail using morphometric data on the Thai humerus such as radius of curvature and mediolateral angle and add a distal screw to increase the stability of the fixation system to reduce the total strain on the gap fracture as shown in Figure 26.

This section developed a proper design for a standard humeral nail based on geometric data on the Thai humerus and tested it with biomechanical data with FEA at ninety degree abduction with lower gap fracture condition.

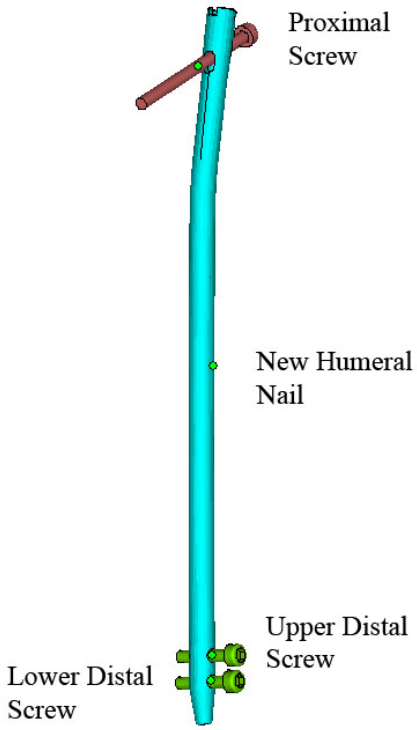

Figure 26 The new standard humeral nail with proximal and distal screws.

2. Related Theory

2.1 Finite Element Analysis (Bathe, 1996)

The finite element method is a numerical procedure for obtaining solution to many of the problems encountered in engineering analysis. It combines several mathematical concepts to produce a system of linear and nonlinear equations. In the finite element formulation we assumed that the nature of the boundary conditions remains unchanged during the application of the load on the finite element assemblage. With this assumption, the finite element equilibrium equation was derived for static analysis

$$\mathbf{KU} = \mathbf{R} \qquad (1)$$

This equation corresponds to a linear analysis of a structure problem because the displacement response U is a linear function of the applied load vector R, if the loads are αR instead of R, where α is a constant, the corresponding displacements are αU. When this is not case, we perform a nonlinear analysis.

A general nonlinear analysis is to find the state of equilibrium of a body corresponding to the applied loads. Assuming that the externally applied loads are described as a function of time, the equilibrium conditions of a system of finite elements representing the body under consideration can be expressed as

$$^{t}R - ^{t}F = 0 \qquad (2)$$

where the vector ^{t}R lists the externally applied nodal point forces in the configuration at time t and the vector ^{t}F lists the nodal point forces that correspond to the element stresses in this configuration.

Basic equations to be solve in nonlinear analysis are, at time t

$$^{t+\Delta t}R - ^{t+\Delta t}F = 0 \qquad (3)$$

where the vector $^{t+\Delta t}R$ stores the externally applied nodal loads and $^{t+\Delta t}F$ is the vector of nodal point forces that are equivalent to the element stresses. Both vector R and F are evaluated using the principle of virtual displacements. Since the nodal point forces $^{t+\Delta t}F$ depend nonlinearly on the nodal point displacements, it is necessary to iterate in the solution of ARTICLE? nonlinear analysis equation.

2.1.1 Newton-Raphson Schemes

The most frequently used iteration schemes for the solution of nonlinear finite element equations are the Newton-Raphson iteration

$$\Delta R^{(i-1)} = {}^{t+\Delta t}R - {}^{t+\Delta t}F^{(i-1)} \qquad \text{for i = 1, 2, 3,…} \qquad (4)$$

$${}^{t+\Delta t}K^{(i-1)}\Delta U^{(i)} = \Delta R^{(i-1)} \qquad (5)$$

$${}^{t+\Delta t}U^{(i)} = {}^{t+\Delta t}U^{(i-1)} + U^{(i)}$$

With

$${}^{t+\Delta t}U^{(0)} = {}^{t}U\,; \qquad {}^{t+\Delta t}F^{(0)} = {}^{t}F$$

These equations were obtained by linearizing the response of the finite element system about the conditions at time $t + \Delta t$, iteration $(i-1)$

The finite element equilibrium requirements amount to finding the solution of the equations

$$f(U^*) = 0 \qquad (6)$$

where $$f(U^*) = {}^{t+\Delta t}R(U^*) - {}^{t+\Delta t}F(U^*)$$

We denote here and in the following the complete array of the solution as U^* but realize that this vector may also contain variables other than displacements. Assume that in the iterative solution we have evaluated ${}^{t+\Delta t}U^{(i-1)}$; then a Taylor series expansion gives

$$f(U^*) = f({}^{t+\Delta t}U^{(i-1)}) + \left[\frac{\partial f}{\partial U}\right]_{{}^{t+\Delta t}U^{(i-1)}} (U^* - {}^{t+\Delta t}U^{(i-1)}) + \text{higher-order terms}$$

Substituting the equation, we obtain

$$\left[\frac{\partial F}{\partial U}\right]_{{}^{t+\Delta t}U^{(i-1)}}({U^*}-{}^{t+\Delta t}U^{(i-1)})+\text{higher-order terms}={}^{t+\Delta t}R-{}^{t+\Delta t}F^{(i-1)} \qquad (7)$$

where we assumed that the externally applied loads are deformation-independent. Neglecting the higher-order terms, we can calculate an increment in the displacements,

$${}^{t+\Delta t}K^{(i-1)}\Delta U^{(i)}={}^{t+\Delta t}R-{}^{t+\Delta t}F^{(i-1)} \qquad (8)$$

where ${}^{t+\Delta t}K^{(i-1)}$ is the current tangent stiffness matrix

$${}^{t+\Delta t}K^{(i-1)}=\left[\frac{\partial F}{\partial U}\right]_{{}^{t+\Delta t}U^{(i-1)}} \qquad (9)$$

and the improved displacement solution is

$${}^{t+\Delta t}U^{(i)}={}^{t+\Delta t}U^{(i-1)}+\Delta U^{(i)} \qquad (10)$$

The relation of ${}^{t+\Delta t}K^{(i-1)}\Delta U^{(i)}$ and ${}^{t+\Delta t}U^{(i)}$ constitute the Newton-Raphson solution of ${}^{t+\Delta t}R-{}^{t+\Delta t}F=0$. Since an incremental analysis is performed with time (or load) step of size Δt, the initial conditions in this iteration are ${}^{t+\Delta t}K^{(0)}={}^{t}K$, ${}^{t+\Delta t}F^{(0)}={}^{t}F$ and ${}^{t+\Delta t}U^{(0)}={}^{t}U$. The iteration is continued until appropriate convergence criteria are satisfied. A characteristic of this iteration is that a new tangent stiffness matrix is calculated in each iteration, which is why this method is also referred to as the full Newton-Raphson method.

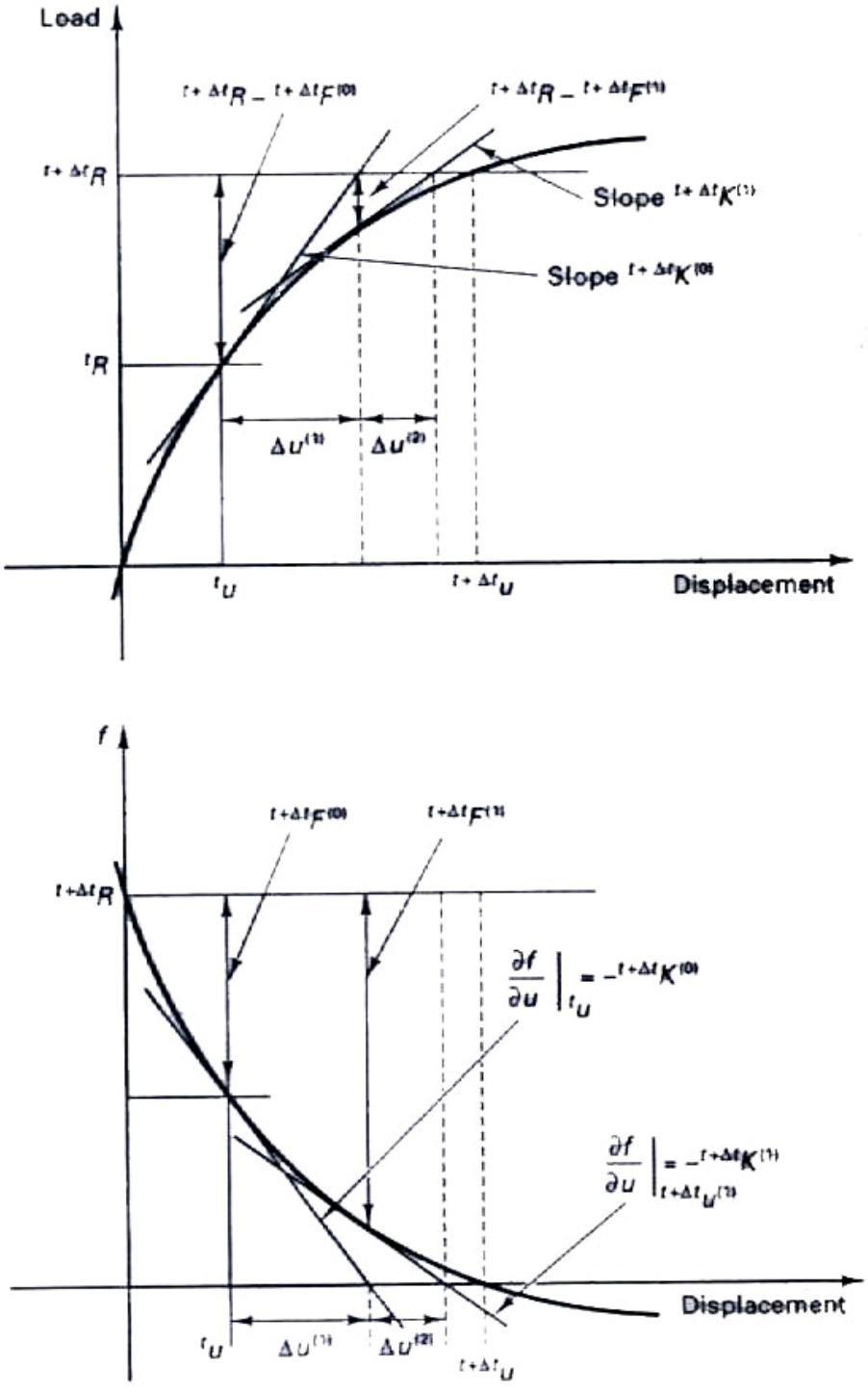

Figure 27 Illustration of Newton-Raphson iteration in the solution of a single degree of freedom system. (Top) Shows load-displacement relation. (Bottom) Shows iteration for zero of function f: $f = {}^{t+\Delta t}R - {}^{t+\Delta t}F(u)$.

Source: Bathe (1996).

Figure 27 illustrates the process of solution when used for a single degree of freedom system. The nonlinear response characteristics are such that convergence is rapidly obtained. However, we can imagine a more complex response characteristic with a starting point of iteration for which the procedure does not converge. Hence, the representation in Figure 27 is rather simplistic because a very special case is considered: that of a well-behaved single degree of freedom system. In the solution of systems with many degrees of freedom, the response curves will in general be rather non-smooth and complicated.

2.1.2 Element Types used in the FEA Simulation (Moaveni, 1999)

a) The four-node tetrahedral element is the simplest three-dimensional element used in the analysis of solid mechanic problems. This element has four nodes, with each node having three translational degrees of freedom in the nodal x, y, and z-directions. A typical four-node tetrahedral element is shown in Figure 28.

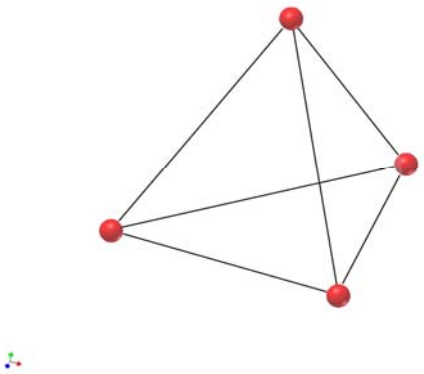

Figure 28 The four-node tetrahedral element.
Source: http://fea-cae-engineering.com.

b) The ten-node tetrahedral is a higher order version of the three-dimensional linear tetrahedral element. It modified four nodes tetrahedral element by inserting mid-side nodes on each element edge. Consequently, the obtained result is

more accurate than the four-node type due to the approximation method is second-order interpolation. A typical ten-node tetrahedral element is shown in Figure 29.

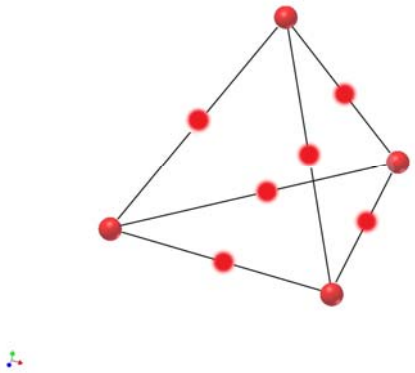

Figure 29 The ten-node tetrahedral element.
Source: http://fea-cae-engineering.com.

c) The eight-node hexahedral is the next simple three-dimensional element used in the analysis of solid mechanics problem. Each of the eight nodes of this element has three translational degrees of freedom in the nodal x, y, and z-directions. A typical eight-node hexahedral element is shown in Figure 30.

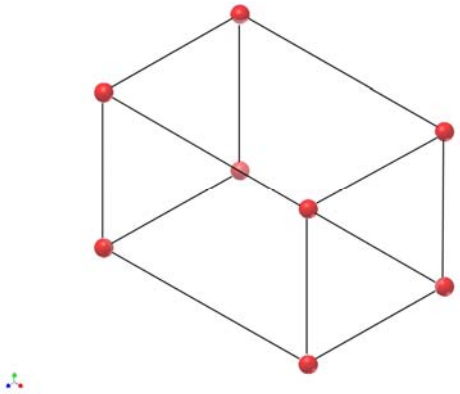

Figure 30 The eight-node hexahedral element.
Source: http://fea-cae-engineering.com.

d) The twenty-node hexahedral is a higher order version of the three-dimensional eight-node brick element. This element is more capable and more accurate for modeling problem with curved boundaries than the eight-node brick element. A typical twenty-node hexahedral element is shown in Figure 31.

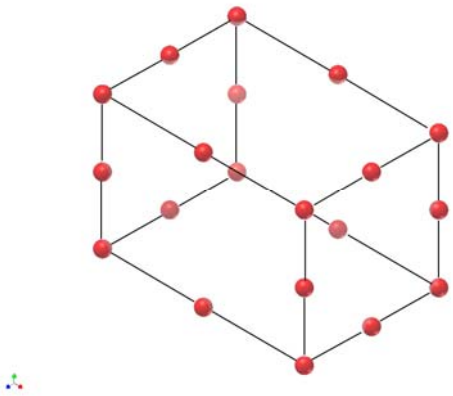

Figure 31 The twenty-node hexahedral element.
Source: http://fea-cae-engineering.com.

2.1.3 Analysis of Three-dimensional Solid Problem using The Four-Node Tetrahedral Elements

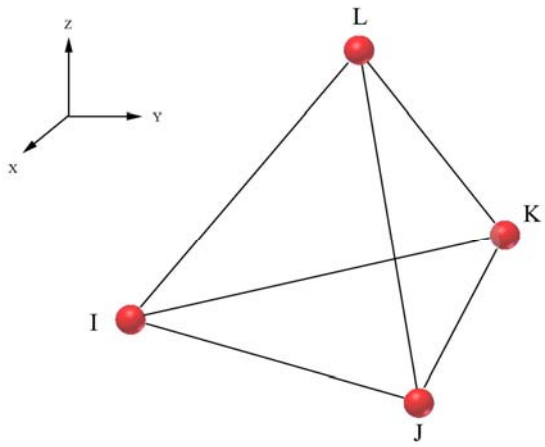

Figure 32 The four-node tetrahedral element.
Source: http://fea-cae-engineering.com.

The shape functions for two-dimensional problems. The displacement field is represented by following equations:

$$u = C_{11} + C_{12}X + C_{13}Y + C_{14}Z \tag{11}$$

$$v = C_{21} + C_{22}X + C_{23}Y + C_{24}Z \tag{12}$$

$$w = C_{31} + C_{32}X + C_{33}Y + C_{34}Z \tag{13}$$

Considering the nodal displacements, we must satisfy the following conditions:

$$\begin{array}{llllllll}
u = u_I & \text{at} & X = X_I & Y = Y_I & \text{and} & Z = Z_I \\
u = u_J & \text{at} & X = X_J & Y = Y_J & \text{and} & Z = Z_J \\
u = u_K & \text{at} & X = X_K & Y = Y_K & \text{and} & Z = Z_K \\
u = u_L & \text{at} & X = X_L & Y = Y_L & \text{and} & Z = Z_L
\end{array}$$

Similarly, we must satisfy the following requirements:

$$\begin{array}{llllllll}
v = v_I & \text{at} & X = X_I & Y = Y_I & \text{and} & Z = Z_I \\
\vdots & \vdots & \vdots & \vdots & \vdots & \vdots \\
w = w_L & \text{at} & X = X_I & Y = Y_I & \text{and} & Z = Z_I
\end{array}$$

Substitution of respective nodal values into equations u, v, and w results in 12 equations and 12 unknowns:

$$\begin{array}{c}
u_I = C_{11} + C_{12}X_I + C_{13}Y_I + C_{14}Z_I \\
u_J = C_{11} + C_{12}X_J + C_{13}Y_J + C_{14}Z_J \\
\vdots \\
w_L = C_{31} + C_{32}X_L + C_{33}Y_L + C_{34}Z_L
\end{array}$$

Solving for the unknown C-coefficients, substituting the result back into equations u, v, and w and regrouping the parameters, we obtain:

$$u = S_1 u_I + S_2 u_J + S_3 u_K + S_4 u_L \tag{14}$$

$$v = S_1 v_I + S_2 v_J + S_3 v_K + S_4 v_L \tag{15}$$

$$w = S_1 w_I + S_2 w_J + S_3 w_K + S_4 w_L \tag{16}$$

The shape functions are

$$S_1 = \frac{1}{6V}\left(a_I + b_I X + c_I Y + d_I Z\right) \tag{17}$$

$$S_2 = \frac{1}{6V}\left(a_J + b_J X + c_J Y + d_J Z\right) \tag{18}$$

$$S_3 = \frac{1}{6V}\left(a_K + b_K X + c_K Y + d_K Z\right) \tag{19}$$

$$S_4 = \frac{1}{6V}\left(a_L + b_L X + c_L Y + d_L Z\right) \tag{20}$$

where V, the volume of the tetrahedral element, is computed from

$$6V = \det\begin{vmatrix} 1 & X_I & Y_I & Z_I \\ 1 & X_J & Y_J & Z_J \\ 1 & X_K & Y_K & Z_K \\ 1 & X_L & Y_L & Z_L \end{vmatrix} \tag{21}$$

the $a_I, b_I, c_I, d_I, \ldots,$ and d_L -terms are:

$$a_I = \det\begin{vmatrix} X_J & Y_J & Z_J \\ X_K & Y_K & Z_K \\ X_L & Y_L & Z_L \end{vmatrix} \qquad b_I = -\det\begin{vmatrix} 1 & Y_J & Z_J \\ 1 & Y_K & Z_K \\ 1 & Y_L & Z_L \end{vmatrix}$$

$$c_I = \det\begin{vmatrix} X_J & 1 & Z_J \\ X_K & 1 & Z_K \\ X_L & 1 & Z_L \end{vmatrix} \qquad d_I = -\det\begin{vmatrix} X_J & Y_J & 1 \\ X_K & Y_K & 1 \\ X_L & Y_L & 1 \end{vmatrix}$$

We can present the $a_J, b_J, c_J, d_J, \ldots,$ and d_L-terms using similar determinants by rotating through the I, J, K, and L subscripts using the right-hand rule.

$$a_J = \det\begin{vmatrix} X_K & Y_K & Z_K \\ X_L & Y_L & Z_L \\ X_I & Y_I & Z_I \end{vmatrix}$$

The six independent stress components are needed to characterize the general state of stress at a point. These components are

$$[\sigma]^T = \begin{bmatrix} \sigma_{xx} & \sigma_{yy} & \sigma_{zz} & \tau_{xy} & \tau_{yz} & \tau_{xz} \end{bmatrix} \tag{22}$$

The displacement vector measured the change occurring in the position of a point within a body when the body is subjected to a load. The displacement vector, $\vec{\delta}$ can be written in terms of its Cartesian components as

$$\vec{\delta} = u(x,y,z)\vec{i} + v(x,y,z)\vec{j} + w(x,y,z)\vec{k} \tag{23}$$

The general state of strain is characterized by six independent components as given by

$$[\varepsilon]^T = \begin{bmatrix} \varepsilon_{xx} & \varepsilon_{yy} & \varepsilon_{zz} & \gamma_{xy} & \gamma_{yz} & \gamma_{xz} \end{bmatrix} \tag{24}$$

The relationship between the strain and the displacement is presented by

$$\varepsilon_{xx} = \frac{\partial u}{\partial x}, \qquad \varepsilon_{yy} = \frac{\partial v}{\partial y}, \qquad \varepsilon_{zz} = \frac{\partial w}{\partial z}$$

$$\gamma_{xy} = \frac{\partial u}{\partial y} + \frac{\partial v}{\partial x}, \qquad \gamma_{yz} = \frac{\partial v}{\partial z} + \frac{\partial w}{\partial y}, \qquad \gamma_{xz} = \frac{\partial u}{\partial z} + \frac{\partial w}{\partial x}$$

It can be represented in matrix form as

$$\{\varepsilon\} = LU \tag{25}$$

where

$$\{\varepsilon\} = \begin{Bmatrix} \varepsilon_{xx} \\ \varepsilon_{yy} \\ \varepsilon_{zz} \\ \gamma_{xy} \\ \gamma_{yz} \\ \gamma_{xz} \end{Bmatrix} \tag{26}$$

and

$$LU = \begin{Bmatrix} \dfrac{\partial u}{\partial x} \\ \dfrac{\partial v}{\partial y} \\ \dfrac{\partial w}{\partial z} \\ \dfrac{\partial u}{\partial y} + \dfrac{\partial v}{\partial x} \\ \dfrac{\partial v}{\partial z} + \dfrac{\partial w}{\partial y} \\ \dfrac{\partial w}{\partial x} + \dfrac{\partial u}{\partial z} \end{Bmatrix} \tag{27}$$

L is commonly referred to as the linear differential operator.

Over the elastic region of a material, there also exists a relationship between the state of stresses and strains, according to the generalized Hooke's Law. This relationship is given by the following equations:

$$\varepsilon_{xx} = \frac{1}{E}\left[\sigma_{xx} - \nu\left(\sigma_{yy} + \sigma_{zz}\right)\right] \tag{28}$$

$$\varepsilon_{yy} = \frac{1}{E}\left[\sigma_{yy} - \nu\left(\sigma_{xx} + \sigma_{zz}\right)\right] \tag{29}$$

$$\varepsilon_{zz} = \frac{1}{E}\left[\sigma_{zz} - \nu\left(\sigma_{xx} + \sigma_{yy}\right)\right] \tag{30}$$

$$\gamma_{xy} = \frac{1}{G}\tau_{xy}, \quad \gamma_{yz} = \frac{1}{G}\tau_{yz}, \quad \gamma_{zx} = \frac{1}{G}\tau_{zx}$$

The relationship between the stress and strain can be expressed in a compact-matrix form as:

$$\{\sigma\} = [v]\{\varepsilon\} \tag{31}$$

where

$$\{\sigma\} = \begin{Bmatrix} \sigma_{xx} \\ \sigma_{yy} \\ \sigma_{zz} \\ \tau_{xy} \\ \tau_{yz} \\ \tau_{xz} \end{Bmatrix} \tag{32}$$

$$[v] = \frac{E}{1+v}\begin{bmatrix} \frac{1-v}{1-2v} & \frac{v}{1-2v} & \frac{v}{1-2v} & 0 & 0 & 0 \\ \frac{v}{1-2v} & \frac{1-v}{1-2v} & \frac{v}{1-2v} & 0 & 0 & 0 \\ \frac{v}{1-2v} & \frac{v}{1-2v} & \frac{1-v}{1-2v} & 0 & 0 & 0 \\ 0 & 0 & 0 & \frac{1}{2} & 0 & 0 \\ 0 & 0 & 0 & 0 & \frac{1}{2} & 0 \\ 0 & 0 & 0 & 0 & 0 & \frac{1}{2} \end{bmatrix} \tag{33}$$

$$\{\varepsilon\} = \begin{Bmatrix} \varepsilon_{xx} \\ \varepsilon_{yy} \\ \varepsilon_{zz} \\ \gamma_{xy} \\ \gamma_{yz} \\ \gamma_{xz} \end{Bmatrix} \tag{34}$$

For a solid material under tri-axial loading, the strain energy Λ is

$$\Lambda^{(e)} = \frac{1}{2}\int_V \left(\sigma_{xx}\varepsilon_{xx} + \sigma_{yy}\varepsilon_{yy} + \sigma_{zz}\varepsilon_{zz} + \tau_{xy}\gamma_{xy} + \tau_{xz}\gamma_{xz} + \tau_{yz}\gamma_{yz}\right) dV \tag{35}$$

Or, in a compact-matrix form,

$$\Lambda^{(e)} = \frac{1}{2}\int_V \{\varepsilon\}^T [v]\{\varepsilon\} dV \tag{36}$$

We will now use the four-node tetrahedral element to formulate the stiffness matrix. Recall that this element has four nodes, with each node having three translational degrees of freedom in the nodal x, y, and z-direction. The displacements u, v, and w in terms of the nodal values and the shapes functions are represented by

$$\{\mathrm{u}\} = [S]\{U\} \tag{37}$$

where

$$\{\mathrm{u}\} = \begin{Bmatrix} u \\ v \\ w \end{Bmatrix} \tag{38}$$

$$[S]=\begin{bmatrix} S_1 & 0 & 0 & S_2 & 0 & 0 & S_3 & 0 & 0 & S_4 & 0 & 0 \\ 0 & S_1 & 0 & 0 & S_2 & 0 & 0 & S_3 & 0 & 0 & S_4 & 0 \\ 0 & 0 & S_1 & 0 & 0 & S_2 & 0 & 0 & S_3 & 0 & 0 & S_4 \end{bmatrix} \quad (39)$$

$$\{U\}=\begin{Bmatrix} u_I \\ v_I \\ w_I \\ u_J \\ v_J \\ w_J \\ u_K \\ v_K \\ w_K \\ u_L \\ v_L \\ w_L \end{Bmatrix} \quad (40)$$

In the next step, we begin by relating the strains to the displacement field and, in turn, to the nodal displacements through the shape functions. We need to take the derivatives of the components of the displacement field with respect to x, y, and z-coordinates according to the strain-displacement relation. The operation results in:

$$\begin{Bmatrix} \varepsilon_{xx} \\ \varepsilon_{yy} \\ \varepsilon_{zz} \\ \gamma_{xy} \\ \gamma_{yz} \\ \gamma_{xz} \end{Bmatrix} = \begin{bmatrix} \frac{\partial S_1}{\partial x} & 0 & 0 & \frac{\partial S_2}{\partial x} & 0 & 0 & \frac{\partial S_3}{\partial x} & 0 & 0 & \frac{\partial S_4}{\partial x} & 0 & 0 \\ 0 & \frac{\partial S_1}{\partial y} & 0 & 0 & \frac{\partial S_2}{\partial y} & 0 & 0 & \frac{\partial S_3}{\partial y} & 0 & 0 & \frac{\partial S_4}{\partial y} & 0 \\ 0 & 0 & \frac{\partial S_1}{\partial z} & 0 & 0 & \frac{\partial S_2}{\partial z} & 0 & 0 & \frac{\partial S_3}{\partial z} & 0 & 0 & \frac{\partial S_4}{\partial z} \\ \frac{\partial S_1}{\partial y} & \frac{\partial S_1}{\partial x} & 0 & \frac{\partial S_2}{\partial y} & \frac{\partial S_2}{\partial x} & 0 & \frac{\partial S_3}{\partial y} & \frac{\partial S_3}{\partial x} & 0 & \frac{\partial S_4}{\partial y} & \frac{\partial S_4}{\partial x} & 0 \\ 0 & \frac{\partial S_1}{\partial z} & \frac{\partial S_1}{\partial y} & 0 & \frac{\partial S_2}{\partial z} & \frac{\partial S_2}{\partial y} & 0 & \frac{\partial S_3}{\partial z} & \frac{\partial S_3}{\partial y} & 0 & \frac{\partial S_4}{\partial z} & \frac{\partial S_4}{\partial y} \\ \frac{\partial S_1}{\partial z} & 0 & \frac{\partial S_1}{\partial x} & \frac{\partial S_2}{\partial Z} & 0 & \frac{\partial S_2}{\partial x} & \frac{\partial S_3}{\partial z} & 0 & \frac{\partial S_3}{\partial x} & \frac{\partial S_4}{\partial z} & 0 & \frac{\partial S_4}{\partial x} \end{bmatrix}$$

substituting for the shape functions and differentiating, we have

$$\{\varepsilon\} = [B]\{U\} \tag{41}$$

where

$$[B] = \frac{1}{6V}\begin{bmatrix} b_I & 0 & 0 & b_J & 0 & 0 & b_K & 0 & 0 & b_L & 0 & 0 \\ 0 & c_I & 0 & 0 & c_J & 0 & 0 & c_K & 0 & 0 & c_L & 0 \\ 0 & 0 & d_I & 0 & 0 & d_J & 0 & 0 & d_K & 0 & 0 & d_L \\ c_I & b_I & 0 & c_J & b_J & 0 & c_K & b_K & 0 & c_L & b_L & 0 \\ 0 & d_I & c_I & 0 & d_J & c_J & 0 & d_K & c_K & 0 & d_L & c_L \\ d_I & 0 & b_I & d_J & 0 & b_J & d_K & 0 & b_K & d_L & 0 & b_L \end{bmatrix}$$

and the volume V and the b, c, and d-terms are given. Substituting into the strain energy equation for the strain components in terms of the displacements, we obtain

$$\Lambda^{(e)} = \frac{1}{2}\int_V \{\varepsilon\}^T [v]\{\varepsilon\} dV = \frac{1}{2}\int_V [U]^T [B]^T [v][B][U] dV \tag{42}$$

Differentiating with respect to the nodal displacements yields

$$\frac{\partial \Lambda^{(e)}}{\partial U_k} = \frac{\partial}{\partial U_k}\left(\frac{1}{2}\int_V [U]^T [B]^T [v][B][U]dV\right) \qquad \text{for k = 1, 2, …, 12}$$

Evaluation of the equation $\frac{\partial \Lambda^{(e)}}{\partial U_k}$ results in the expression $[K]^{(e)}\{U\}$ and, subsequently, the expression for the stiffness matrix, which is

$$[K]^{(e)} = \int_V [B]^T [v][B]dV = V[B]^T [v][B] \qquad (43)$$

where V is the volume of the element. The resulting stiffness matrix will have the dimensions of 12x12.

2.1.4 Load Matrix

The load matrix for a tetrahedral element is a 12x1 matrix. For a concentrated-loading situation, the load matrix is formed by placing the components of the load at appropriate nodes in appropriate directions. For a distributed load, the load matrix is computed from the equation

$$\{F\}^{(e)} = \int_A [S]^T \{p\}dA \qquad (44)$$

where

$$\{p\} = \begin{Bmatrix} p_x \\ p_y \\ p_z \end{Bmatrix} \qquad (45)$$

and A represents the surface over which the distributed-load components are acting. The surfaces of the tetrahedral element are triangular in shape. Assuming that the distributed load acts on the I-J-K surfaces, the load matrix becomes:

$$\{F\}^{(e)} = \frac{A_{I-J-K}}{3}\begin{Bmatrix} p_x \\ p_y \\ p_z \\ p_x \\ p_y \\ p_z \\ p_x \\ p_y \\ p_z \\ 0 \\ 0 \\ 0 \end{Bmatrix} \tag{46}$$

The load matrix for distributed load acting on the other surfaces of the tetrahedral element is obtained in a similar fashion.

MATERIALS AND METHODS

1. Three Dimensional Morphometric Study of the Thai Proximal Humerus: Anatomical Study

1.1 Three-Dimensional Modeling

Seventy-six Thai cadaveric humeri (38 rights and 38 lefts) from the Department of Anatomy, Faculty of Medicine, Siriraj Hospital were used in this study. The donors were 18 males, 15 females and five individuals of unknown sex; they ranged in age at the time of death from 22 to 79 years (average, 47.71). The humeri were scanned with a GE Light Speed Pro Series computerized tomographic (CT) scanner. None of the donors had had any surgical procedure performed on the humeri.

Figure 33 A set of twelve humeri in the CT machine.

Twelve humeri at a time were placed into an acrylic box as shown in Figure 33 and scanned. CT sections were available for the humeri with a spacing of 0.625-mm slice thickness. The inner and outer contours were identified by different

thresholding methods from the CT images. The CT data were transferred to medical image processing software (Mimic, Materialise N.V., Belgium) and then exported as stereolithography (STL) files.

Each humeral model, stl file, was imported into reverse engineering CAD software and displayed as a point cloud. The shape of each specific portion of the humerus was approximated with a simple geometric configuration, such as a circle, an ellipse, or a sphere, that best fit the real geometry.

The *fit sphere* function, which is the optimal least squares spherical approximation to a three-dimensional point cloud, was applied to derive the geometric data of the humeral head. The *fit cylinder* function, which is the optimal least squares cylindrical approximation to a three-dimensional point cloud, was applied to derive the straight portion of the intramedullary canal of the proximal humerus. The *fit circle* function, which is the optimal least squares circular approximation to two-dimensional point cloud, was applied in the humeral shaft region. The details of each step are summarized below:

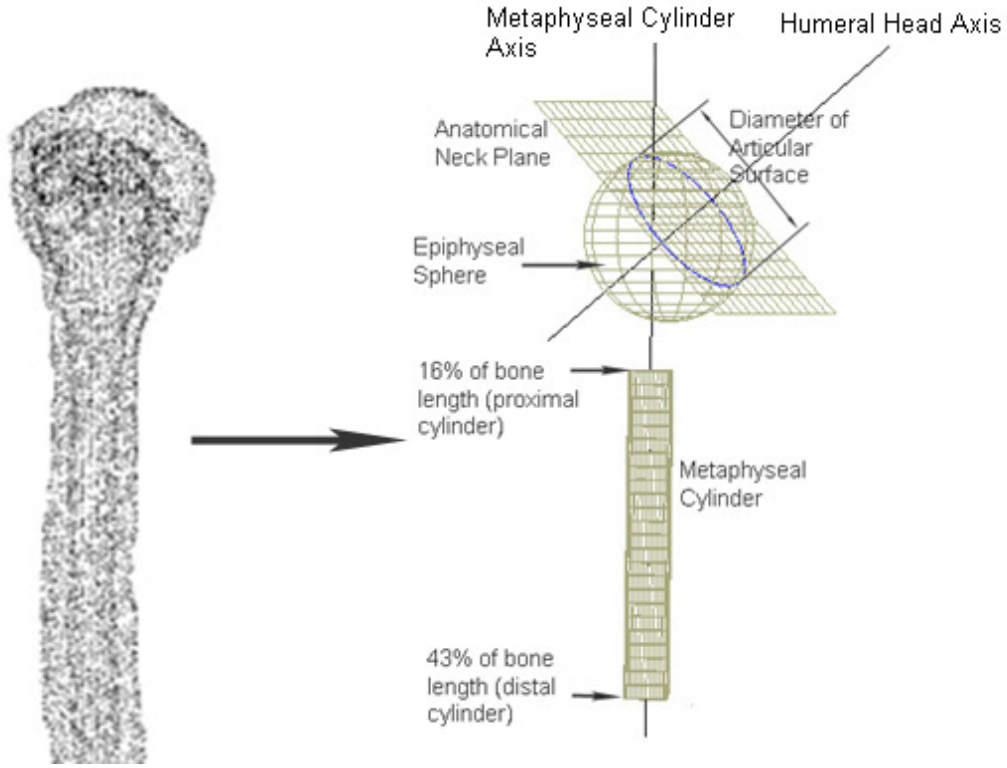

Figure 34 Cloud point of the humerus approximated with simple geometric shapes.

a) The first step was to determine the ***"anatomical neck plane"***, which was the best plane fit to the periphery of the articular surface as shown in Figure 34.

b) The second step was to determine the sphere that best fit the humeral head; this is called the ***"epiphyseal sphere"*** and is shown in Figure 34. The humeral head diameter, the center of rotation, and the humeral head axis, which was the perpendicular distance from the anatomical neck plane to the periphery of the epiphyseal sphere were derived, and the intersection area of the anatomical neck plane and epiphyseal sphere gave the ***"diameter of articular surface"*** and the ***"articular surface thickness"***.

c) The third step was to determine the cylinder that best fit the upper intramedullary canal, which is called the ***"metaphyseal cylinder"***. This cylinder was limited to the proximal half of the bone because there is a change in curvature in

the coronal plane. It extended from 16% to 43% of the length of the humerus, from the tip of humerus as shown in Figure 34. From the canal axis and the anatomical neck plane axis, the ***"inclination angle"***, the ***"mediolateral angle"***, the ***"medial and posterior offset"*** was derived.

d) The fourth step was to determine the cross sections of the intramedullary canal; fit circles were used to fit each section. From the centers of all sections, the ***"curve length"*** and the ***"radius of curvature"*** were derived.

e) The final step was to create a line at the distal part of the humerus from the medial epicondyle to the lateral epicondyle, called the ***"transepicondylar axis"*** and another line at the distal part of humerus from the capitulum to the trochlea, called the ***"tangent elbow axis"***. From these, the "***retroversion angles"*** were derived.

1.2 Measurements of the Proximal Humerus

After geometric simplification of the CAD models of the humerus, the dimensions of each studied parameter were measured in three-dimensions. The 11 morphometric parameters of the humerus (Boileau and Walch, 1997) were measured as follows:

a) The Diameter of the Humeral Head as shown in Figure 34 was the diameter of the epiphyseal sphere. This also determined the center of rotation.

b) The Diameter of the Articular Surface as shown in Figure 34 was the diameter of the circle on the anatomical neck plane. This circle was the intersection of the epiphyseal sphere with the anatomical neck plane.

c) The Articular Surface Thickness as shown in Figure 35 was the perpendicular distance from the center of the circle of the anatomical neck plane to the apex of the epiphyseal sphere. This thickness represented the distance of insertion of the humeral head into the rotator cuff.

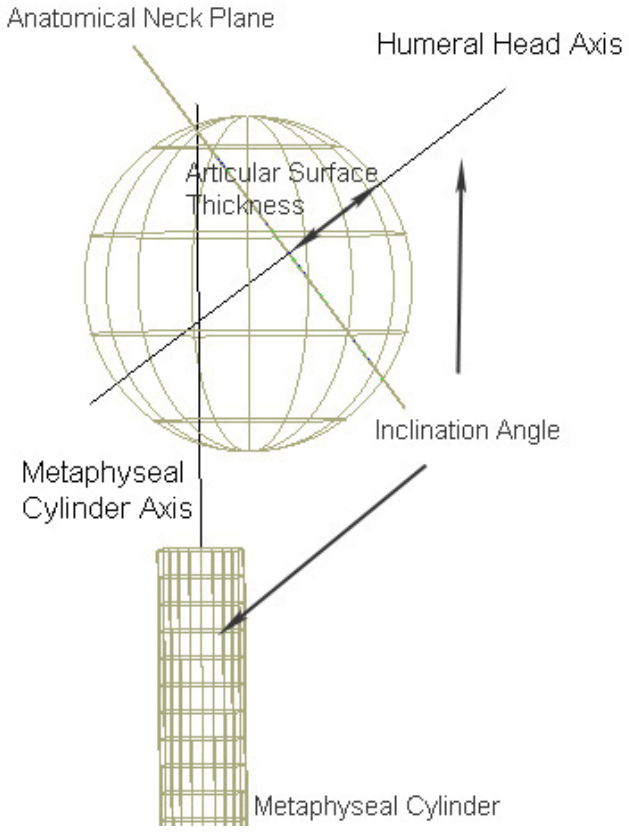

Figure 35 The articular surface thickness and the inclination angle were measured with simple geometric shapes.

d) The Inclination Angle as shown in Figure 35 was the angle between the metaphyseal cylinder axis and the humeral head axis.

e) The Retroversion Angle (Transepicondylar; B1), shown in Figure 36, was the angle between the humeral head axis and the transepicondylar axis.

f) The Retroversion Angle (Tangent Elbow: B2), shown in Figure 36, was the angle between the humeral head axis and the tangent elbow axis.

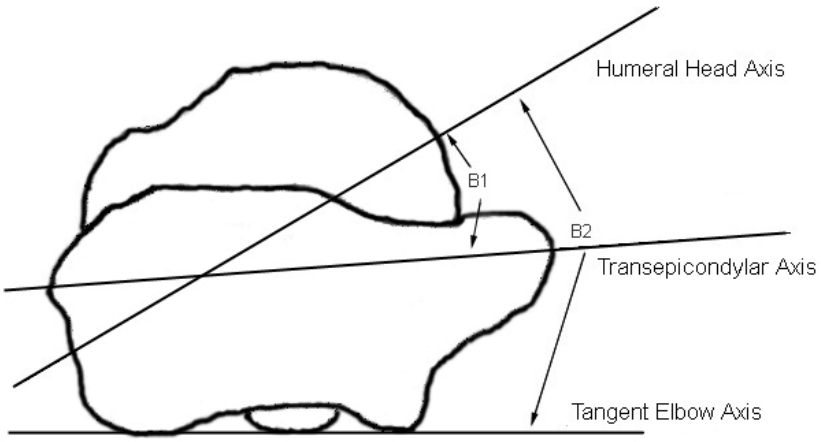

Figure 36 The retroversion angles at the distal humerus.

g) The Medial Offset, shown in Figure 37, was the perpendicular distance on the axial plane between the center of the epiphyseal sphere and the central axis of the metaphyseal cylinder.

h) The Posterior Offset, shown in Figure 37, was the perpendicular distance on the coronal plane between the center of the epiphyseal sphere and the central axis of the metaphyseal cylinder.

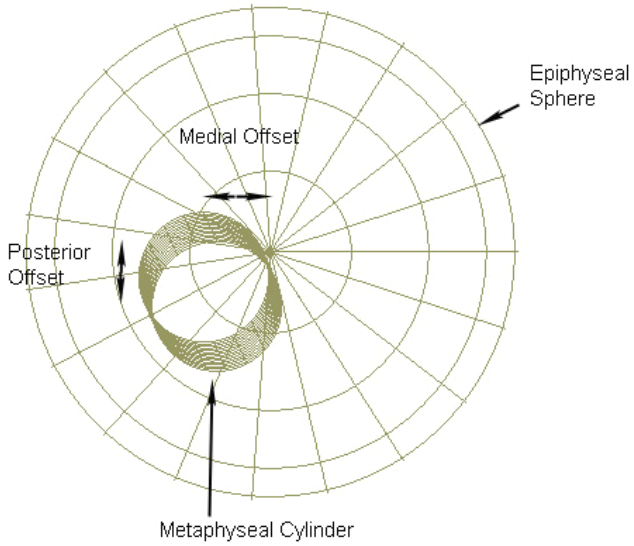

Figure 37 Medial and posterior offset of the humerus.

i) The Curve Length, shown in Figure 38, was the length of the intramedullary canal axis.

j) The Radius of Curvature was the radius of the curve length.

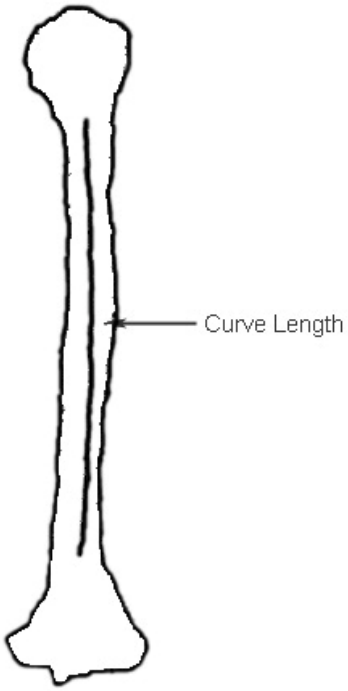

Figure 38 The curve length of the intramedullary canal.

k) The Mediolateral Angle, as shown in Figure 39, was the angle between the entry point and the metaphyseal cylinder axis (Leung *et al*., 1996), the entry point being the point on the top margin of the anatomical neck of the humeral head, medial to the greater tuberosity, which is the best point for antegrade nail insertion (See also Figure 23 in Chapter 2 above).

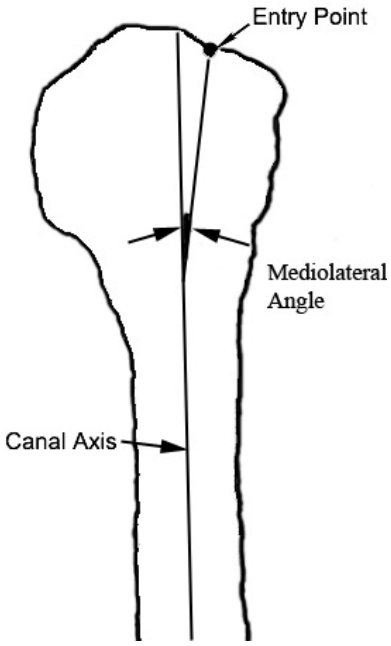

Figure 39 The mediolateral angle was measured from the entry point.

2. Fit and Fill Analysis of Nail Insertion in the Thai Humerus: A Virtual Simulation Study

2.1 Three-Dimensional Modeling

The cadaveric humeral database from the previous section was used to investigate virtual simulation of humeral nail insertion. The standard humeral nail was created with a Kreon KZ50 3D Laser Scanner combined with a Cimcore 3000i articulated arm, as shown in Figure 40. Cloud point collection was performed, and the data exported in STL format in the same way as the bone data.

Figure 40 The laser scanner was used to scan the standard humeral nail.

2.2 Anatomic Measurement Technique

A three-dimensional reverse engineering technique was applied for anatomic measurement of a three-dimensional reconstructed humerus obtained from CT medical images and imported into computer aided design (CAD) software for analysis. To determine the medullary canal axis (MCA), 20 cross sections of the humeral shaft were analyzed. The cross sections started 50 mm below the highest portion of the humeral head and continued in cranial to caudal direction. To each cross section, a circle was fitted with the use of a least squares circle-fitting routine, and a line, called "MCA," was passed through the center of each cross section as shown in Figure 41.

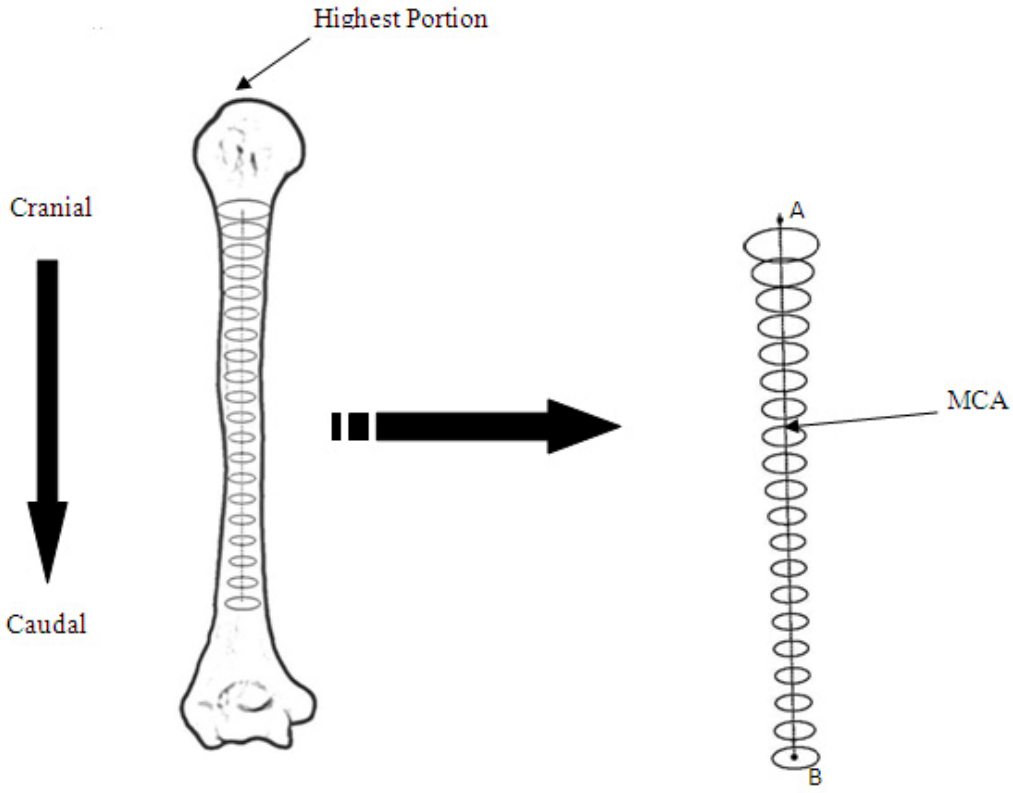

Figure 41 Cross sections of the humerus medullary canal were used to create the medullary canal axis (MCA).

The humeral head axis (HHA) as shown in Figure 42 was derived from the geometric center of the humeral head and anatomical neck. The humeral head was evaluated as a sphere with a least-square fit method, and from this sphere, the humeral head center (HHC) was obtained. The anatomical neck was estimated as a circle by using the best fitting circle with minimum error at the narrowest portion, and from this circle, the anatomical neck center (ANC) and entry point were obtained. Considering the orientation of the circle in three dimensional space, the highest point of the circle in the caudal to cranial direction was defined as the "*entry point*". The centers of the humeral head and the anatomical neck obtained were connected, and the line derived was defined as the "*Humeral head axis*".

In the distal portion of the humerus, the olecranon fossa was evaluated as a sphere by selecting points from the posterior side. The selected points were located around the fossa, which was drawn as a closed loop. A least squares method was used

to determine the geometric center of the olecranon fossa, and this was defined as the "*Fossa center*" and is shown in Figure 43.

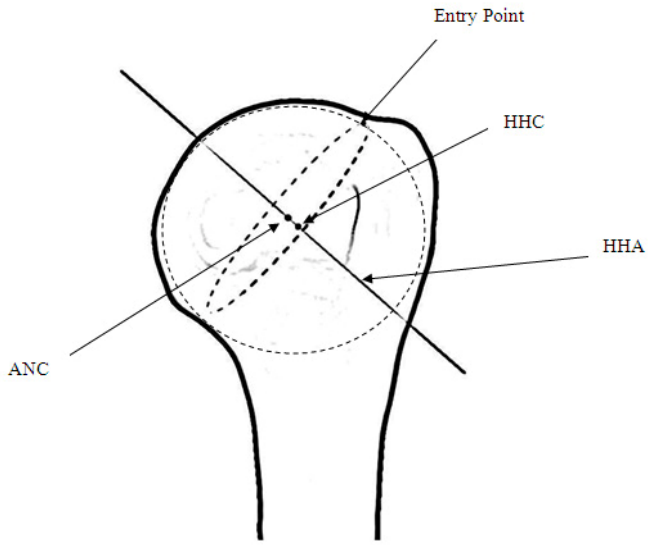

Figure 42 The proximal humerus showing the parameters of the humeral head.

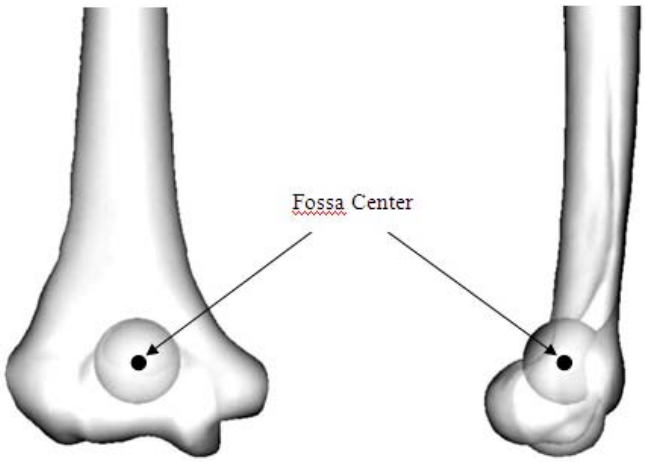

Figure 43 The best fit sphere for the olecranon fossa.

2.3 Measurement of Parameters

a) From anatomic measurement, three significant points were obtained: the end points of the medullary canal axis (MCA) and the entry point. These three points generated a plane that was defined as the "*Antegrade Plane*" and is shown in Figure 44.

b) The two end points of the MCA and the fossa center point generated the plane that was defined as the "*Retrograde Plane*" and is shown in Figure 45.

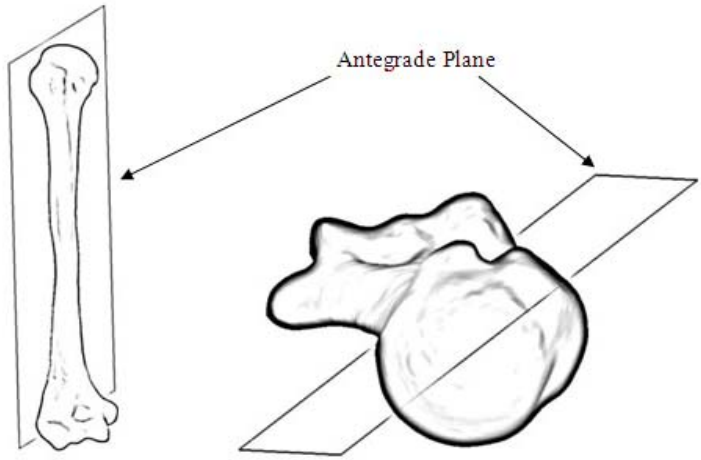

Figure 44 The antegrade plane of the humerus was generated from the two end points of the MCA and the entry point.

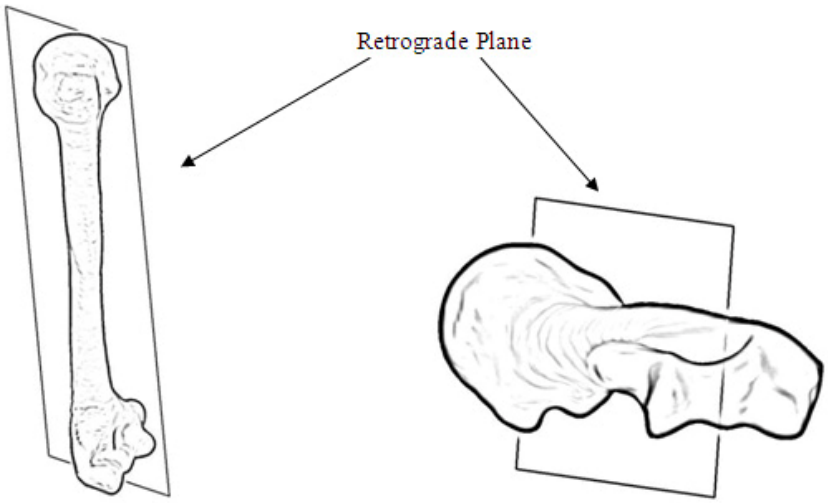

Figure 45 The retrograde plane of the humerus was generated from the two end points of the MCA and the center of fossa.

c) The nail axis was used in a least square fit geometry method in order to determine the "*Nail Plane*," as shown in Figure 46.

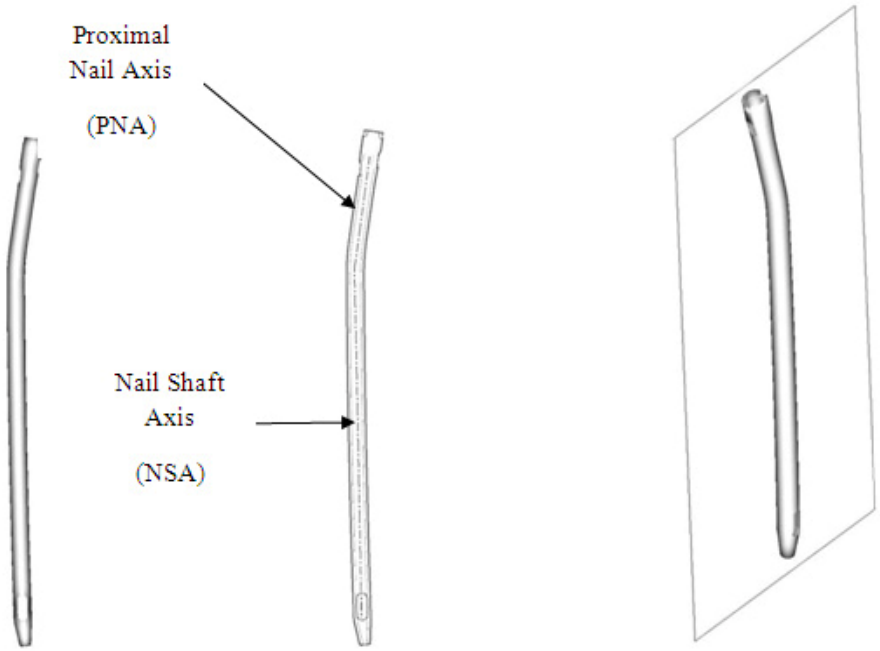

Figure 46 The nail plane was created from the humeral nail axis.

2.4 A Virtual Simulation

A three-dimensional reverse engineering technique was used to insert a model humeral nail into the model humerus, There are two techniques for humeral nail insertion: antegrade and retrograde insertion.

The antegrade insertion method may be detailed as follows:

a) The first step was to align the NSA of the humeral nail with the MCA by best fit function as shown in Figure 47.

b) The second step was to translate the MCA until the proximal end region of the nail passed through the humeral head.

c) The final step was to rotate the nail plane and the antegrade plane until they were coincident.

The retrograde insertion method may be detailed as follows:

a) In the first step, the NSA of the humeral nail was aligned with the MCA by best fit function. The humeral nail was oriented in a direction the reverse of that in antegrade insertion.

b) In the second step, the MCA was translated until the proximal end of the nail was located 5-mm above the olecranon fossa.

c) In the final step, the nail plane and the retrograde plane were rotated until they were coincident. The position of nail in retrograde insertion is shown in Figure 48.

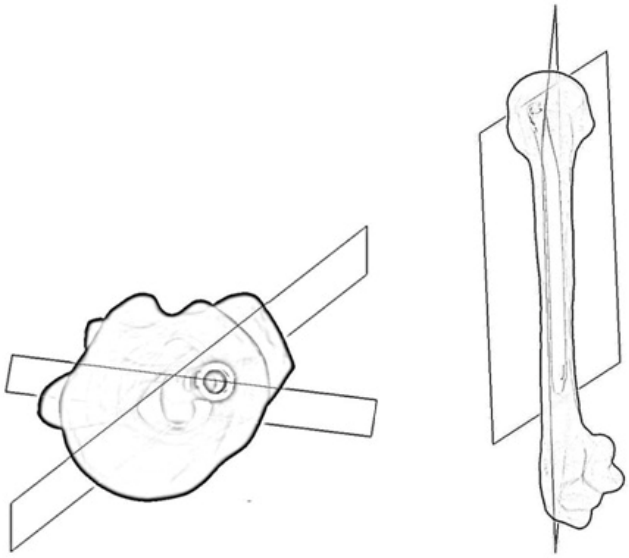

Figure 47 Antegrade insertion showing the optimal position with two planes coincident.

Figure 48 The optimal position of retrograde insertion, the proximal end of the nail 5-mm above the fossa.

In considering insertion of the humeral nail into the intramedullary canal, cross-sections of the humerus beginning at 50 mm from the highest point on the

humeral head (the initial of medullary canal) to 280 mm. (the end of the medullary canal) at 10-mm intervals from proximal to distal part were created. For each section, the circumferences of the nail and of the medullary canal were superimposed, as shown in Figure 49.

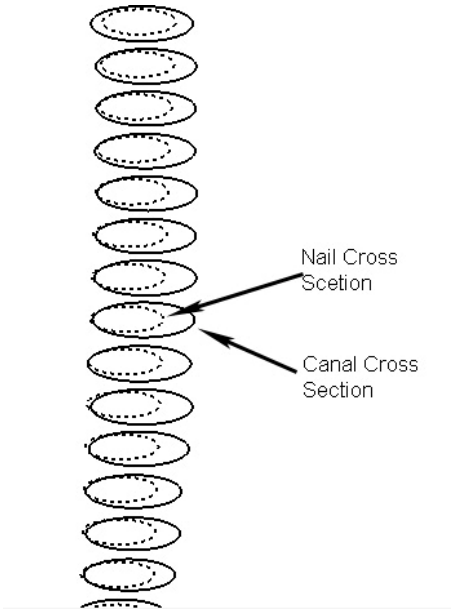

Figure 49 Circles of the medullary canal and the nail in antegrade insertion.

To determine the circular best fit for each section, the following data were collected: 1) the diameter of the medullary canal, 2) the minimal reaming diameter to accommodate the insertion of the nail virtually, 3) the minimal reaming thickness of the inner cortex, 4) the percentage of cortical bone removal prior to nail insertion and 5) the eccentric of the nail-medullary canal center (Mahaisavariya *et al*., 2004). All parameters are shown in Figure 50 and were calculated by using Equations 47-50.

Minimal reaming diameter

$$= 2 \times (\text{Radius}_{\text{canal}} + \text{Distance}_{\text{out of centricity}}) \quad (47)$$

Minimal inner cortical reaming thickness

$$= (\text{Minimal reaming dia.} - \text{Medullary canal dia.})/2 \quad (48)$$

% Bone removal

$$= \%[(\text{Area}_{\text{minimal reaming}} - \text{Area}_{\text{canal}})/\text{Area}_{\text{canal}} \quad (49)$$

The deviation of the nail center from the canal center

$$= \text{Position}_{\text{canal center}} - \text{Position}_{\text{nail center}} \quad (50)$$

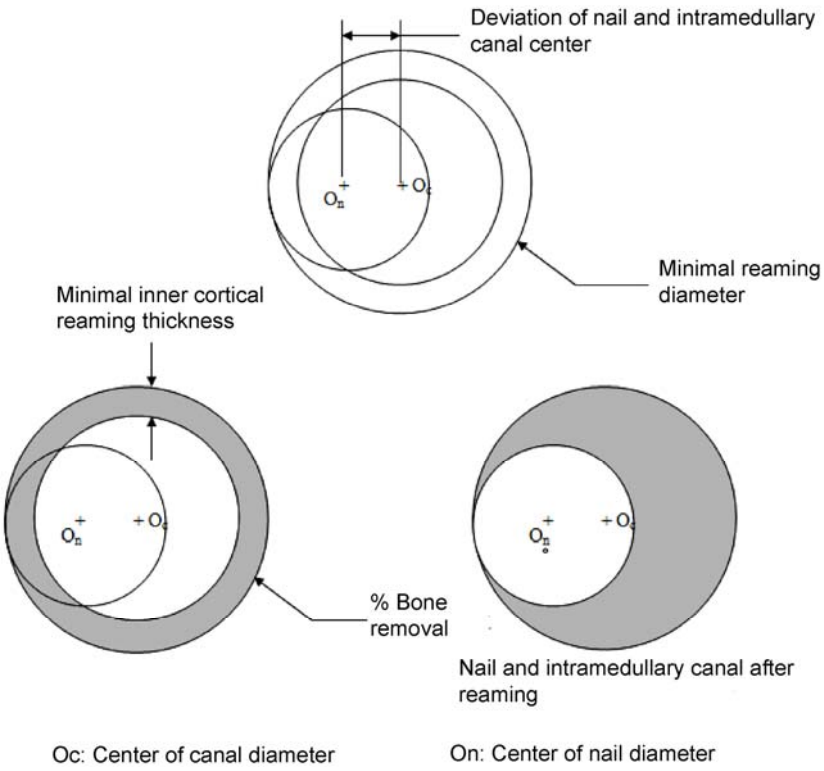

Figure 50 The parameters of fit and fill analysis data shown as the circle of nail and canal for each section.

3. An Advanced Method to Evaluate the Three Dimensional Shape and Direction of the Rotator Cuff and Deltoid Muscles: MRI 3 Tesla

A volunteer, aged 32 years, lying on a standard bed with zero degree abduction as shown in Figure 51, was scanned with a Magnetic Resonance Imaging (MRI) 3 Tesla scanner (Philips Achieva), a high field strength machine providing faster and better scanning for contour of muscle.

Figure 51 MRI 3 Tesla scanner (Philips Achieva).

After scanning, the data was imported into medical image processing software (Mimic, Materialize N.V.). Each section for the muscle around the humerus was available with a spacing of 0.398-mm slice thickness. To optimize the contour of muscle shape (Figure 52), two housefield values were applied to find the inner and outer contour of each section, and the results were exported to form the three-dimensional model as shown in Figure 53.

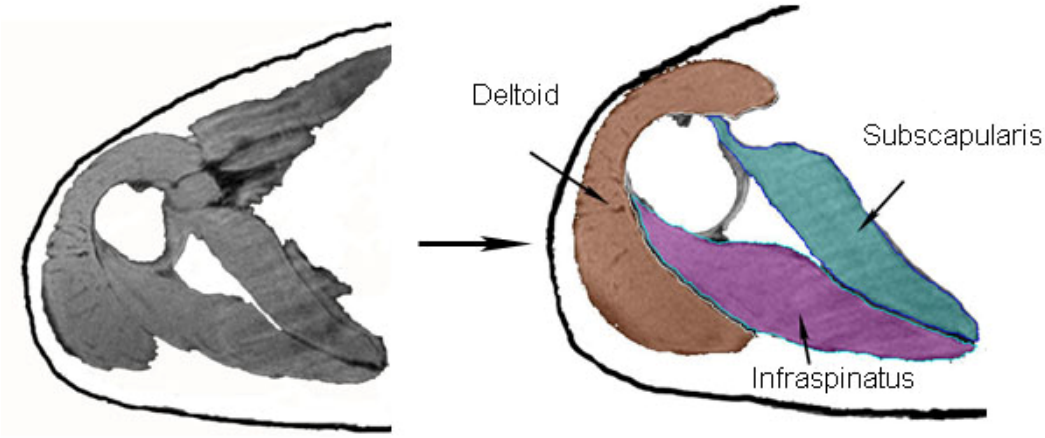

Figure 52 Contour of muscle from MRI 3 Tesla and the region growing of each muscle, showing the shape of muscle.

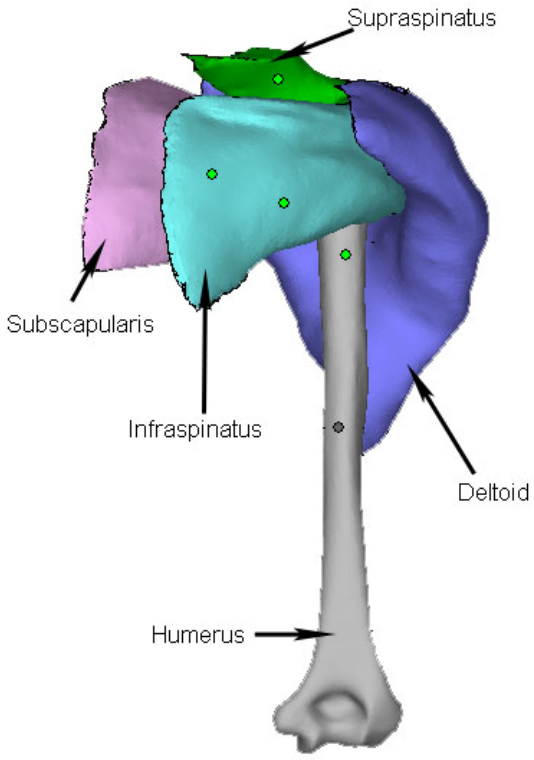

Figure 53 Three-dimensional model of the rotator cuff and deltoid muscles around the humerus.

From the three-dimensional shape, cross sections of each muscle were used to optimize the circular fit. For each section, the center line was derived and was fit for determination of the muscle axis, shown in Figure 54.

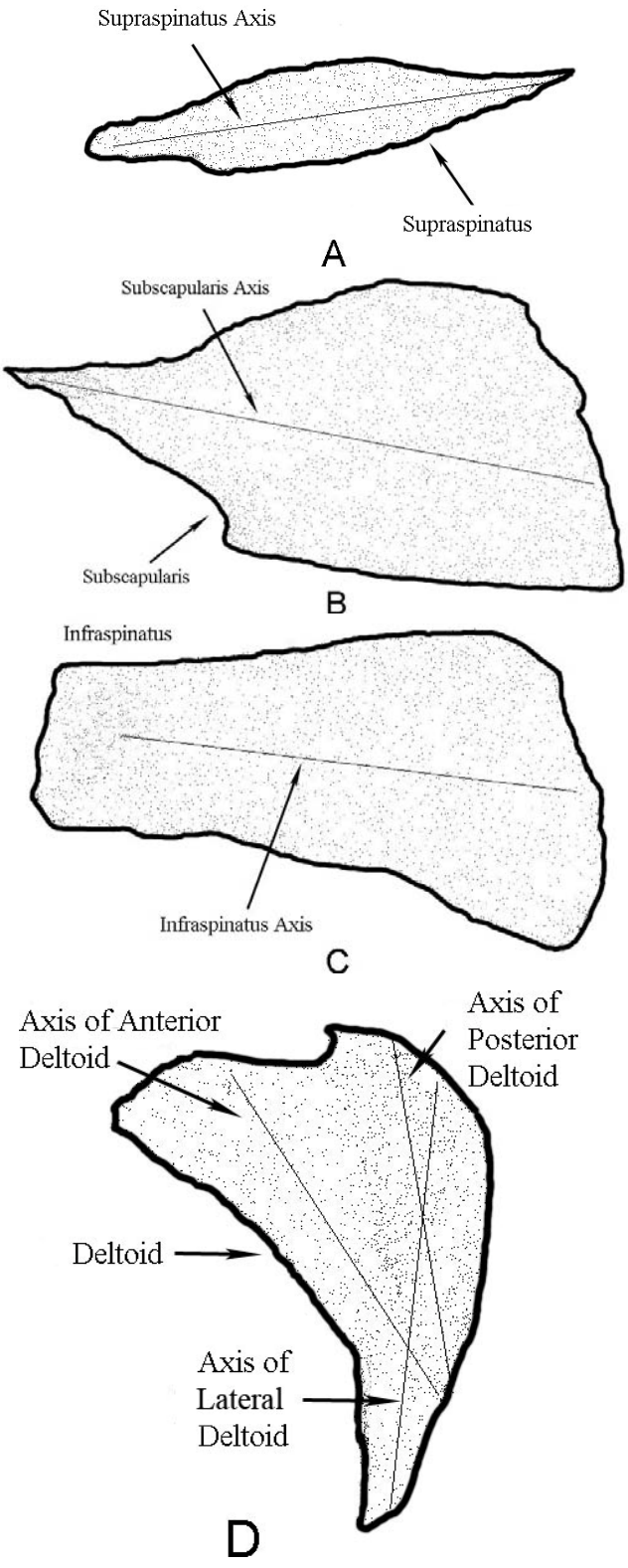

Figure 54 Directions of the axes of the rotator cuff and deltoid muscles: A) Supraspinatus, B) Subscapularis, C) Infraspinatus, and D) Deltoid.

4. Measuring Muscle Force Active on the Thai Humerus Exerted by the Rotator Cuff and Deltoid Muscles

4.1 Model Preparation

In this study, the model was developed from the seventy-six Thai dry cadaveric humeral bones. The average model was constructed with a rapid prototype (RP) technique and used to create a silicone mold as shown in Figure 55 for casting the mechanical test model.

Figure 55 The silicone mold from the RP model was used to construct the testing model.

The mechanical test model consisted of two layers, as shown in Figure 56, with spongy and dense layers like a real bone. For the spongy layer, polyurethane that had bubbles in it and properties like those of cancellous bone was used. For the dense layer, another type of polyurethane with no bubbles in it and properties like those of cortical bone was used. Hooks were inserted in the humeral head to which to were attached slings to represent the muscular force of the rotator cuff muscles as shown in Figure 57 and also at the mid-shaft to represent the deltoid muscle.

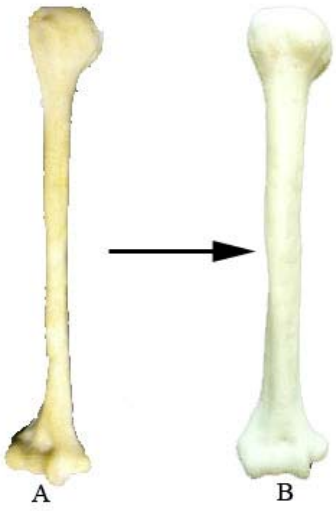

Figure 56 The mechanical test model consisted of (A) Cancellous bone and (B) Cortical bone.

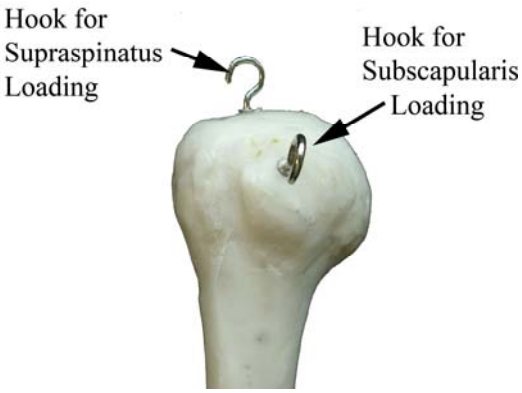

Figure 57 The mechanical test model with hooks to use for sling loading.

4.2 Testing Device

A Cartesian coordinate system referenced to the humerus was used to define the lines of action of forces, and the resulting turning moments. It was defined as follows for the right shoulder and is shown in Figure 58:

- The origin is the center of rotation of the humeral head.
- The X-axis lies in the scapular plane and is directed from medial to lateral.
- The Z-axis is directed caudal to cranial.
- The Y-axis follows the right-hand rule (directed anterior).

Figure 58 Three axes of the right humeral model.

The static shoulder testing apparatus consisted of a rigid frame and a glenohumeral mounting that allowed for anatomic positioning of the humerus to simulate normal abduction. Muscle force vectors for the rotator cuff and deltoid were based on prior anatomic and magnetic resonance imaging studies of the shoulder. The humerus testing device was designed with CAD software and constructed with an aluminium frame. The CAD software was used to find the direction of the muscles so the slings could be extended enough to accommodate the load cells and adjusters. The test apparatus is shown in Figure 59.

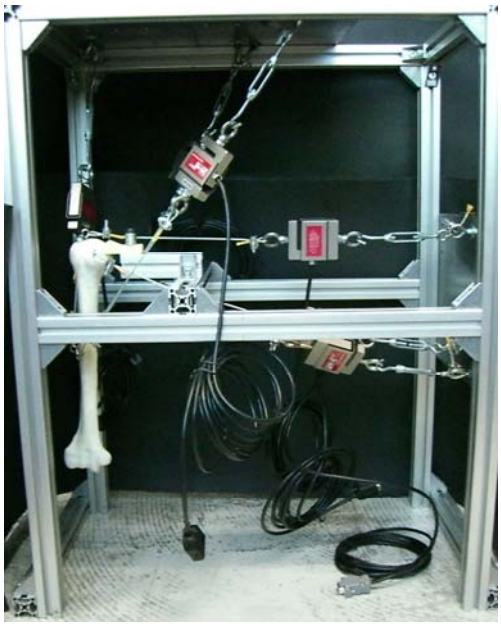

Figure 59 Aluminium framework for evaluating the muscular force at abduction status.

Weights were attached with slings at the distal humerus. The weight of the arm equals approximately 5% of body weight (Inman *et al*., 1944, Doody *et al*., 1970, Deluca and Forrest, 1973, Poppen and Walker, 1978, and Ringelberg, 1985). For all conditions, the force applied to the deltoid, infraspinatus, subscapularis, and supraspinatus remained constant to provide a stabilizing force couple during active abduction and to eliminate the effect that each of these muscles would have on abduction.

Each sling carried a load of muscular force and had a load cell in line to register the load occurring as shown in Figure 60. The data were transferred to a data locker as shown in Figure 61. The slings had an adjuster to adjust the load to obtain the optimum position.

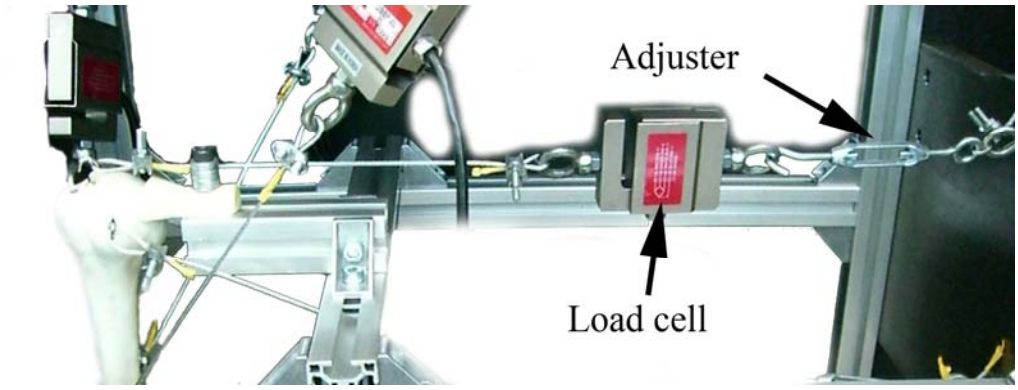

Figure 60 Sling connected to the side plate with a load cell and adjuster.

Figure 61 A computer connected to a data locker to convert the data.

The humeral model was hung by a sling so that the humeral head pressed into the socket representing the glenohumeral. All of the slings were adjusted to the tightest until the model lay parallel to the Z-axis for zero degrees or normal to the Z-axis for ninety degrees abduction. The data recorded from each sling showed the raw data of force magnitude. All data was transferred to a spreadsheet. The output from the data locker (in unit of mV/V) was converted to Newton units. Each load cell gave the magnitude of the muscular force, which is shown in Tables 10 and 11.

5. Finite Element Analysis of the Thai Humerus at Zero and Ninety Degrees Abduction

To fully understand the reasons behind the greater biomechanical stability afforded by the standard humeral nail, a finite elements study was conducted. Four finite element models were developed in which the geometry and position of the humerus, bone material properties, nail geometry, nail location, gap positions, loading and boundary conditions were identical while the humerus position was varied to zero and to ninety degrees abduction, the gap position was varied in mid-third region (Verbruggen and Stapert, 2005) with upper, medium, and lower gaps, and nail location was varied to antegrade and retrograde insertion. All finite element models were constructed by MSC PATRAN 2005 and all analyses were performed by MSC MARC/MENTAT 2005 finite element software packages.

5.1 Finite Element Model

The computer aided design (CAD) model of a three-dimensional humerus was the model of the average Thai humerus, which was created from the CT scans of 76 Thai cadaveric humeri. The humerus model consisted of cortex and cancellous layers. The set of internal fixation consisted of the standard humeral nail and the proximal and distal screws. The defect locations were evenly distributed along the humerus axis. Fractures were represented by 5 mm gaps (Lin *et al*., 1997, and Maldonado *et al*., 2003) in the mid-third region, as shown in Figure 62. Fractures in this region are considered unstable humeral shaft fractures.

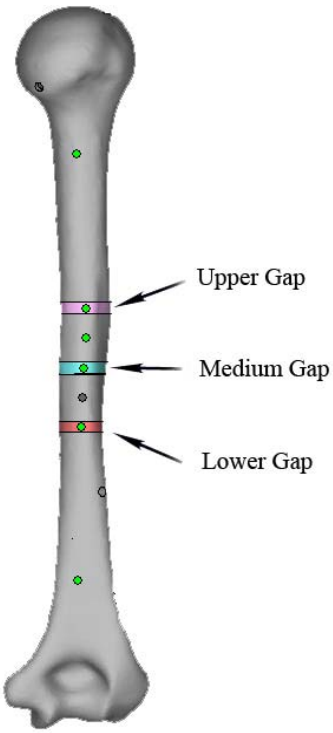

Figure 62 Three gaps in the mid-third region of the humeral shaft.

Four-node tetrahedral elements were used to build up the mesh of humeral bone in Figure 63 and the standard humeral nail with proximal and distal screws in antegrade insertion in Figure 64 and in retrograde insertion in Figure 65. In the proximal and distal screw holes on the humeral nail, smaller elements (0.6-mm) were used to investigate the stress distribution and the displacement of the implant. The humerus–implant model had a total of 79,813 nodes and 318,266 elements.

Figure 63 Finite element analysis of the humerus model.

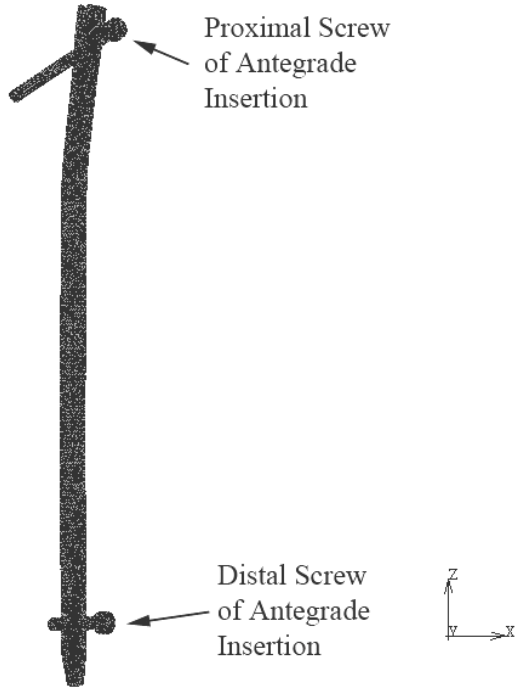

Figure 64 Finite element model of the standard humeral nail in the antegrade insertion technique.

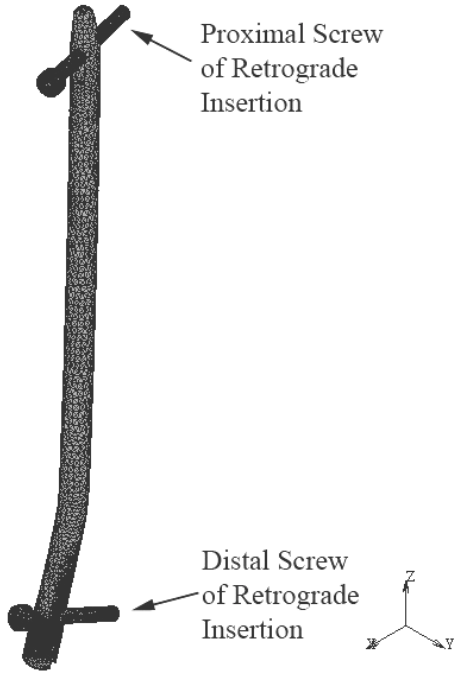

Figure 65 Finite element model of the standard humeral nail in the retrograde insertion technique.

5.2 Material Properties

Linear elastic, isotropic, and homogeneous material properties were assigned to all materials involved in the model (Duda *et al*., 2001, Sitthiseripratip *et al*., 2002). Material properties of all models are shown in Table 3. The fracture gaps were replaced by connective tissue to simulate healing status.

Table 3 Material properties applied for the FEA Model.

Model	Modulus (MPa)	Poisson's ratio
Cortical Bone	14,000	0.3
Cancellous Bone	600	0.2
Connective Tissue	3	0.4
Stainless Steel	200,000	0.3

Source: Perez *et al*. (2007).

5.3 Boundary Conditions

Muscle attachment data, force magnitudes and orientations were derived from the mechanical testing device. The weight of the lower extremity, 3 kg, was applied to the distal humerus. The glenohumeral part was made to touch the humeral head for abduction status and its displacement was fixed for all directions. As to the results of muscular force, the six forces acting on the humerus are shown in Table 10 for zero degrees abduction and in Table 11 for ninety degrees abduction.

5.4 The Finite Element Analysis

Computational simulation contact of the bone and the nail requires finite element software equipped to incrementally update nodal displacements under a load while checking for penetration between the contacting bodies. The MARC contact algorithm determines whether any two bodies are contacting each other, and

repositions nodes on the contact surface based on local normal stresses. An iterative Newton-Raphson method was used to ensure convergence to an equilibrium state at each load step. Twelve contact bodies were defined as deformable bodies. These were separated into seven parts that were cortical bones, two parts that were cancellous bone, and three parts that were implants. All cortical bone parts in contact in glue condition and were in contact to cancellous bone in glue condition too. The humeral nail was in contact to the cortical and cancellous bone in touch condition, but the proximal and distal screws were in contact in glue condition. The analyses were performed under the frictionless mode to simplify the contact phenomena.

The influence of contact conditions in the fracture zone can be classified into two stages: before bone formation and after bone formation. Sixteen analyses were performed in this study and are shown in Table 4.

Table 4 List of conditions and fracture zone in the analyses.

Cases	Insertion	Angle of Abduction	Fracture Zone
1	Antegrade	Zero Degree	Intact
2	Antegrade	Zero Degree	Upper Gap
3	Antegrade	Zero Degree	Medium Gap
4	Antegrade	Zero Degree	Lower Gap
5	Retrogrtade	Zero Degree	Intact
6	Retrogrtade	Zero Degree	Upper Gap
7	Retrogrtade	Zero Degree	Medium Gap
8	Retrogrtade	Zero Degree	Lower Gap
9	Antegrade	Ninety Degree	Intact
10	Antegrade	Ninety Degree	Upper Gap
11	Antegrade	Ninety Degree	Medium Gap
12	Antegrade	Ninety Degree	Lower Gap
13	Retrogrtade	Ninety Degree	Intact
14	Retrogrtade	Ninety Degree	Upper Gap

Table 4 Continued.

Cases	Insertion	Angle of Abduction	Fracture Zone
15	Retrogrtade	Ninety Degree	Medium Gap
16	Retrogrtade	Ninety Degree	Lower Gap

6. Design of the New Standard Humeral Nail Based on Thai Morphometric Data

6.1 Humeral bone

From previous section, the lower gap in the antegrade insertion model at ninety degrees abduction was used to validate the new humeral nail because the maximum total strain was on the lower gap. The muscular force of ninety degrees abduction from Table 11 was used to act on the humerus and all properties of the humeral model were taken from Table 3.

6.2 Nail Fixation

The proximal part was inclined 8 degrees from the shaft with the mediolateral angle of the Thai humerus as the valgus angle. The total length of nail was varied in three sizes, *viz.*, (1) the normal new humeral nail having a total length of 220 mm, (2) the long new humeral nail having a total length of 230 mm, and (3) the short new humeral nail having a total length of 220 mm. All types of new humeral nails are shown in Figure 66 and assigned the properties of titanium alloy with Young's modulus 110,000 MPa and Poisson's ratio 0.3.

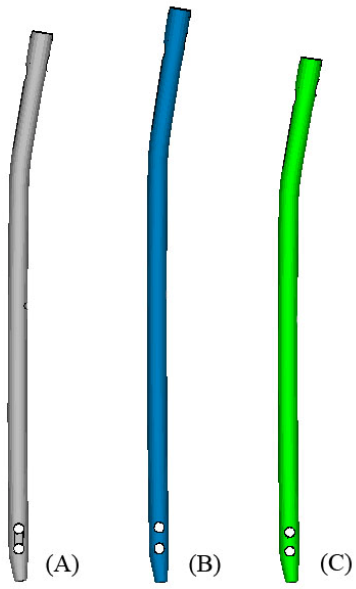

Figure 66 Three sizes of the new humeral nail: (A) The normal new humeral nail, (B) the long new humeral nail, and (C) the short new humeral nail.

RESULT AND DISCUSSION

1. Three Dimensional Morphometric Study of the Thai Proximal Humerus: Anatomical Study

1.1 Result

All parameters obtained from the three-dimensional data on the 76 Thai humeri are shown in Table 5 and are compared with data on 65 and 60 Caucasian humeri in Table 6.

Table 5 Morphometric data of the Thai humerus for each parameter (n=76).

Parameters	Mean	STDEV	Max	Min	95% Confidence Interval
1. Diameter of Humeral Head (mm)	42.65	4.21	50.60	32.00	41.70-43.60
2. Diameter of Articular Surface (mm)	40.51	3.88	47.60	31.00	39.64-41.38
3. Articular Surface Thickness (mm)	14.84	1.86	19.12	11.05	14.42-15.26
4. Inclination Angle (degree)	127.64	4.28	136.00	120.20	126.68-128.60
5. Retroversion Angle (degree:B1)	31.01	9.72	55.60	8.14	28.82-33.20
6. Retroversion Angle (degree:B2)	33.89	9.71	57.00	11.90	31.71-36.07
7. Medial Offset (mm)	5.33	2.29	11.00	0.14	4.82-5.84
8. Posterior Offset (mm)	3.37	1.98	9.10	0.30	2.91-3.83

Table 5 (Continued)

Parameters	Mean	STDEV	Max	Min	95% Confidence Interval
9. Curve Length (mm)	196.38	18.66	235.32	145.16	192.18-200.57
10. Radius of Curvature (mm)	1,344.54	461.10	2,998.87	435.81	1,240.88-1,448.21
11. Mediolateral Angle (degree)	7.83	3.50	15.01	0.80	7.05-8.62

Table 6 Morphometric data on the Thai humerus compared with three-dimensional data on the Caucasian humerus.

Parameters	Thai 3D (n=76)		Caucasian 3D based on CMM (n=65)		Caucasian 3D based on CT (n=60)	
	Mean	STDEV	Mean	STDEV	Mean	STDEV
1. Diameter of Humeral Head (mm)	42.65	4.21	46.20	5.40	46.00	2.00
2. Diameter of Articular Surface (mm)	40.51	3.88	43.30	4.30	-	-
3. Articular Surface Thickness (mm)	14.84	1.86	15.00	1.60	19.00	2.00
4. Inclination Angle (degree)	127.64	4.28	129.60	2.90	131.00	3.00
5. Retroversion Angle (degree);(B1)	31.01	9.72	17.90	13.70	19.00	6.00

Table 6 (Continued)

Parameters	Thai 3D (n=76)		Caucasian 3D based on CMM (n=65)		Caucasian 3D based on CT (n=60)	
	Mean	STDEV	Mean	STDEV	Mean	STDEV
6. Retroversion Angle (degree);(B2)	33.89	9.71	21.50	15.10	-	-
7. Medial Offset (mm)	5.33	2.29	6.90	2.00	7.00	2.00
8. Posterior Offset (mm)	3.37	1.98	2.60	1.80	2.00	2.00
9. Curve Length (mm)	196.38	18.66	-	-	-	-
10. Radius of Curvature (mm)	1,344.54	461.10	-	-	-	-
11. Mediolateral Angle (degree)	7.83	3.50	-	-	-	-

Source: Boileau and Walch (1997), and Douglas *et al*. (2000)

The results showed that most parameters of the Thai proximal humerus were smaller than those of the Caucasian; the exceptions were the retroversion angle and posterior offset. The retroversion angles of the Thai population were 31.01° and 33.89° and the posterior offset was 3.37 mm, but the retroversion angles of the Caucasian population were 17.90° and 21.50° and the posterior offset was 2.60 mm. This shows that the Thai humeral head is more inclined to the medio-posterior than the Caucasian and humeral head position tends to the posterior more than the Caucasian.

1.2 Discussion

Determination of humeral bone parameters has been investigated by several researchers with various measurement techniques. The first is direct bone measurement, in which the parameters of cadaveric humeri were measured directly (Christopher and Joseph, 1995, Michael and Albert, 1995, Frederick *et al*., 1998, Gordon, 1999, Akman *et al*., 2005, and Michael, 2005). The second technique is indirect bone measurements, which have mostly been based on two-dimensional standard radiographic images (Michael and Albert, 1996, Edward *et al*., 1997, Anthony and Robert, 1998, Laurent *et al*., 2001, Ralph *et al*., 2002, and Katsumi *et al*., 2004), magnetic resonance imaging (MRI) (Brown *et al*., 1986), and computerized tomography (CT) (Farrokh *et al*., 2001, Lieven *et al*., 2003, and Ryan *et al*., 2006). Some researchers have shown interest in three-dimensional measurements using a stylus probe that can measure and evaluate three-dimensional morphometric data of the outer geometry of the humerus or other long bones (Jennifer *et al*., 2007). The last is an advanced technique, in which long bones were measured based on three-dimensional measurements (Boileau and Walch, 1997, Douglas *et al*., 2000, Mahaisavariya *et al*., 2002, and Wataru *et al*., 2005); this gave more accuracy than other methods.

The results showed that the Thai humerus was smaller than the Caucasian; however, the use of a smaller prosthesis may lead to several undesirable consequences. The ratio of articular surface thickness to the diameter of humeral head is a relationship of marked biomechanical importance. This ratio is proportional to the surface arc of the humeral head which, extrapolating from the planar measurement of this study, correlates with the articular surface area available for the glenohumeral joint. The contact between the prosthetic head and the glenoid articular surface may decrease earlier in the range of motion. The glenoid may not be able to capture a humeral head with which it is only partially in contact, leading to instability. Contact pressures may increase for a given joint reaction force, possibly accelerating wear of the glenoid. If these pressures are at the periphery of the glenoid, eccentric loading

may promote glenoid loosening (Harryman *et al*., 1995, Michael and Albert, 1996, and Michael and Sam, 1999).

Currently, prostheses designs are based mostly on the Caucasian anatomical data. There is concern about mismatching in Thai patients. Use of a small size prosthesis in Thai patients was not suitable because of biomechanical consequences. The new design of the prosthesis based on Thai population will solve the geometric mismatching or clinical complication in Thai patients.

2. Fit and Fill Analysis of Nail Insertion in the Thai Humerus: A Virtual Simulation Study

2.1 Result

All parameters of geometric mismatch in the cases of antegrade and retrograde insertion are shown in Tables 7 and 8, respectively.

Table 7 Parameters of geometric mismatch in the antegrade insertion technique.

Geometric mismatch parameters	Average	Standard Deviation(SD)
The diameter of the medullary canal	7.85-13.78 mm.	1.29-3.47
The minimal reaming diameter	8.84-14.83 mm.	0.60-2.80
The minimal inner cortical reaming thickness	0.06-1.45 mm.	0.22-2.00
The percentage of the removed cortical bone area	3.81-107.14 %	15.50-162.60
The deviation of the nail center from center of the medullary canal.	0.42-3.42 mm.	0.24-1.40

Table 8 Parameters of geometric mismatch in the retrograde insertion technique.

Geometric mismatch parameters	Average	Standard Deviation(SD)
The diameter of the medullary canal	7.85-13.78 mm.	1.29-3.47
The minimal reaming diameter	8.77-15.15 mm.	0.44-8.25
The minimal inner cortical reaming thickness	0.06-4.10 mm.	0.21-3.22
The percentage of the removed cortical bone area	3.79-394.12 %	15.15-593.23
The deviation of the nail center from center of the medullary canal.	0.38-4.72 mm.	0.22-3.08

Virtual insertion revealed that some regions of the standard humeral nail deviated out of the medullary canal. This would cause some clinical complications.

2.2 Discussion

Stable internal fixation of upper arm fractures is growing in popularity (Van de Griend *et al*., 1986). External fixation is restricted to fractures with severe soft tissue damage and contaminated or defect fractures. The well-known advantages of plate osteosynthesis are high stability and the possibility of postoperative mobilization without dressing, but the disadvantages are the traumatizing approach and iatrogenic radial nerve palsy (Fernandez *et al*., 2003). The advantages of the humeral nail are that they cause minor soft tissue trauma, require short operating time, do not require stripping of the bone and provide indirect fracture stabilization when the fracture level of humerus occurs, as it frequently does as shown in Figure 67, in the middle-third region of the humerus.

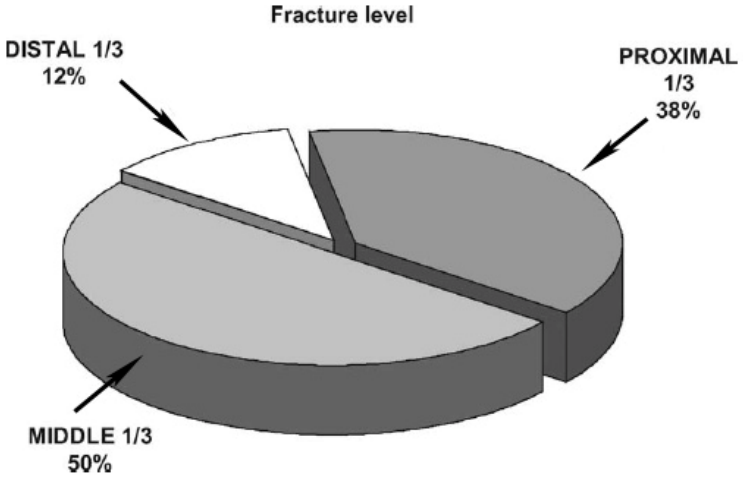

Figure 67 Fracture level in percentages.
Source: Seide *et al*. (2007).

Based on the results in Tables 7 and 8 and the region of humerus fracture, we considered the minimal reaming diameter at the mid-shaft region of the humerus because this parameter affects the thickness of the cortex. Our study revealed that the retrograde technique required a smaller reaming diameter than the antegrade technique, as shown in Figure 68.

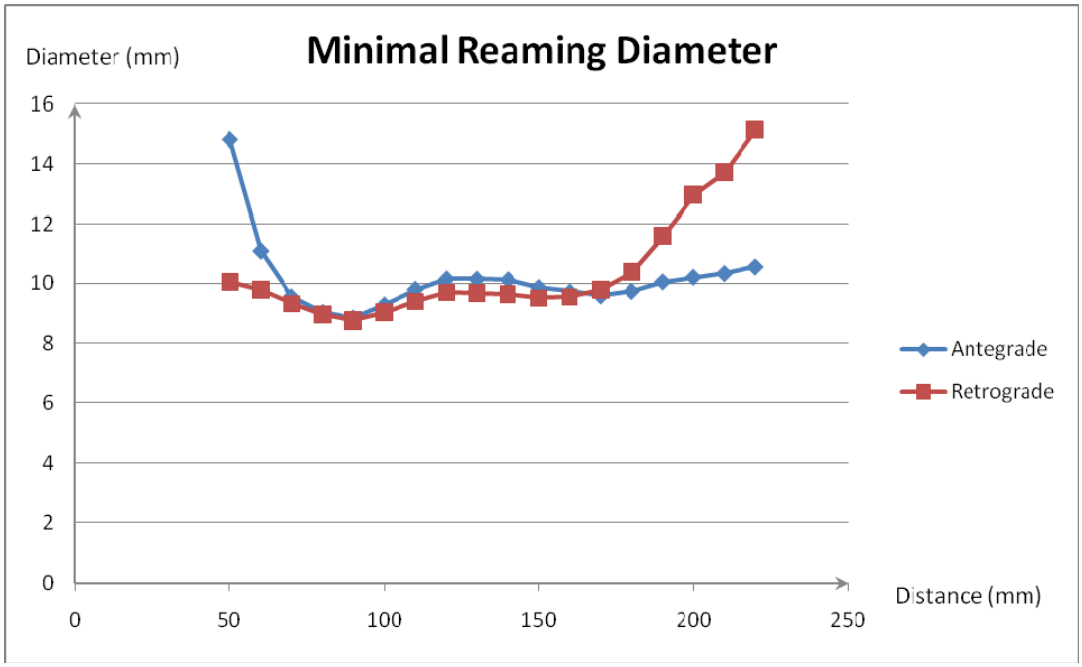

Figure 68 Graph of minimal reaming diameter with antegrade versus retrograde insertion.

On the basis of physical considerations, the retrograde technique is better than the antegrade technique because the over-reaming of the humeral canal weakens the shaft and may lead to bursting in the future; however, these biomechanical considerations must be verified.

3. The Advanced Method to Evaluate the Three-dimensional Shape and Direction of the Rotator Cuff and Deltoid Muscles: MRI 3 Tesla

3.1 Result

From the muscle axes, the delta value of the start point and the end point were used to find the unit vector of each muscle. The data are shown in Table 9.

Table 9 Unit vectors of the rotator cuff and deltoid muscles.

Muscle	$\vec{i}$	$\vec{j}$	$\vec{k}$
1. Anterior Deltoid	-0.2961	-0.1408	0.9447
2. Lateral Deltoid	0.0817	0.1009	0.9915
3. Posterior Deltoid	-0.0226	-0.5454	0.8379
4. Infraspinatus	-0.6656	-0.7284	-0.1627
5. Subscapularis	-0.6402	-0.7349	-0.2237
6. Supraspinatus	-0.6326	-0.7619	0.1386

This unit vector was oriented in the direction of muscle that acts on the humerus at zero degrees normal abduction. The deltoid muscle is large in size and can be separated into three parts: the anterior deltoid, the lateral deltoid, and the posterior deltoid; these acts on the mid shaft region.

3.2 Discussion

It has long been recognized that, any estimate of muscular force in the stability of shoulder joint would depend on the biomechanical model chosen. In the classical method, electromyography (EMG) is used to evaluate the muscle force, but EMG recordings fail to produce reliable force estimates because the relationship between force and EMG activity is dependent on several unpredictable variables (Inman *et al*., 1952, De Lucas and Forrest, 1973, Van der Helm, 1994, and MacMahon *et al*., 1995) Several researchers have used the physiological cross-sectional area (PCSA) of a muscle (Wood *et al*., 1989, and Murray *et al*., 2000), but in this method, the muscle was measured in two dimensions. The shoulder mechanism is a three-dimensional kinematics model, which is active in three directions. This study evaluated the direction of the muscles on three axes and employed a mechanical testing device to find the force magnitude. The data can be used to test the finite element analysis of humeral implant.

4. Measuring Muscle Force Exerted on the Thai Humerus by the Rotator Cuff and Deltoid Muscles

4.1 Result

The force magnitudes of the rotator cuff and the three parts of the deltoid muscle at the zero degrees abduction position are given in Table 10 and those at the ninety degrees abduction position in Table 11. Figure 69 shows the muscular force acting on the humerus at zero degrees abduction and Figure 70 the force at ninety degrees abduction.

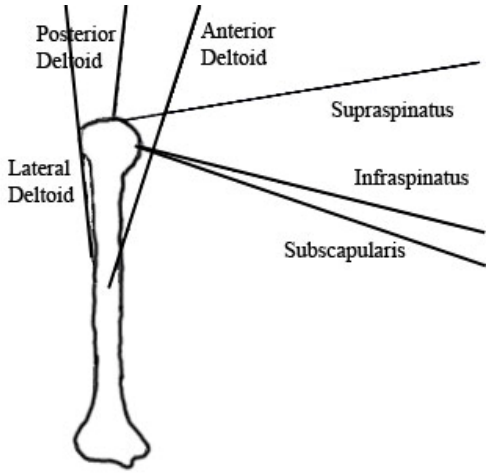

Figure 69 The right Thai humerus at zero degrees abduction with the rotator and deltoid muscles.

Table 10 Force magnitudes of six muscles at zero degrees abduction.

Muscle	Force Magnitude (N)	F_X (N)	F_Y (N)	F_Z (N)
Anterior Deltoid	78.00	-23.09	-10.98	73.69
Lateral Deltoid	25.33	2.07	2.56	25.12
Posterior Deltoid	22.00	-0.50	-12.00	18.43
Subscapularis	22.00	-14.09	-16.17	-4.92
Infraspinatus	58.33	-38.82	-42.49	-9.49
Supraspinatus	206.67	-130.75	-157.47	28.65

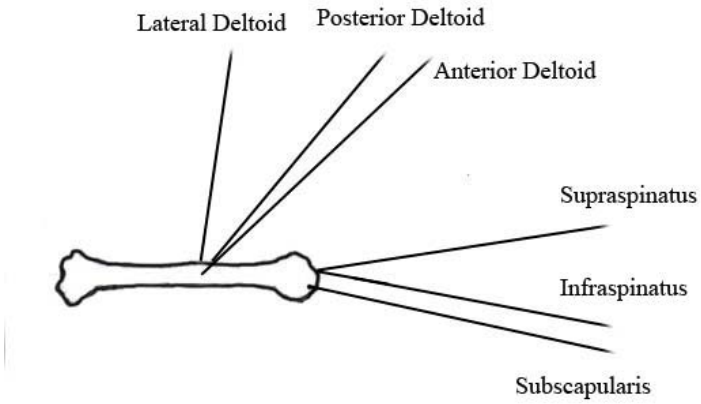

Figure 70 The right Thai humerus at ninety degrees abduction with the rotator cuff and deltoid muscles.

Table 11 Force magnitudes of six muscles at ninety degrees abduction.

Muscle	Force Magnitude (N)	F_X (N)	F_Y (N)	F_Z (N)
Anterior Deltoid	49.33	-31.33	3.66	37.93
Lateral Deltoid	38.00	-5.40	-2.28	37.54
Posterior Deltoid	10.67	-7.02	-4.59	6.59
Subscapularis	76.67	-74.56	-7.79	-16.05
Infraspinatus	31.67	-31.09	-2.07	-5.66
Supraspinatus	66.00	-64.62	-9.20	9.81

The constant weight of the arm was active at the distal humerus, and the effect of this was to tighten all of the slings. The results show the magnitudes of the force for each axis that act on the humerus as muscular force at normal and severe abduction.

4.2 Discussion

The glenohumeral joint is not inherently stable because the humerus hangs by muscular force. The cadaveric testing models limited the muscular forces on the humerus because the cadaveric model was given only force magnitudes, not direction. The computer control was used to pull the sling connected to the model, but the force magnitude was found from simulated active abduction trials (Poppen and Walker, 1978). The models were elevation (Inman *et al*., 1944) and abduction (Wuelker *et al*., 1993, Debski *et al*., 1995, McMahon *et al*., 1995, Apreleva *et al*., 2000, Halder *et al*., 2000, Kedgley *et al*., 2007, Levasseur *et al*., 2007, Terrier *et al*., 2007, and Warner *et al*., 2007) brought about by pulling muscle attached to the model.

This model was measured the real force magnitude that act on the humerus with three-dimensional direction and does not account for rotation of the scapular during abduction of the upper extremity. The infraspinatus and subscapularis were

used to counteract the rotation. At zero degrees abduction, the supraspinatus was active as the maximum value from the result of the absolute equilibrium. The weight of the arm is the main cause of moment occurring. The area of contact between the humeral head and the glenohumeral was a fulcrum of the system. The distance between supraspinatus and the fulcrum was less than the distances between the other muscles and the fulcrum; it had a maximum force for equilibrium in the rotating of the system. At ninety degrees abduction, the maximum of muscular force occurred at the supraspinatus the same as at zero degrees abduction, but the force distributed to each sling was higher than at zero degrees abduction as the severe load was shared to all slings and the force transferred to the humerus. At the two states of abduction, zero and ninety degrees, it was found that magnitudes of the forces of the lateral deltoid and subscapularis increased and the magnitude of the force of the supraspinatus decreased to a minimum. In the future, the dynamics of each sling in the humeral testing system will have to designed to make it possible to find the force magnitude at any degree abduction.

5. Finite Element Analysis of the Thai Humerus at Zero and Ninety Degrees Abduction

5.1 Result

The maximum von Mises stress on the implants, i.e., the standard humeral nail, proximal screw, and distal screw, are shown in Tables 12 and 13. All implants were strongly enough for use to fix the humeral shaft fracture in both the antegrade and the retrograde insertion techniques. All figures of FEA are shown in Appendix Figure 1-24 and the stress distributions at the medial and lateral side on standard humeral nail are shown in Appendix Figure 29-44.

Table 12 The maximum von Mises stress on the implant with the antegrade insertion technique.

Zero Degree Abduction	Gap position	Stress (Mpa)
Proximal Screw Hole	Lower Gap	784.00
Distal Screw Hole	Medium Gap	574.13
Proximal Screw	Lower Gap	115.65
Distal Screw	Medium Gap	96.02

Ninety Degree Abduction	Gap position	Stress (Mpa)
Proximal Screw Hole	Lower Gap	348.70
Distal Screw Hole	Lower Gap	145.26
Proximal Screw	Upper Gap	149.22
Distal Screw	Lower Gap	123.83

Table 13 The maximum von Mises stress on the implant with the retrograde insertion technique.

Zero Degree Abduction	Gap position	Stress (Mpa)
Proximal Screw Hole	Medium Gap	247.60
Distal Screw Hole	Lower Gap	599.65
Proximal Screw	Medium Gap	729.45
Distal Screw	Lower Gap	301.50

Ninety Degree Abduction	Gap position	Stress (Mpa)
Proximal Screw Hole	Upper Gap	319.63
Distal Screw Hole	Upper Gap	218.99
Proximal Screw	Upper Gap	460.86
Distal Screw	Upper Gap	118.56

5.1.1 Zero Degree Abduction

Study of the total strain on the gaps showed that the upper gap had higher strain than the others in the case of antegrade insertion, as shown in Figure 71; the total strain at the upper gap was between 3,415-107,007 microstrain. In retrograde insertion, the maximum total strain was at the medium gap, as shown in Figure 72; the total strain was between 12,734-29,431 microstrain.

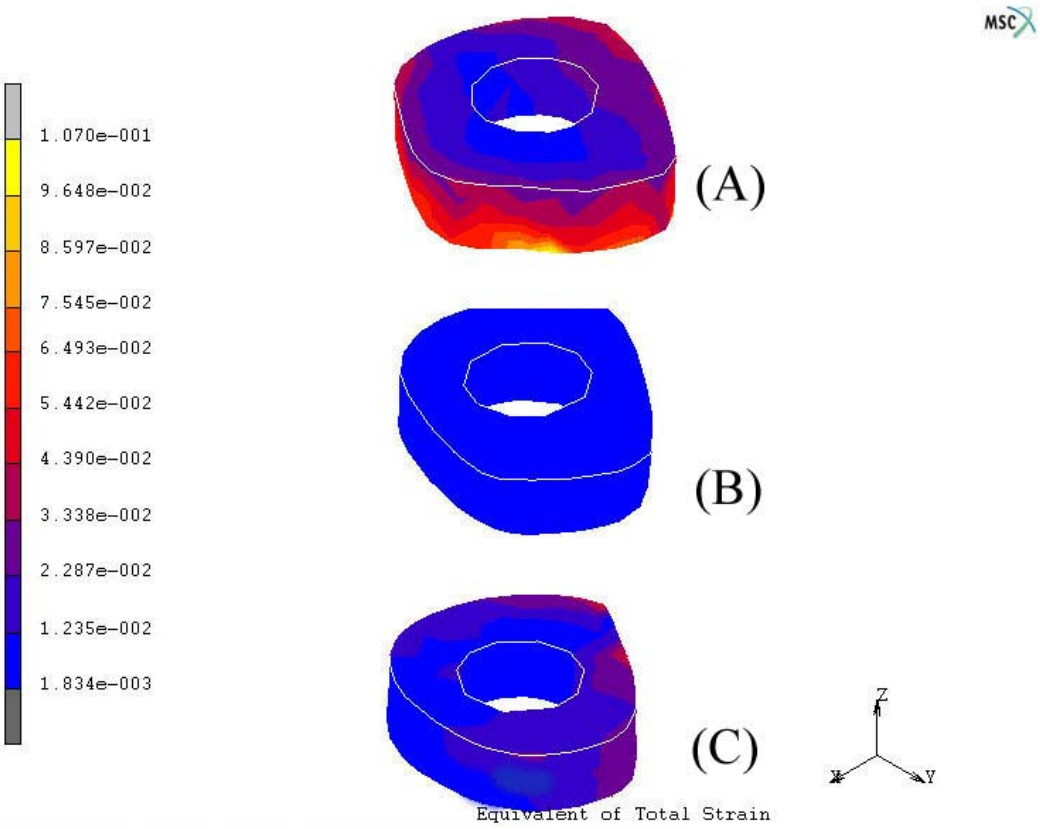

Figure 71 The total strain on the three gaps with antegrade insertion and zero degrees abduction: (A) Upper gap, (B) Medium gap, and (C) Lower gap.

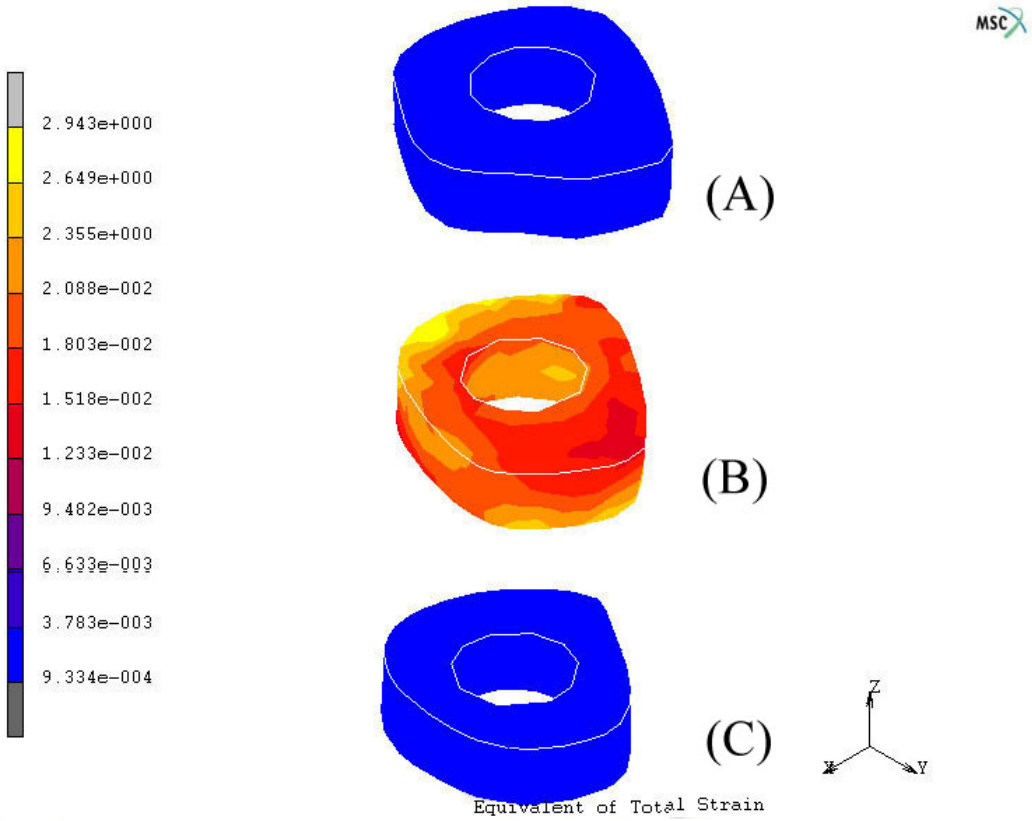

Figure 72 The total strain on the three gaps with retrograde insertion and zero degrees abduction: (A) Upper gap, (B) Medium gap, and (C) Lower gap.

5.1.2 Ninety degree abduction

This status is a severe condition for normal abduction. Study of the total strain on the gaps showed that the lower gap had the highest total strain in the cases of both antegrade and retrograde insertion. In antegrade insertion, the maximum strain was at the lower gap and was between 15,422-57,727 microstrain, as shown in Figure 73. In retrograde insertion, the maximum strain was at the lower gap the same as in antegrade insertion; the total strain was between 4,190-73,681 microstrain, as shown in Figure 74.

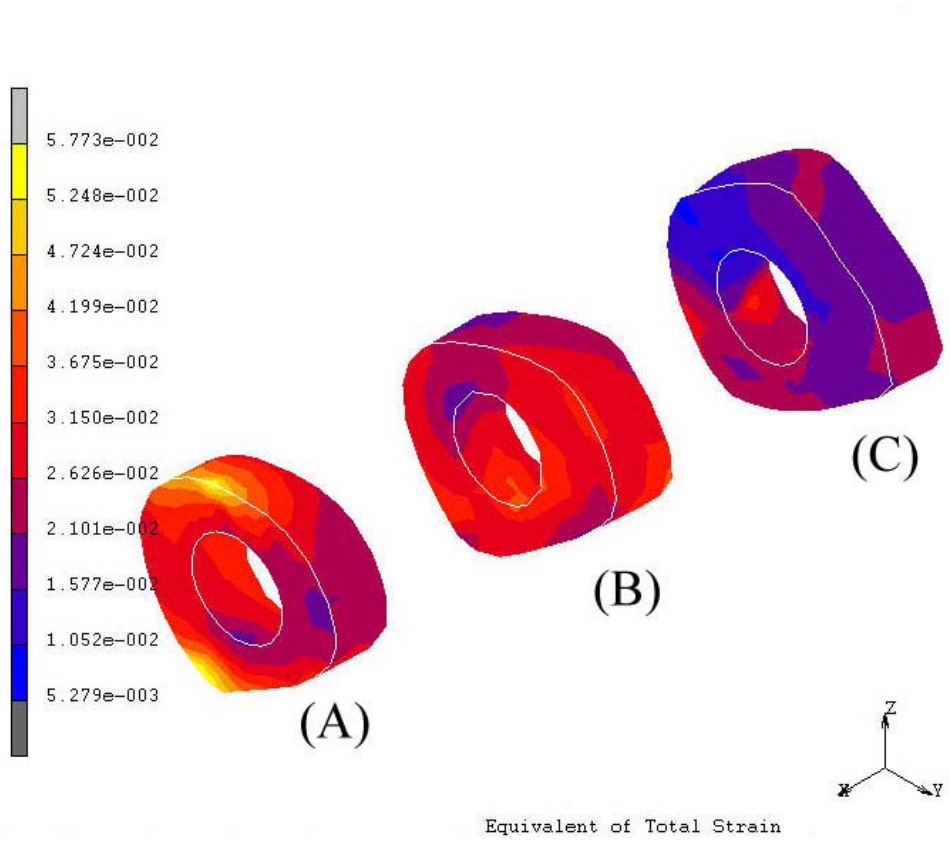

Figure 73 The total strain on the three gaps with antegrade insertion and ninety degrees abduction: (A) Lower gap, (B) Middle gap, and (C) Upper gap.

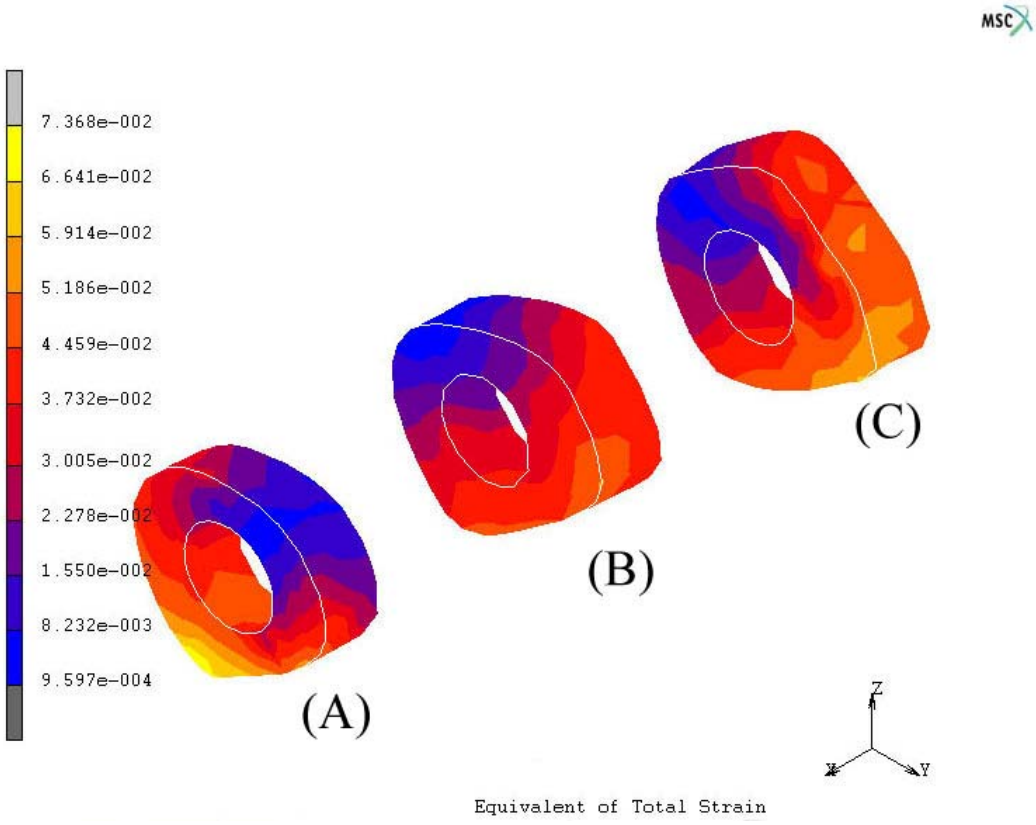

Figure 74 The total strain on the three gaps with retrograde insertion and ninety degrees abduction: (A) Lower gap, (B) Middle gap, and (C) Upper gap.

5.2 Discussion

The muscle load configuration was applied for biomechanical study of a humeral shaft fracture with standard humeral nail fixation. The results will be discussed for the nail and the bone, respectively.

5.2.1 The standard humeral nail

The stress distribution on humeral nail at zero degree abduction was higher than ninety degree status. The humeral nail had shared load from the humeral bone but the ninety degree abduction, humeral bone received much load and

nail had shared a little. It made the higher strain on the fracture gap at ninety degree abduction.

5.2.2 Humeral bone

The maximum strain arose on the lower gap at zero and ninety degrees abduction. The cause was the muscular force moment. The lower gap was at the maximum distance from the six muscular forces, and when the forces had a constant value, the moments vary with the distance. The strain distribution on the bone is the main factor affecting bone remodeling. Figure 75 is a graphic illustration showing the four mechanical usages windows of Frost's mechanostat theory.

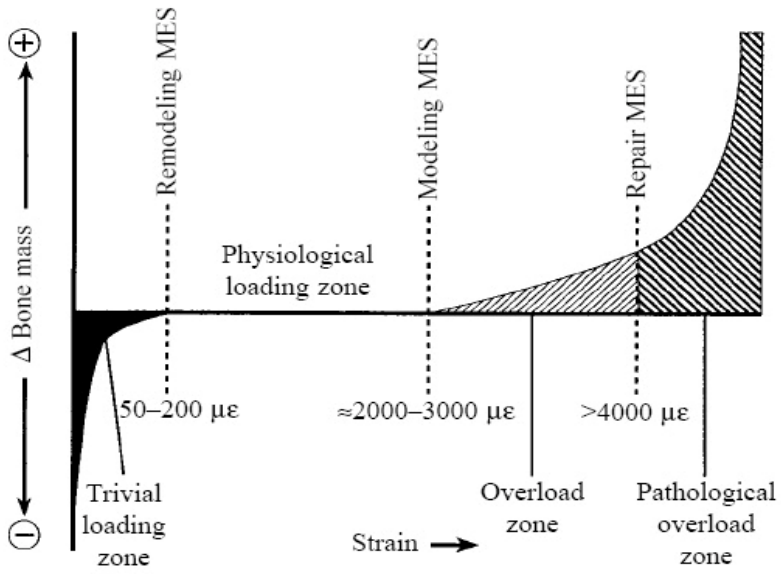

Figure 75 Graph of Frost's mechanostat theory show the behavior of strain distribution on bone.

Source: Su *et al*. (1999).

Each loading zone is defined by strain magnitude thresholds (horizontal axis) which predict bone remodeling and/or modeling activities resulting in an increase or decrease in bone mass (Δ bone mass, vertical axis). Below the remodeling minimum effective strain (MES, or trivial loading zone), strains are low

and bone remodeling is activated to decrease bone mass. Thus, the MES is analogous to the 'lazy' zone (Carter *et al*., 1996) and the 'dead' zone (Huiskes *et al*., 1992). Above the remodeling MES but below the modeling MES (the physiological loading zone), remodeling activity is relatively repressed and there is no net change in bone mass. At higher strains just above the modeling MES, lamellar bone is formed, causing an increase in bone mass. When strains are greater than the repair MES (pathological overload zone), new woven bone is added to bone surfaces and probably represents a repair reaction.

All gaps in both cases of normal abduction had strain greater than the pathological overload zone. The maximum strain distribution on each gap at zero degrees abduction depended on the load acting on the distal humerus. If the load at the distal bone increased, it raised the maximum strain on each gap. In the case of ninety degrees abduction, the maximum strain was at the lower gap because of the moment of muscular forces act on the gap. The distance from all muscular forces to the lower gap was higher than the distances to the other gaps, and this directly affected the moment that occurred. In the case of a humeral shaft fracture, the patient's arm hung in a sling; the patient did not lift the humeral bone to ninety degrees abduction.

5.2.3 Mechanical validation

A mechanical testing device was used to validate the finite element model at zero degrees abduction with three strain gages on the humeral bone model. The first was glued at the top of humeral head as shown in Figure 76 (A). The others were glued on the shaft of humeral model as shown in Figure 76 (B). All strain gages were used to measure the total strain that occurred on the humeral bone.

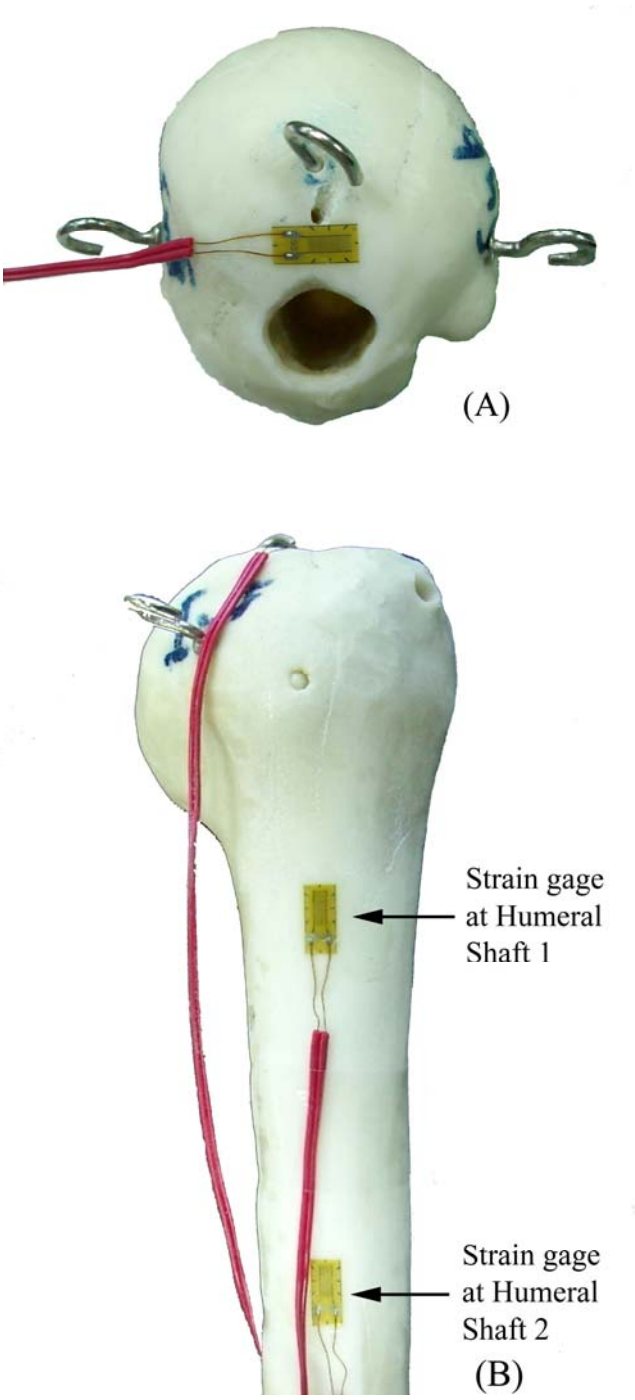

Figure 76 Strain gages on the humeral model: (A) Strain gage on the humeral head, (B) Strain gage on the shaft of the humeral bone model.

Zero degrees abduction with the intact condition was used to validate the FEA data and Mechanical Testing Device. The strain gages as shown in Figure 77 collected the data in mV/V unit and translated them to ε:

$$\varepsilon = \left(\frac{(mV/V)*0.001}{2.07} \right)$$

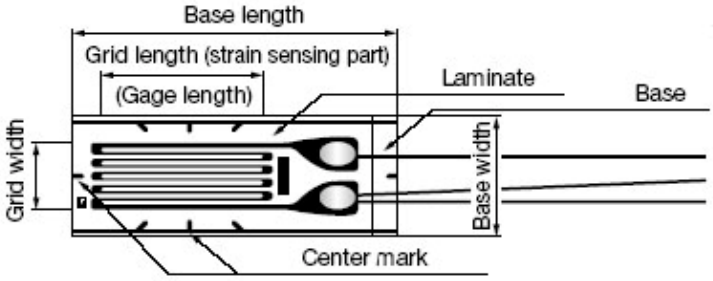

Figure 77 The diagram of strain gage.

The data from the mechanical testing device as shown in Figure 78 was used to find the total strain that occurred on the humeral bone model at three distances from the top of the humeral head and are shown in Table 14:

Figure 78 Mechanical testing device in zero degrees abduction status.

Table 14 The mechanical testing device data from the humeral bone model.

Strain gage position	Strain
	0.00072
Top of Humeral bone model	
Humeral shaft 1	0.00025
Humeral shaft 2	0.00030

The finite element model used the properties of sponge resin as cancellous bone and dense resin as cortical bone. The cancellous bone has Young's modulus 713 MPa and cortical bone has Young's modulus 911 MPa and Poisson's ratio 0.3. All properties of resin were obtained from mechanical testing with a tensile testing machine. The total strain on the humeral model from finite element analysis compared with that from the mechanical testing device is shown in Figures 79 and 80.

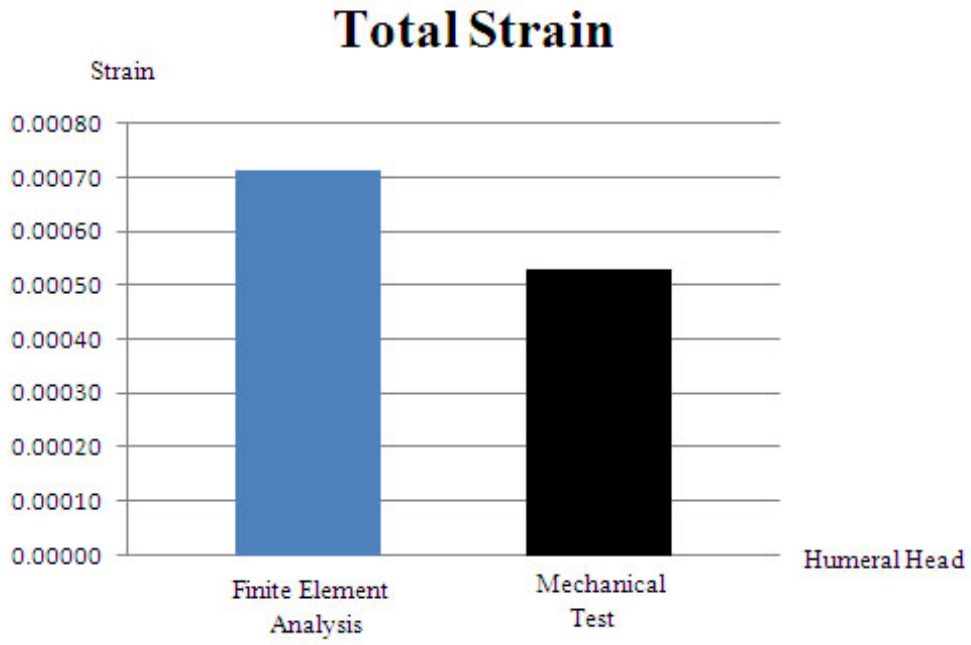

Figure 79 A comparison of FEA and Mechanical Testing data on the total strain at the humeral head.

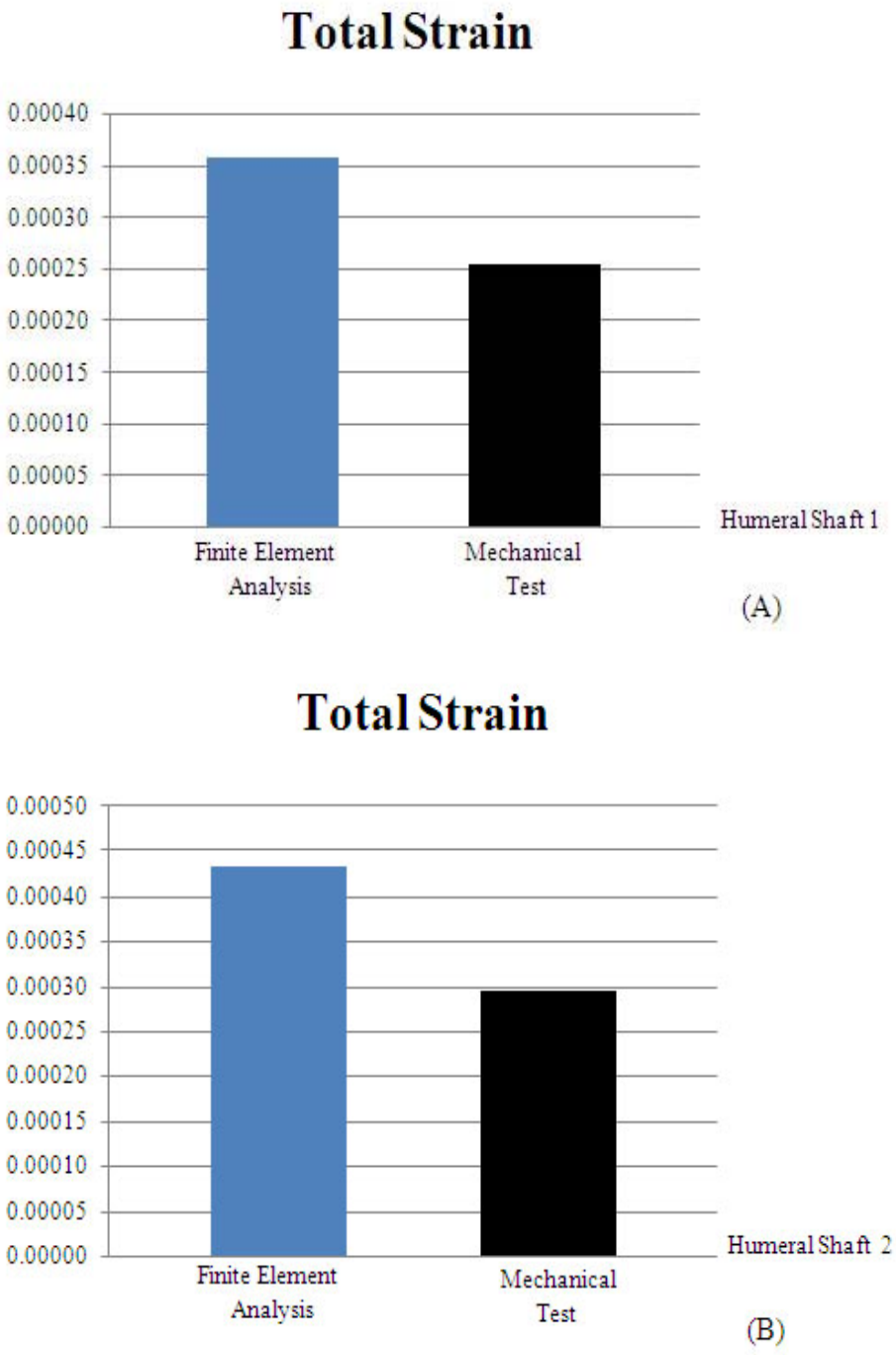

Figure 80 A comparison of FEA and Mechanical Testing data on the total strain on at the humeral shaft: (A) Humeral shaft 1, (B) Humeral shaft 2.

The total strain from the mechanical testing device was lower than that from FEA at three levels attached to the strain gages. The mechanical testing model was not really homogeneous and isotropic, and this may be the main reasons that the error occurred. Another reason may be due to the fact that the contact area of the model and the strain gage was not really a flat area, and this affected the strain distribution on the strain gage. The result was an error of approximately 25.96 % at the humeral head, 28.70 % at the humeral shaft 1, and 31.55 % at the humeral shaft 2 from the FEA data. Related research has used a photoelastic method to determine the stress distribution on an implant and bone, and this can reduce the error between mechanical testing data and FEA data; however in this study, we were constrained by limited financial support.

6. Design of the New Standard Humeral Nail Based on Thai Morphometric Data

6.1 Result

The total strain on the lower gap that was fixed with three sizes of the new humeral nail was compared with that on the standard humeral nail in Table 15 and is shown in Figure 81.

Table 15 Total strain at the lower gap at ninety degrees abduction in four nails.

Type of Nail	Range of Strain (microstrain)
Standard Nail	15,422-57,727
Normal New Nail	2,873-39,050
Long New Nail	2,547-32,954
Short New Nail	7,223-43,696

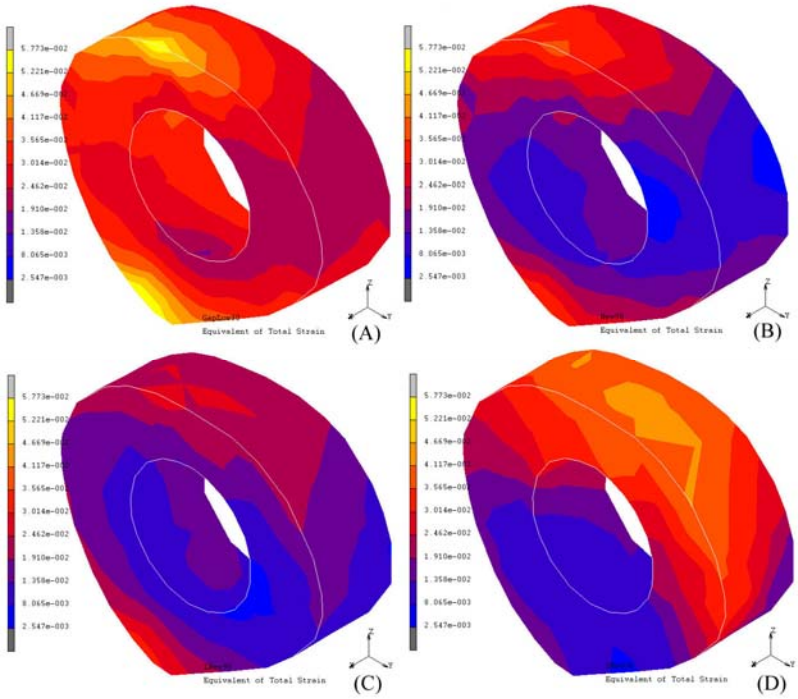

Figure 81 Total strain on lower gaps fixed with four types of nail: (A) the standard humeral nail, (B) the normal new humeral nail, (C) the long new humeral nail, and (D) the short humeral nail.

The long new humeral nail fixed the fracture at the lower gap with greater stability than the other nails. Because the distal screw will be far away from the gap, the stability will increase.

6.2 Discussion

The material to construct the nail was changed from stainless steel to titanium alloy, compared in Table 16. Titanium is ductile and well yield to the mechanical shaping. Titanium has the most biocompatibility of all metals due to its resistance to attack by body fluids, high strength and low modulus and is widely used for implants, surgical devices, pacemaker cases and centrifuges. The most common grades used are commercially pure titanium and the Ti6Al4V alloy (Altieri *et al*., 2003).

Table 16 Comparison between titanium and stainless steel.

Characteristics	Stainless Steel	Titanium
Stiffness	High	Low
Strength	Medium	High
Corrosion resistance	Low	High
Biocompatibility	Low	High

Source: Altieri *et al*. (2003).

The new humeral nail was used to fix the lower gap of humerus fracture with severe condition. It can reduce the total strain at the lower gap 84.40 % at lower range and 32.35 % at upper range from the standard humeral nail. In case of long new humeral nail, it can reduce the total strain 86.17 % at lower range and 42.91 % at upper range and 60.79 % at lower range and 24.31 % at upper range of short new humeral nail. From the result, the long new humeral nail was shown the higher stability than another nail but it want more reaming canal that will make some thin cortex area at the distal bone for crack at the distal part.

CONCLUSION AND RECOMMENDATION FOR FURTHER RESEARCH

1. Conclusion

The medical imaging processing, computerized tomography, and magnetic resonance imaging 3 tesla was used to find the morphometric data of Thai humerus, the outer and inner geometry with more accuracy than the other methods, and direction of rotator cuff and deltoid muscles which is the main effect of normal abduction. The rapid prototyping was used to construct the Thai humeral bone model for mechanical testing device to find the muscular force and validate the result with FEA.

We applied FEA to analyze the humeral bone with intramedullary fixation. The humerus differs from the femur and tibia, in which the body weight is the main factor creating the initial load acting on the proximal bone. In a humeral shaft fracture, the patient's arm will hang in zero degrees abduction, and the ninety degrees abduction will not occur.

Finally, the proper design of the new humeral nail with better mechanical performance can be summarized as follows:

1.1 Nail (Titanium alloy): total length 220 mm, proximal diameter 9 mm, proximal screw hole 4 mm, proximal length 55 mm, distal diameter 8 mm, distal screw hole 4 mm, neck shaft angle 55°, valgus angle 8°, location of proximal screw hole from the proximal end of the nail 13.5 mm, location of lower distal screw hole from the distal end of the nail 13 mm, the distance between upper and lower distal screw hole 8 mm as shown in Figure 82 and 83.

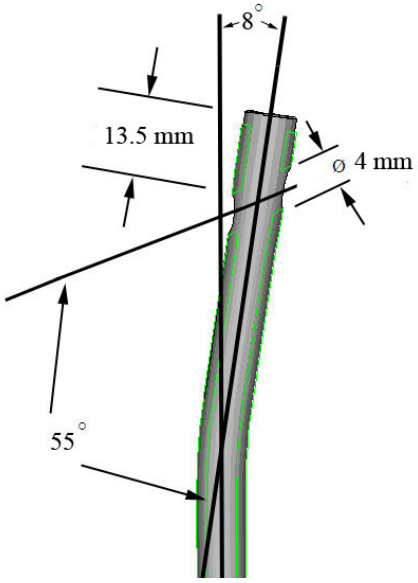

Figure 82 Dimensions of new humeral nail.

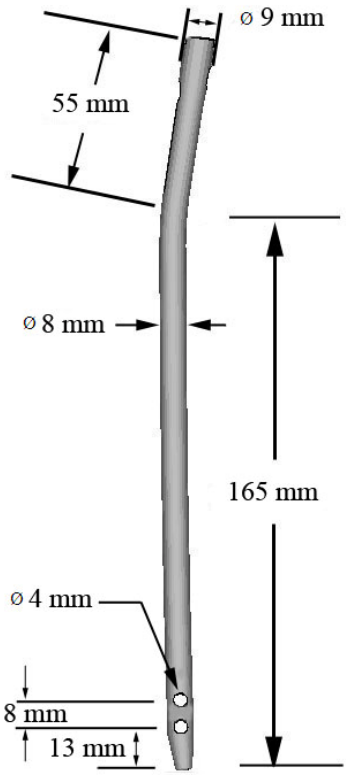

Figure 83 Dimensions of new humeral nail 2.

1.2 Proximal screw: total length 58 mm, diameter 4 mm.

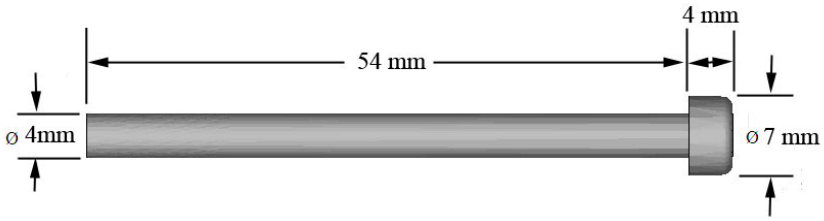

Figure 84 Dimensions of proximal screw.

1.3 Distal screw: total length 24 mm, diameter 4mm.

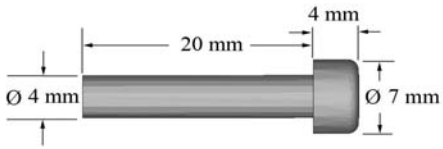

Figure 85 Dimensions of distal screw.

2. Recommendation for Further Research

The research work done in this study was not finished due to some limitations. It can be extended into several steps. The first would be to find the three dimensional shape of the muscles at several angles of abduction, such as 30°, 45°, and 60°. The three-dimensional shape can be used to find the unit vectors of muscular forces for use in Mechanical Testing and Finite Element Analysis.

Secondly the accuracy of the results calculated by the finite element method need to be verified with servo-hydraulic mechanical testing. Moreover, fatigue analysis is the next important issue to verify the service lifetime of the humeral nail under dynamic loading.

Thirdly, the prototyping and manufacturing of the humeral nail is an important issue. Optimization of cutting conditions in turning is indeed important to obtain high-

quality, smooth surface finishing. The higher the quality of surface finishing, the better the corrosion resistance of the implant in living bone tissue will be. This directly affects to the quality of the passive film of the implant, for the implant made of stainless steel and titanium alloy will spontaneously form a chemically inactive surface when exposed to air or other oxygen-containing environments.

Fourthly, after finalizing the geometrical, biomechanical and manufacturing aspects of the humeral nail development, it is necessary to pay attention to the clinical aspect of the implant to the living bone tissue. Thus, the ***in vivo*** testing should be performed to confirm the biocompatibility aspects before stepping forward to clinical trials.

Finally, clinical follow up is needed for the final evaluation and further development of the humeral nail.

LITERATURE CITED

Akman, S.D., P. Karakas and M.G. Bozkir. 2005. The morphometric measurements of humerus segments. **Turk J. Med Sci**: 81-85.

Akpinar, F., A. Aydinlioglu, N. Tosun, T. Dogan, I. Tuncay and O. Unal. 2003. A morphometric study on the humerus for intramedullary fixation. **J. Exp Med**: 35-42.

Altieri, C., J. Flores, V. Gonzalez and A. Rodriguez. 2003. Biomechanics of orthopaedic fixations. **Mechanics of Materials I.** University of Puerto Rico.

Anthony, J.D. and T.B. Robert. 1998. Comparison of humeral head retroversion with the humeral axis/biceps groove relationship: A study in live subjects and cadavers. **J. Shoulder Elbow Surg**: 453-457.

Apreleva, M., I.M. Parsons IV, J.J.P. Warner, F.H. Fu and S.L-Y. Woo. 2000. Experimental investigation of reaction forces at the glenohumeral joint during active abduction. **J. Shoulder Elbow Surg**: 409-417.

Bajaj, S.K., N.R. Mohan and C.S. Kumar. 2003. Supracondylar femoral nail in the management of non-union of humeral shaft fractures. **J. Care Injuried**: 1-5.

Bathe, K.J. 1996. **Finite Element Procedures.** Prentice-Hall, Inc., New Jersey.

Bishop, R.C., K.A. Moore and M.N. Hadley. 1996. Anterior cervical interbody fusion using autogeneic and allogeneic bone graft substrate: a prospective comparative analysis. **J. Neurosurg**: 206–210.

Bitsakos, C., J. Kerner, I. Fisher and A.A. Amis. 2004. The effect of muscle loading on the simulation of bone remodeling in the proximal femur. **J. Biomech**: 1-7.

Blum, J., H. Janzing, R. Gahr, H.S. Langendorff and P.M. Rommens. 2000. Clinical performance of a new medullary humeral nail: Antegrade versus retrograde insertion. **J. Ortho Trauma**: 342-349.

Blumenthal, S.L., J. Baker and A. Dossett. 1988. The role of anterior lumbar fusion for internal disc disruption. **Spine**: 566–569.

Boileau, P. and G. Walch. 1997. The three-dimensional geometry of the proximal humerus. **J. Bone Joint Surg**: 857-865.

Boriani, S., R. Regnoli and M. Giocomelli. 1991. Results of the multicentric Italian experience on the Gamma nail: A report on 648 cases. **Orthopaedics**: 1307-1314.

Braunstein, V., E. Wiedemann, W. Plitz, O.J. Muensterer, W. Mutschler and S. Hinterwimmer. 2007. Operative treatment of greater tuberosity fractures of the humerus-A biomechanical analysis. **J. Clinbiomech**: 1-6.

Brown, C.W., T.J. Orme and H.D. Richardson. 1986. The rate of pseudarthrosis (surgical nonunion) in patients who are smokers and patients who are nonsmokers: a comparison study. **Spine**: 942–943.

Browner, B.D., J.B. Jupiter, A.M. Levine and P.G. Trafton. 1998. **Skeleton Trauma: Fractures, Dislocations, Ligamentous Injuries.** 2nd ed. W.B. Saunders Company, United State of America.

Buchler, P., N.A. Ramaniraka, L.R. Rakotomanana, J.P. Iannotti and A. Farron. 2002. A finite element model of the shoulder: application to the comparison of normal and osteoarthritic joints. **J. Clinbiomech**: 630-639.

Burchardt, H. and W.F. Enneking. 1978. Transplantation of bone. **Surg Clin North Am**: 403–427.

Carter, D.R., M.C.H. Van der Meulen and G.S. Beaupre. 1996. Mechanical factors in bone growth and development. **Bone**: 5S-10S.

Chao, E.Y., N. Inoue, J.J. Elias and H. Aro. 1998. Enhancement of fracture healing by mechanical and surgical intervention. **Clin Orthop**: 163-178.

Christopher, M.J. and P.I. Joseph. 1995. Limits imposed on glenohumeral motion by joint geometry. **J. Shoulder Elbow Surg**: 281-285.

Christos, G. 2005. Humeral nails: when to choose what and how to use. **J. Cuor**: 294-304.

Claes, L.E. and C.A. Heigele. 1998. Magnitudes of local stress and strain along bony surfaces prsdict the course and type of fracture healing. **J. Biomech**: 255-266.

Cross, A.R. and D.D. Lewis. Fracture management, bone healing and grafting. College of Veterinary Medicine, University of Florida.

Daftari, T.K., T.E. Jr Whitesides and J.G. Heller. 1994. Nicotine on the revascularization of bone graft. An experimental study in rabbits. **Spine**: 904–911.

Daniel, G., P. Jean-Marie, Z. Sebastien and V.D. Stephane. 2003. Shoulder surgery from cuff repair to joint replacement: An update. **J. Joint Bone Spine**: 422-432.

Debski, R.E., P.J. McMahon, W.O. Thompson, S.L-Y. Woo, J.J.P. Warner and F.H. Fu. 1995. A new dynamic testing apparatus to study glenohumeral joint motion. **J. Biomechanics**: 869-874.

Deluca, C.J. and W.J. Forrest. 1973. Force analysis of individual muscles acting simultaneously on the shoulder joint during isometric abduction. **J. Biomechanics**: 385-393.

De Lucas, C.J. and W.J. Forrest. 1973. Force analysis of individual muscles acting simultaneously on the shoulder joint during isometric abduction. **J. Biomech**: 385-393.

DePalma, A.F., R.H. Rothman and G.E. Lewinnek. 1972. Anterior interbody fusion for severe cervical disc degeneration. **Surg Gynecol Obstet**: 755–758.

Dimakopoulos, P., X.A. Papadipoulos, M. Papas, A. Panagopoulos and E. Lambiris. 2005. Modified extra rotator-cuff entry point in antegrade humeral nailing. **J. Arch Ortho Trauma Surg**: 27-32.

Doody, S.G., L. Freedman and J.C. Waterland. 1970. Shoulder movements during abduction in the scapular plane. **Arch. Phys. Med. Rehabil**: 595.

Douglas, D.R., Y. Jie, U.B. Louis, L.F. Evan and Y. Ken. 2000. Three-dimensional analysis of the proximal part of the humerus: Relevance to arthroplasty**. J. Bone Joint Surg**: 1594-1602.

Duda, N.G., F. Mandruzzato, M. Heller, J. Goldhahn, R. Moser, M. Hehli, L. Claes and P.N. Hass. 2001. Mechanical boundary conditions of fracture healing: borderline indications in the treatment of undreamed tibial nailing. **J. Biomech**: 639-650.

Edward, J.M., J.F. Richard, H.A. Yuehuei, C. Rakesh and R.D. Larry. 1997. Anthropometric study of normal glenohumeral relationships. **J. Shoulder Elbow Surg**: 105-112.

Einhorn, T.A. 1995. Enhancement of fracture-healing. **J. Bone Joint Surg**: 940-956.

Epari, D.R., W.R. Taylor, M.O. Heller and G.N. Duda. 2006. Mechanical conditions in the initial phase of bone healing. **J. Clinbiomech**: 646-655.

Farrokh, D., L. Fabeck, P.Y. Descamps, D. Hardy and Ph. Delince. 2001. Computed tomography measurement of humeral head retroversion: Influence of patient positioning. **J. Shoulder Elbow Surg**: 550-553.

Favre, P., R. Sheikh, S.F. Fucentese and A.C.H. Jacob. 2005. An algorithm for estimation of shoulder muscle forces for clinical use. **J. Clinbiomech**: 822-833.

Fernandez, F.F., S. Matschke, A. Hulsenbeck, M. Egenolf and A. Wentzensen. 2003. Five years' clinical experience with the undreamed humeral nail in the treatment of humeral shaft fractures. **J. Care Injuried**: 1-8.

Flinkkila, T. 2004. Intramedullary nailing of humeral shaft fracture. Academic desertation, Faculty of Medicine University of Oulu.

Frederick, J.K., P. Richard and D.Z. Joseph. 1998. The use of the bicipital groove for alignment of the humeral stem in shoulder arthroplasty. **J. Shoulder Elbow Surg**: 144-146.

Gardner, T.N., T. Stoll, L. Marks, S. Mishra and M.K. Tate. 1999. The influence of mechanical stimulus on the pattern of tissue differentiation in a long bone fracture-and FEM study. **J. Biomech**: 415-425.

Gardner, T.N. and S. Mishra. 2003. The biomechanical environment of a bone fracture and its influence upon the morphology of healing. **J. Med Eng Phy**: 455-464.

Gemez-Benito, M.J., J.M. Garcia-Aznar, J.H. Kuiper and M. Doblare. 2005. Influence of fracture gap size on the pattern of long bone healing: a computational study. **J. Theo Bio**: 105-119.

Georg, N.D., M. Francesco, H. Markus, G. Jorg, M. Ruedi, H. Markus, C. Lutz and P.H. Norbert. 2000. Mechanical boundary conditions of fracture healing: borderline indications in the treatment of undreamed tibial nailing. **J. Biomechanics**: 639-650.

Glenn, C.T. and M.C. Thomas. 2000. Functional anatomy of the shoulder. **J. Athletic Training**: 248-255.

Gordon, E. 1999. Variation in the retroversion of the humeral head. **J. Shoulder Elbow Surg**: 142-145.

Grasa, J.M.A., J.A. Perez, J.M. Bea and M.D. Gracia-Aznar. 2005. A probabilistic damage model for acrylic cement: Application to the life prediction of cemented hip implants. **International J. Fatigue**: 1-14.

Gupta, S., F.C.T. Van der Helm and F. van Keulen. 2004. Stress analysis of cemented glenoid prostheses in total shoulder arthroplasty. **J. Biomech**: 1-10.

Gupta, S., F.C.T. Van der Helm and F. van Keulen. 2004. The possibilities of uncemented glenoid component-a finite element study. **J.Clinbiomech**: 292-302.

Halder, S.C. 1992. The Gamma nail for peritrochanteric fractures. **J. Bone Joint Surg**: 340-344.

Halder, A.M., C.G. Halder, K.D. Zhao, S.W. O'Driscoll, B.F. Morrey and K.N. An. 2000. Dynamic inferior stabilizers of the shoulder joint. **J. Clinbiomech**: 138-143.

Harryman, D.T., J.A. Sidles, S.L. Harris, S.B. Lippitt and F.A. Matsen. 1995. The effect of articular conformity and the size of the humeral head component on laxity and motion after glenohumeral arthroplasty: A study in cadaver. **J. Bone Joint Surg**: 555-563.

Hass, N., M. Schutz, N. Sudkamp and R. Hoffmann. 1995. The new undreamed AO nails for the tibia and the femur. **Acta Orthopaedisca Belgica**: 204-206.

Henry. 1918. Anatomy of the human body.

Herron, L.D. and M.H. Newman. 1989. The failure of ethylene oxide gassterilized freeze-dried bone graft for thoracic and lumbar spinal fusion. **Spine**: 496–500.

Hess, S.A. 2000. Functional stability of the glenohumeral joint. **Man.Ther**: 63-71.

Http://fea-cae-engineering.com

Http://www.medical.philips.com/main/products/mri/products/achieva3t/.

Huiskes, R., H. Weinans and H. Van Reitbergen. 1992. The relationship between stress shielding and bone resorption around total hip stems and the effects of flexible materials. **Clin Orthop**: 124-134.

Inman, V.T., H.J. Ralston, J.B. Saunders, B. Feinstein and E.W. Jr Wright. 1952. Relation of human electromyogram to muscular tension. **Electroencephalogr Clin Neurophysiol Suppl**: 187-194.

Inman, V.T., M. Saunders and L.C. Abbot. 1944. Observations on the function of the shoulder joint. **J. Bone Joint Surg**: 1-30.

Jennifer, A.D., T.B. Ryan, A.M. Geoff, M.F. Louis, E.D. Cynthia, J.W.K. Graham, A.J. James and S.D. Darren. 2007. An anthropometric study of the bilateral anatomy of the humerus. **J. Shoulder Elbow Surg**: 1-7.

Joseph, P.I., P.G. Josue, L.C. Stephanie, G.E. Brian and M. Sanjay. 1992. The normal glenohumeral relationship. **J. Bone Joint Surg**: 491-500.

Kalfas, I.H. 2001. Principles of bone healing. **Neurosurg Focus**: 1-4.

Kamineni, S., H. Ankem and S. Sanghavi. 2004. Anatomical considerations for percutaneous proximal humeral fracture fixation. **J. Care Injuried**: 1-4.

Karlsson, D. and B. Peterson. 1992. Towards a model for force predictions in the human shoulder. **J. Biomech**: 189-199.

Katsumi, T., Y. Kengo, I. Atsuhiro and Z.B. Wayne. 2004. The radiographic study in the relationship of the glenohumeral joint. **J. Orthopaedic**: 298-305.

Kedgley, A.E., G.A. Mackenzie, L.M. Ferreira, D.S. Drosdowech, G.J.W. King, K.J. Faber and J.A. Johnson. 2007. The effect of muscle loading on the kinematics of in vitro glenohumeral abduction. **J. Biomechanics**: 1-8.

Kent, M.E., C. Sinopidis, D.J. Brown and S.P. Frostick. 2005. The locking compression plate in periprosthetic humeral fracture: A review of two cases. **J. Care Injured**: 1-5.

Kronberg, M., G. Nemeth and L.A. Brostrom. 1990. Muscle activity and coordination in the normal shoulder. **Clin. Orthop**: 76-85.

Laurent, G.F., F. Dordaneh, T. Michael, E.T. Philippe, Z. Chafiq and E.D. Philippe. 2001. Computed tomography evaluation of shoulder prosthesis retroversion. **J. Shoulder Elbow Surg**: 546-549.

Lee, S.B., K.J. Kim, S.W. O'Driscoll, B.F. Morrey and K.N. An. 2000. Dynamic glenohumeral stability provided by the rotator cuff muscle in the mid-range and end-range of motion. **J. Bone Joint Surg**: 849-857.

Leung, K.S., P. Procter, B. Robioneck and K. Behrens. 1996. Geometric mismatch of the gamma nail to the Chinese femur. **Clinical Orthopaedics and Related Research**: 42-48.

Levasseur, A., P. Tetreault, J. de Guise, N. Nuno and N. Hagemeister. 2007. The effect of axis alignment on shoulder joint kinematics analysis during arm abduction. **J. Clinbiomech**: 1-9.

Lieven, F. De W., M.B. Bart, V. Frederic, S. Alexander and C.V. Rene. 2003. Glenohumeral relationship in the transverse plane of the body. **J. Shoulder Elbow Surg**: 260-267.

Lin, J., N. Inoue, A. Valdevit, Y.S. Hang, S.M. Hou and E.Y.S. Chao. 1997. Biomechanical comparison of antegrade and retrograde nailing of humeral shaft fracture. **J. Clinorthop**: 203-213.

MacMahon, P.J., R.E. Debski, W.O. Thompson, J.J.P. Warner, F.H. Fu and S.L. Woo. 1995. Shoulder muscle forces and tendon excursions during glenohumeral abduction in the scapular plane. **J. Shoulder Elbow Surg**: 199-208.

Mahaisavariya, B., K. Sitthiseripratip, T. Tongdee, L.J.E. Bohez, V.J. Sloten and P. Olis. 2002. Morphological study of the proximal femur: a new method of geometrical assessment using 3-dimensional reverse engineering. **J. Medical Engineering & Physics**: 617-622.

Mahaisavariya, B., K. Sitthiseripratip, P. Oris, E. Chaichanasiri and J. Suwanprateeb. 2004. Fit-and-fill analysis of trochanteric gamma nail for the thai proximal femur: A virtual simulation study. **J. Med Assoc Thai**: 1315-1320.

Maldonado, Z.M., J. Seebeck, M.O.W. Heller, D. Brandt, P. Hepp, H. Lill and G.N. Duda. 2003. Straining of the intact and fractured proximal humerus under physiological-like loading. **J. Biomech**: 1865-1873.

McMahon, P.J., R.E. Debski, W.O. Thompson, J.J.P. Warner, F.H. Fu and S.L-Y. Woo. 1995. Shoulder muscle forces and tendon excursions during glenohumeral abduction in the scapular plane. **J. Shoulder Elbow Surg**: 199-208.

Michael, L.P. and G.V. Albert. 1995. Retroversion of the proximal humerus in relationship to prosthetic replacement arthroplasty. **J. Shoulder Elbow Surg**: 286-289.

Michael, L.P. and G.V. Albert. 1996. Coronal plane geometry of the proximal humerus relevant to prosthetic arthroplasty. **J. Shoulder Elbow Surg**: 320-326.

Michael, L.P. and K. Sam. 1999. Geometric analysis of commonly used prosthetic systems for proximal humeral replacement. **J. Bone Joint Surg**: 660-670.

Michael, L.P., K. Sam, D.R. Douglas and Y. Ken. 2002. Geometric analysis of selected press fit prosthetic systems for proximal humeral replacement. **J. Orthopaedic**: 192-197.

Michael, L.P. 2005. Proximal humeral anatomy in shoulder arthroplasty: Implications for prosthetic design and surgical technique. **J. Shoulder Elbow Surg**: 99-104.

Moaveni, S. 1999. **Finite Element Analysis Theory and Application with ANSYS.** Prentice-Hall, Inc., New Jersey.

Murray, W.A., T.S. Buchanan and S.L. Delp. 2000. The isometric functional capacity of muscles that cross the elbow. **J. Biomech**: 943-952.

Perez, A., A. Mahar, C. Negus, P. Newton and T. Impelluso. 2007. A computational evaluation of the effect of intramedullary nail material properties on the stabilization of simulated femoral shaft fractures. **J. Med Eng Phy**: 1-6.

Plausinis, D., C. Greaves, W.D. Regan and T.R. Oxland. 2005. Ipsilateral shoulder and elbow replacements: on the risk of periprosthetic fracture. **J. Clinbiomech**: 1055-1063.

Poppen, K.N. and P.S. Walker. 1978. Forces at the glenohumeral joint. **Clin. Orthop**: 165-170.

Program Dynamic Human Anatomy 2.0

Ralph, H., K. Ulf and T.B. Franz. 2002. Geometry of the proximal humerus and implications for prosthetic design. **J. Shoulder Elbow Surg**: 331-338.

Recker, R.R. 1992. Embryology, anatomy, and microstructure of bone, in Coe FL, Favus MJ (eds): Disorders of Bone and Mineral Metabolism. New York, Raven: 219–240.

Reynolds, A.K.R. and H. Jackson. 2005. Concept of treatment in supracondylar humeral fractures**. J. Care Injuried**: 51-56.

Riebel, E.D., S.D. Boden and T.E. Whitesides. 1995. The effect of nicotine on incorporation of cancellous bone graft in an animal model. **Spine**: 2198–2202.

Ringelberg, J.A. 1985. EMG and force production of some human shoulder muscles during isometric abduction. **J. Biomechanics**: 939-947.

Rubenstein, I., T. Yong and S.I. Rennard. 1991. Cigarette smoke extract attenuates endothelium-dependent arteriolar dilation in vivo. **Am J Physiol**: H1913–H1918.

Ryan, T.B., A.D. Jen, E.K. Angela, M.F. Louis, E.D. Cynthia, J.W.K. Graham, J.F. Ken, A.J. James and S.D. Darren. 2006. Early experience with computer-assisted shoulder hemiarthroplasty for fractures of the proximal humerus: Development of a novel technique and an in vitro comparison with traditional methods. **J.Shoulder Elbow Surg**: 1-9.

Seide, K., J. Triebe, M. Faschingbauer, A.P. Schulz, K. Puschel, G. Mehrtens and Ch. Jurgens. 2007. Locked vs. unlocked plate osteosynthesis of the proximal humerus-A biomechanical study. **J. Clinbiomech**: 176-182.

Silcox, D.H. III, T. Daftari and S.D. Boden. 1995. The effects of nicotine on spinal fusion. **Spine**: 1549–1553.

Sitthiseripratip, K., H. van Oosterwyck, J.V. Sloten, B. Mahaisavariya, E.L.J. Bohez, J. Suwanprateeb, R. van Audekercke and P. Oris. 2002. Finite element study of trochanteric gamma nail for trochanteric fracture. **J. Med Eng Phy**: 99-106.

Su, C.S., G.J. Skedros, N.K. Bachus and D.R. Bloebaum. 1999. Loading conditions and cortical bone construction of an artiodactyls calcaneus. **J. Exp Bio**: 3239-3254.

Terrier, A., A. Reist, A. Vogel and A. Farron. 2007. Effect of supraspinatus deficiency on humerus translation and glenohumeral contact force during abduction. **J. Clinbiomech**: 645-651.

Van de Griend, R., J. Tomasin and E.F. Ward. 1986. Open reduction and internal fixation of humeral shaft fractures. **J. Bone Joint Surg**: 430-433.

Van der Helm, F.C.T. and R. Veenbaas. 1991. Modelling the mechanical effect of muscles with large attachment sites: Application to the shoulder mechanism. **J. Biomechanics**: 1151-1163.

Van der Helm, F.C.T. 1994. Analysis of the kinematic and dynamic behavior of the shoulder mechanism. **J. Biomech**: 527-550.

Van der Helm, F.C.T. 1994. A finite element musculoskeletal model of the shoulder mechanism. **J. Biomech**: 551-569.

Van der Helm, F.C.T. and G.M. Pronk. 1995. Three-dimensional recording and description of motions of the shoulder mechanism. **J. Biomech Eng**: 27-40.

Verbruggen, J.P.A.M. and J.W.J.L. Stapert. 2005. Failure of reamed nailing in humeral non-union: an analysis of 26 patients. **J. Care Injuried**: 430-438.

Walch, G. and P. Boileau. 1999. Prosthetic adaptability: A new concept for shoulder arthroplasty. **J. Shoulder Elbow Surg**: 443-451.

Walsh, S., R. Reindl, E. Harvey, G. Berry, L. Beckham and T. Steffen. 2006. Biomechanical comparison of a unique locking plate versus a standard plate for internal fixation of proximal humerus fractures in a cadaveric model. **J. Clinbiomech**: 1027-1031.

Warner, C.M.L., P. Favre and C. Gerber. 2007. The role of the subscapularis in preventing anterior glenohumeral subluxation in the abducted, externally rotated position of the arm. **J. Clinbiomech**: 495-501.

Wataru, S., S. Kazuomi, N. Yoshikazu, I. Hiroak, Y. Takaharu and Y. Hideki. 2005. Three-dimensional morphological analysis of humeral heads. ***J.*** **Acta Orthopaedica**: 392-47 396.

White, A.A. III and C. Hirsch. 1971. An experimental study of the immediate load bearing capacity of some commonly used iliac bone grafts. **Acta Orthop Scand**: 482–490.

Wolff, J. 1986. The Law of Bone Remodelling. Translated by Maquet P. Furlong R. Berlin: Springer-Verlag.

Wood, J.E., S.G. Meek and S.C. Jacobsen. 1989. Quantitation of human shoulder anatomy for prosthetic arm control-I. Surface modeling. **J. Biomech**: 273-292.

Wuelker, N., C.J. Wirth, W. Plitz and B. Roetman. 1993. A dynamic shoulder model: Reliability testing and muscle force study. **J. Biomechanics**: 489-499.

APPENDIX

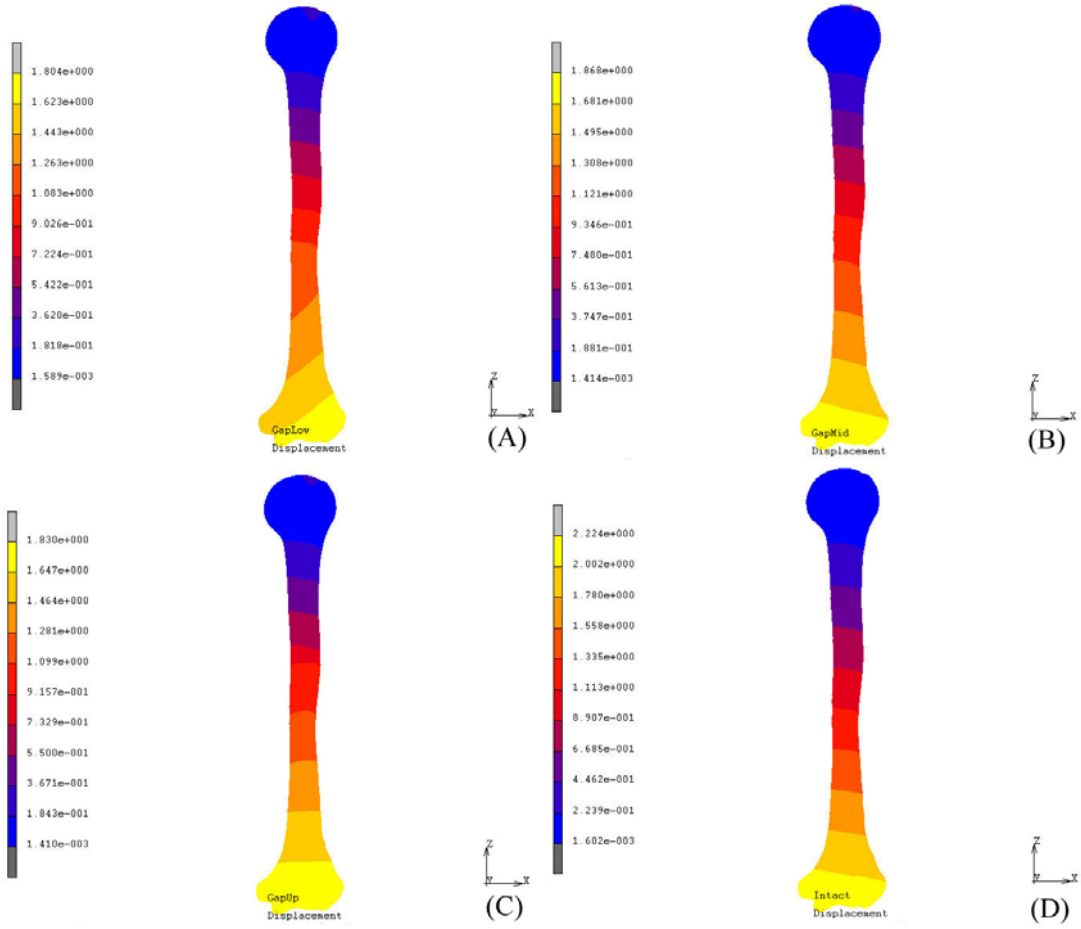

Appendix Figure 1 The displacement of the humeral bone with the antegrade insertion technique at zero degrees abduction: (A) Lower gap, (B) Medium gap, (C) Upper gap, and (D) Intact condition.

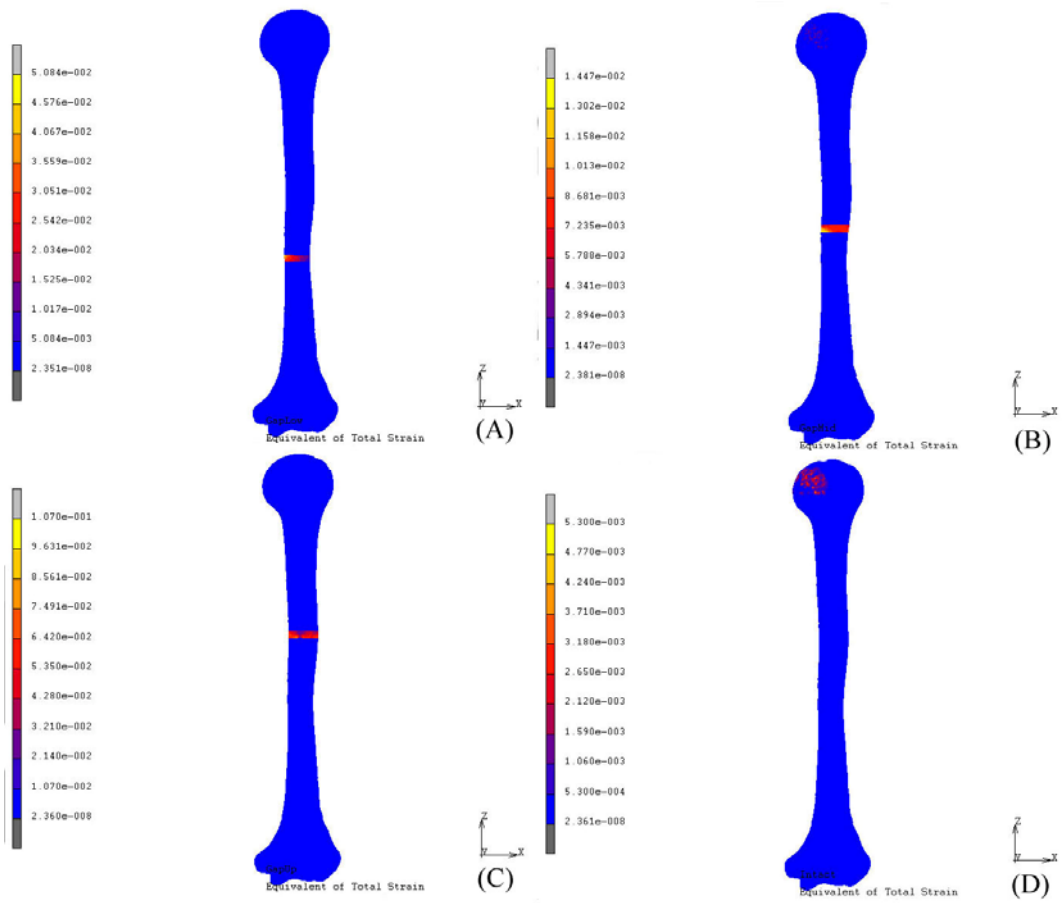

Appendix Figure 2 The total strain on humeral bone with the antegrade insertion technique at zero degrees abduction: (A) Lower gap, (B) Medium gap, (C) Upper gap, and (D) Intact condition.

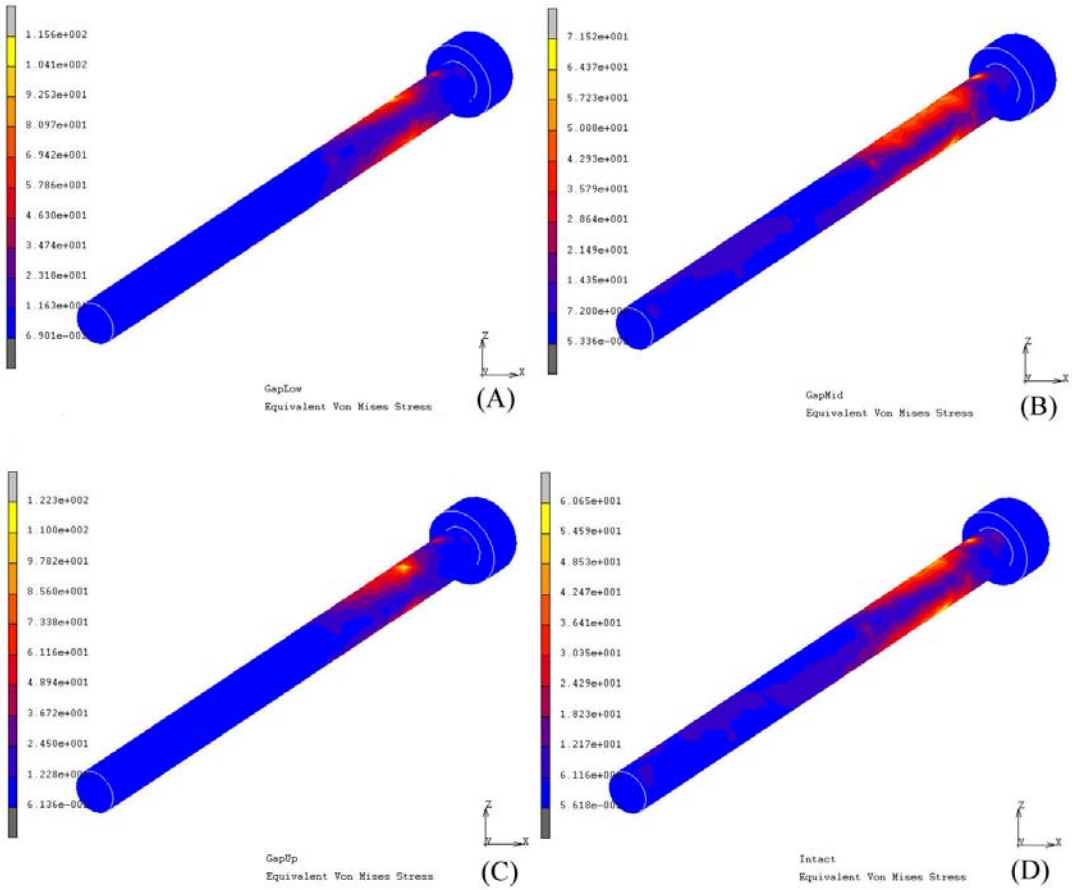

Appendix Figure 3 The von Mises stress on the proximal screw with the antegrade insertion technique at zero degrees abduction: (A) Lower gap, (B) Medium gap, (C) Upper gap, and (D) Intact condition.

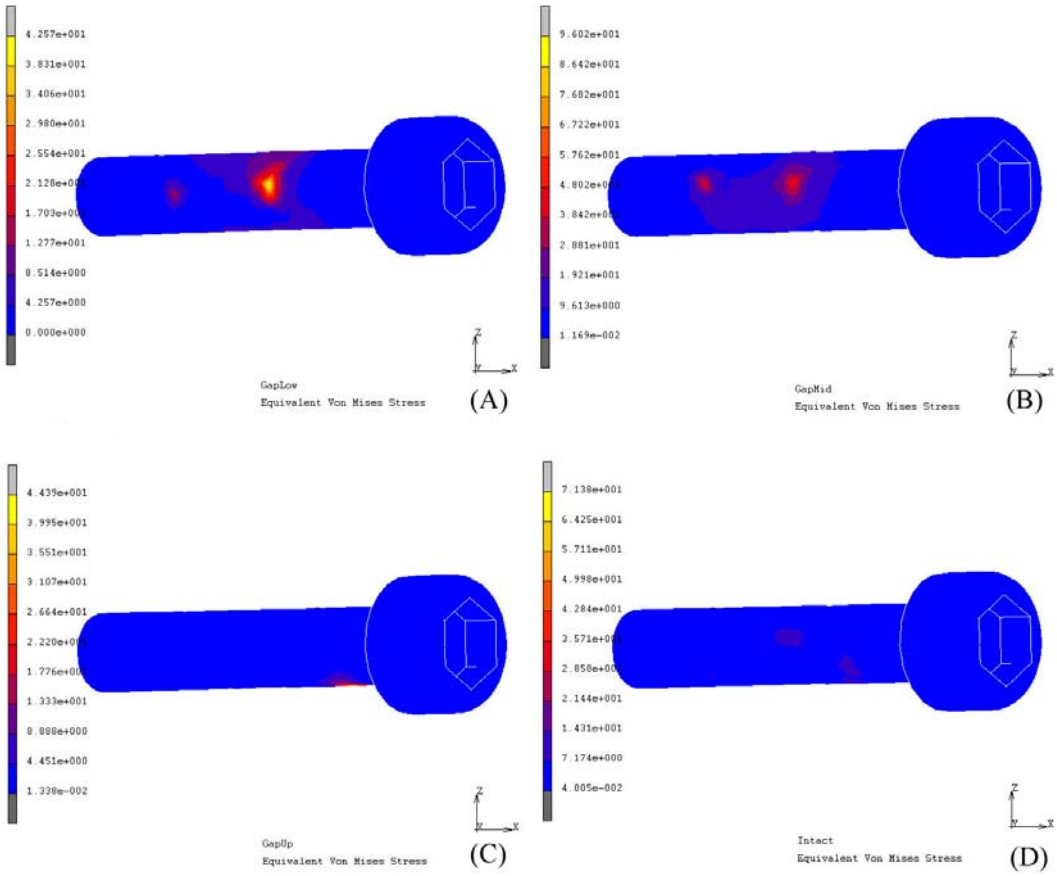

Appendix Figure 4 The von Mises stress on the distal screw with the antegrade insertion technique at zero degrees abduction: (A) Lower gap, (B) Medium gap, (C) Upper gap, and (D) Intact condition.

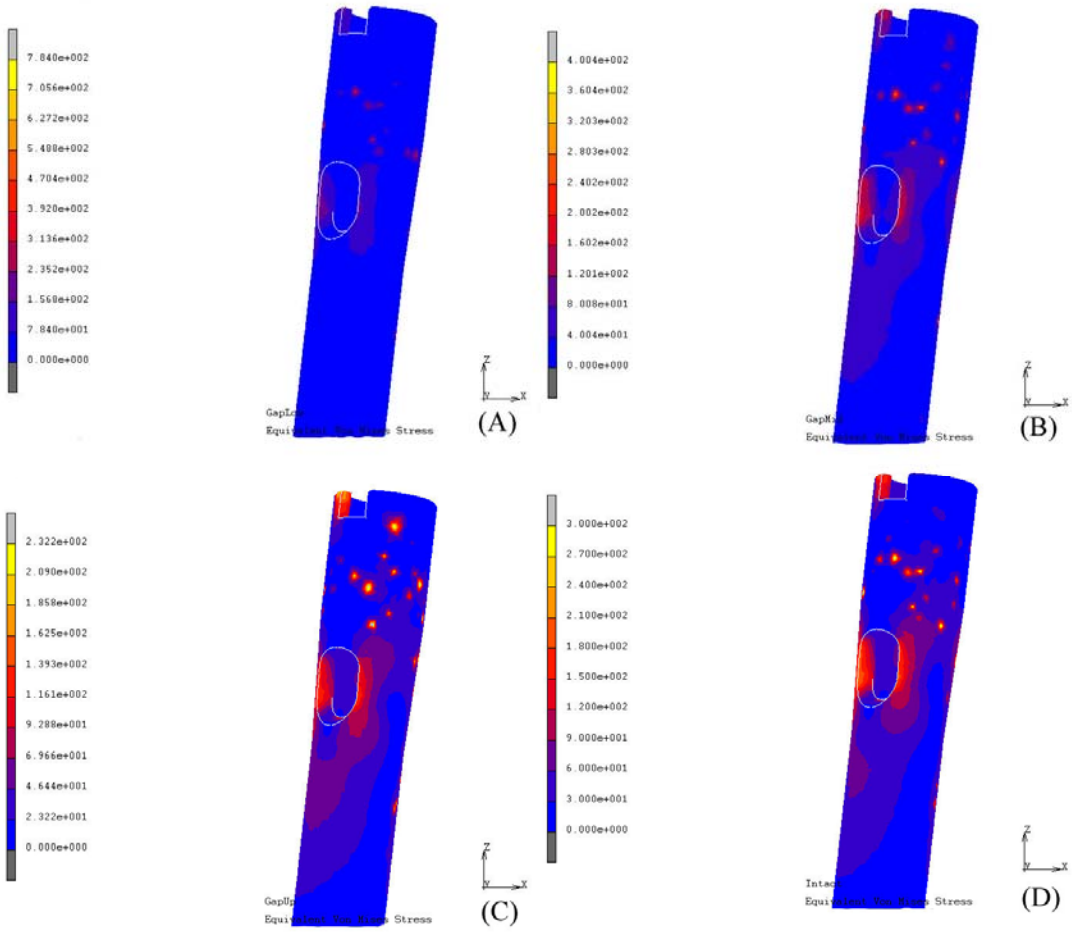

Appendix Figure 5 The von Mises stress on the proximal screw hole on the humeral nail with the antegrade insertion technique at zero degrees abduction: (A) Lower gap, (B) Medium gap, (C) Upper gap, and (D) Intact condition.

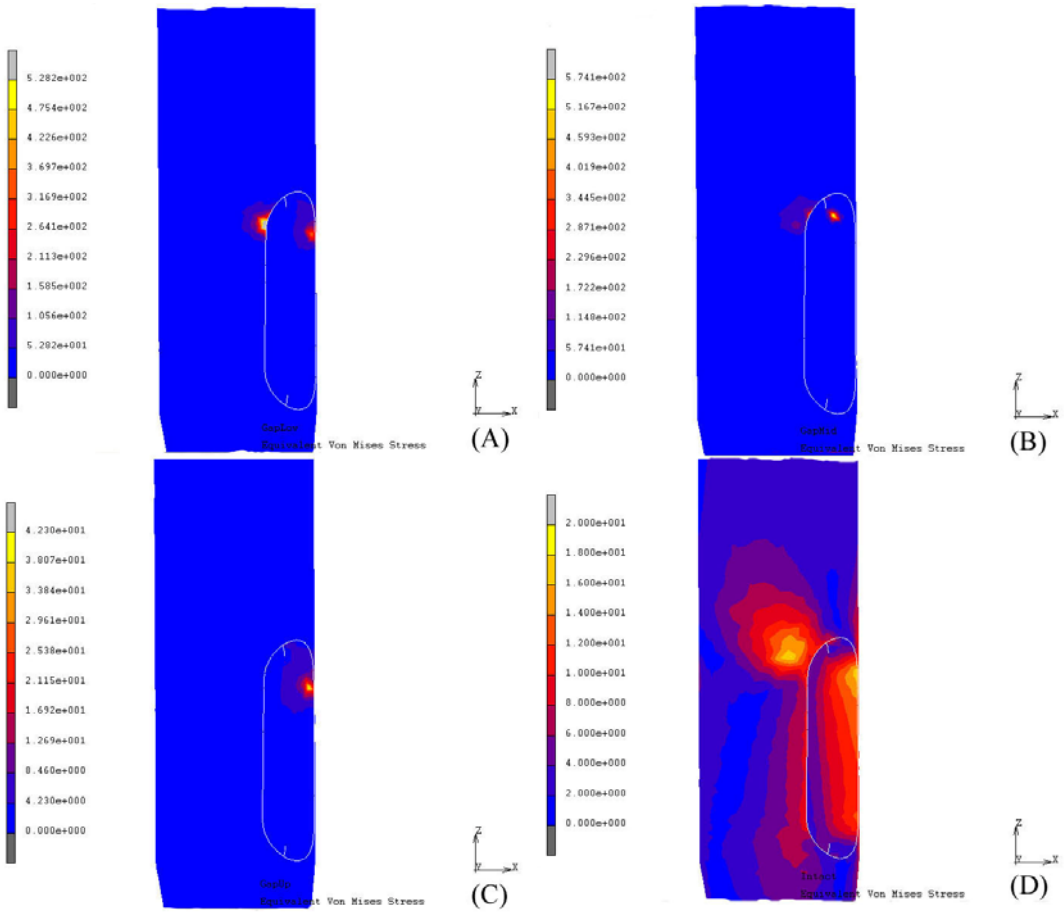

Appendix Figure 6 The von Mises stress on the distal screw hole on the humeral nail with the antegrade insertion technique at zero degrees abduction: (A) Lower gap, (B) Medium gap, (C) Upper gap, and (D) Intact condition.

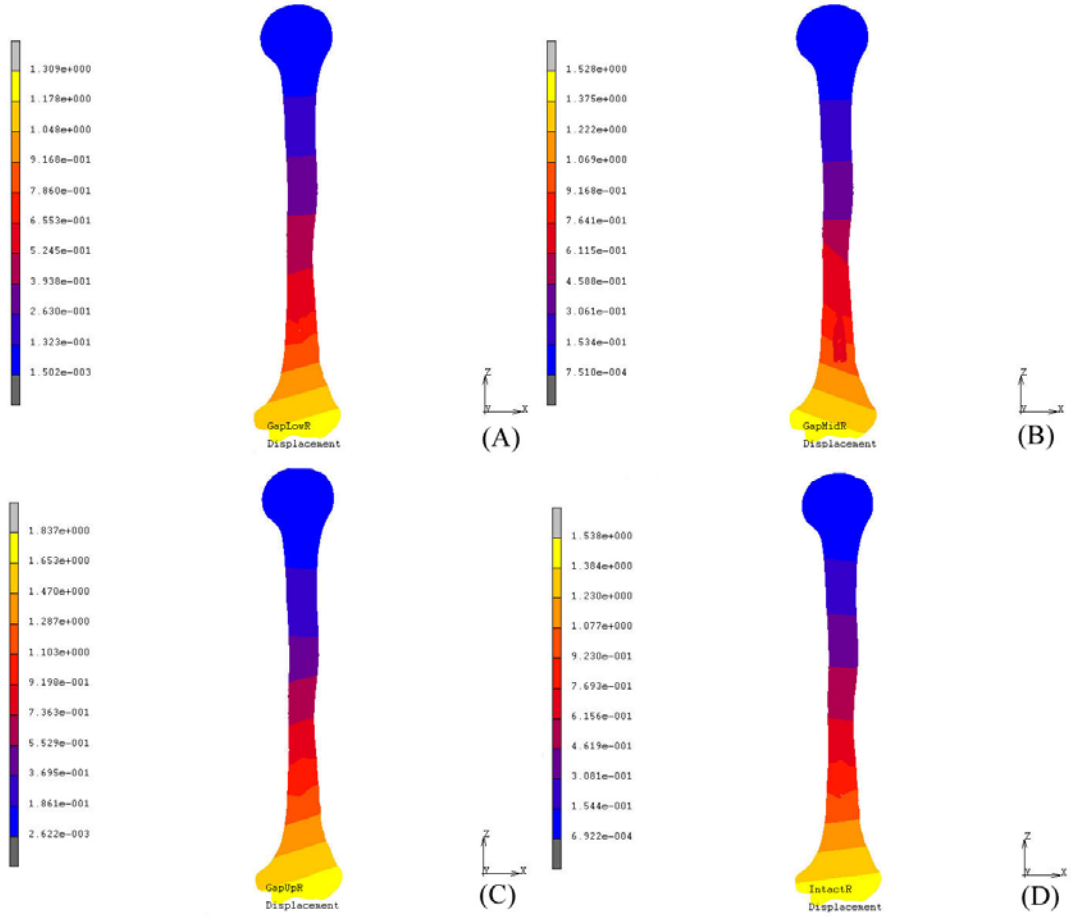

Appendix Figure 7 The displacement of the humeral bone with the retrograde insertion technique at zero degrees abduction: (A) Lower gap, (B) Medium gap, (C) Upper gap, and (D) Intact condition.

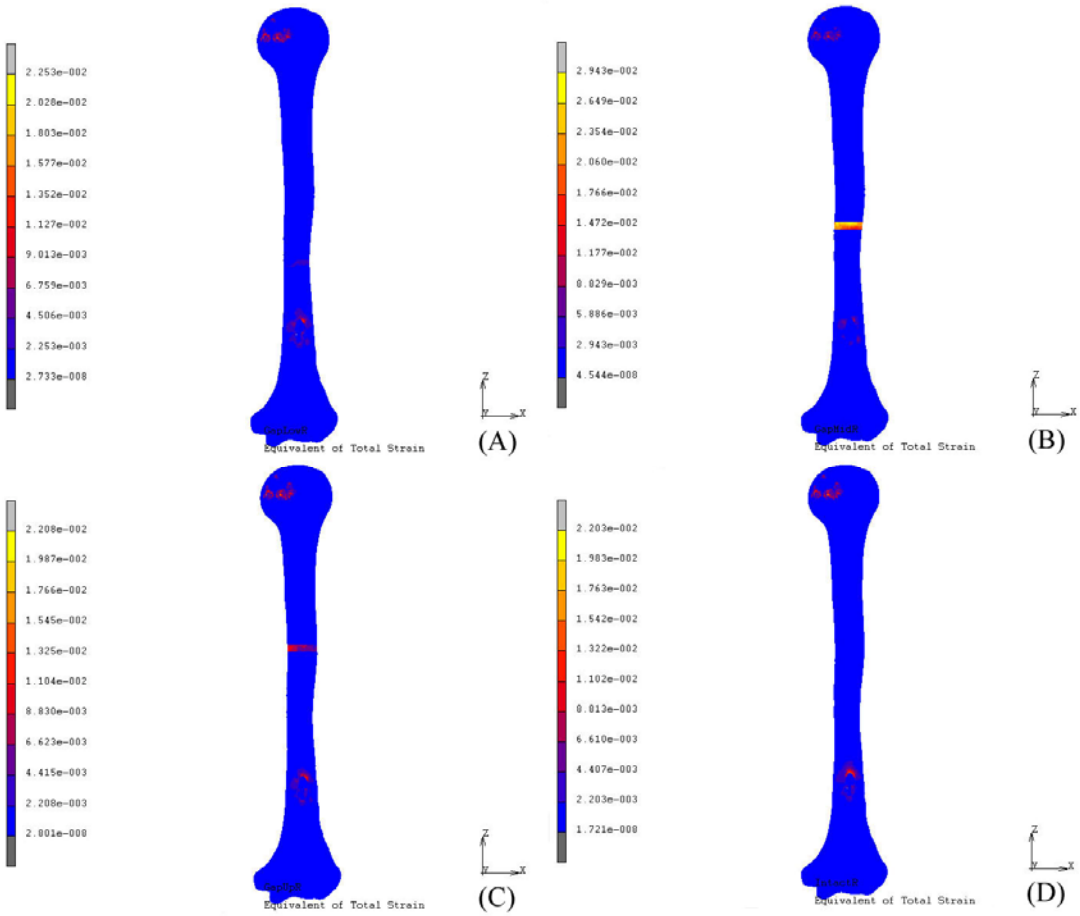

Appendix Figure 8 The total strain on the humeral bone with the retrograde insertion technique at zero degrees abduction: (A) Lower gap, (B) Medium gap, (C) Upper gap, and (D) Intact condition.

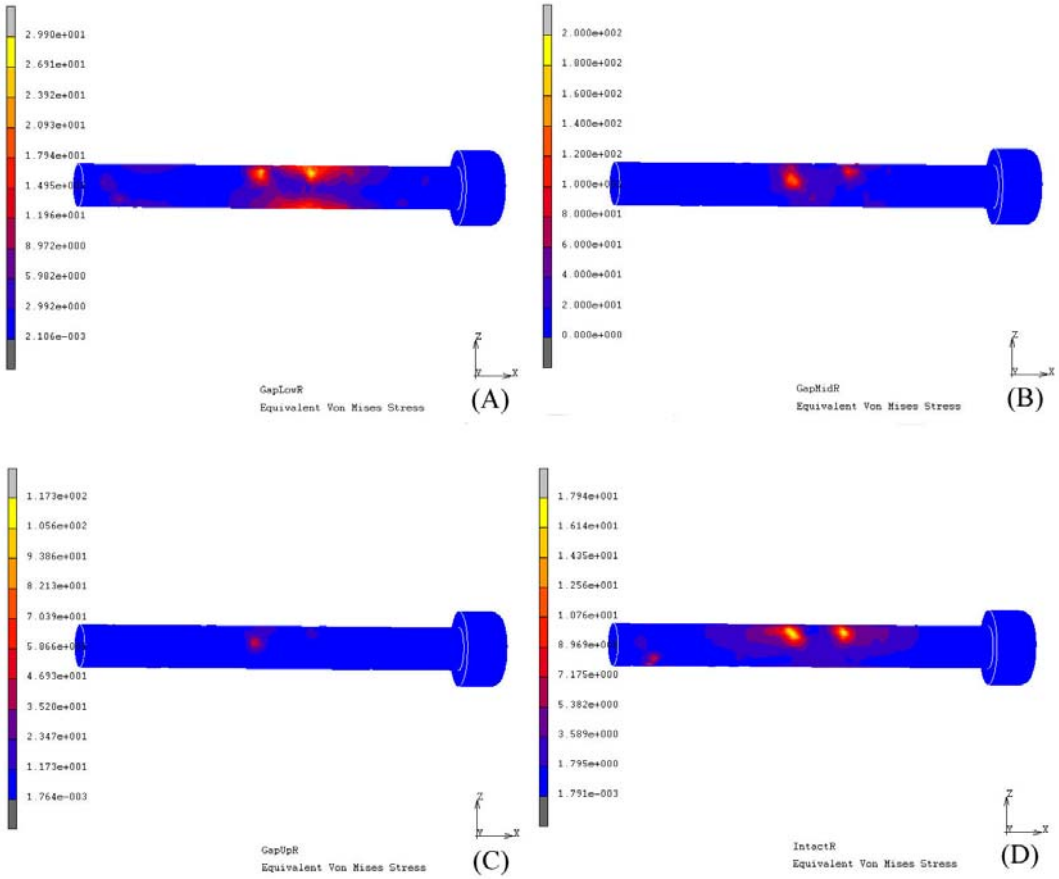

Appendix Figure 9 The von Mises stress on the proximal screw with the retrograde insertion technique at zero degrees abduction: (A) Lower gap, (B) Medium gap, (C) Upper gap, and (D) Intact condition.

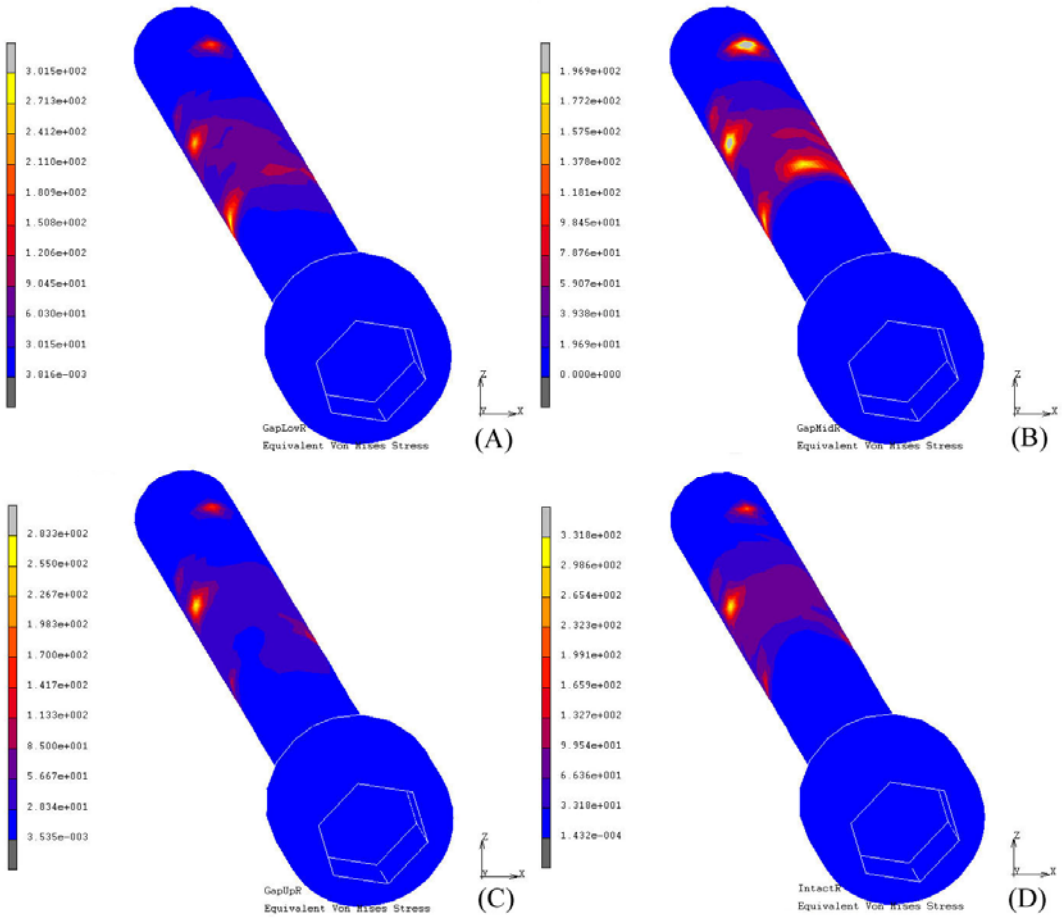

Appendix Figure 10 The von Mises stress on the distal screw on the humeral nail with the retrograde insertion technique at zero degrees abduction: (A) Lower gap, (B) Medium gap, (C) Upper gap, and (D) Intact condition.

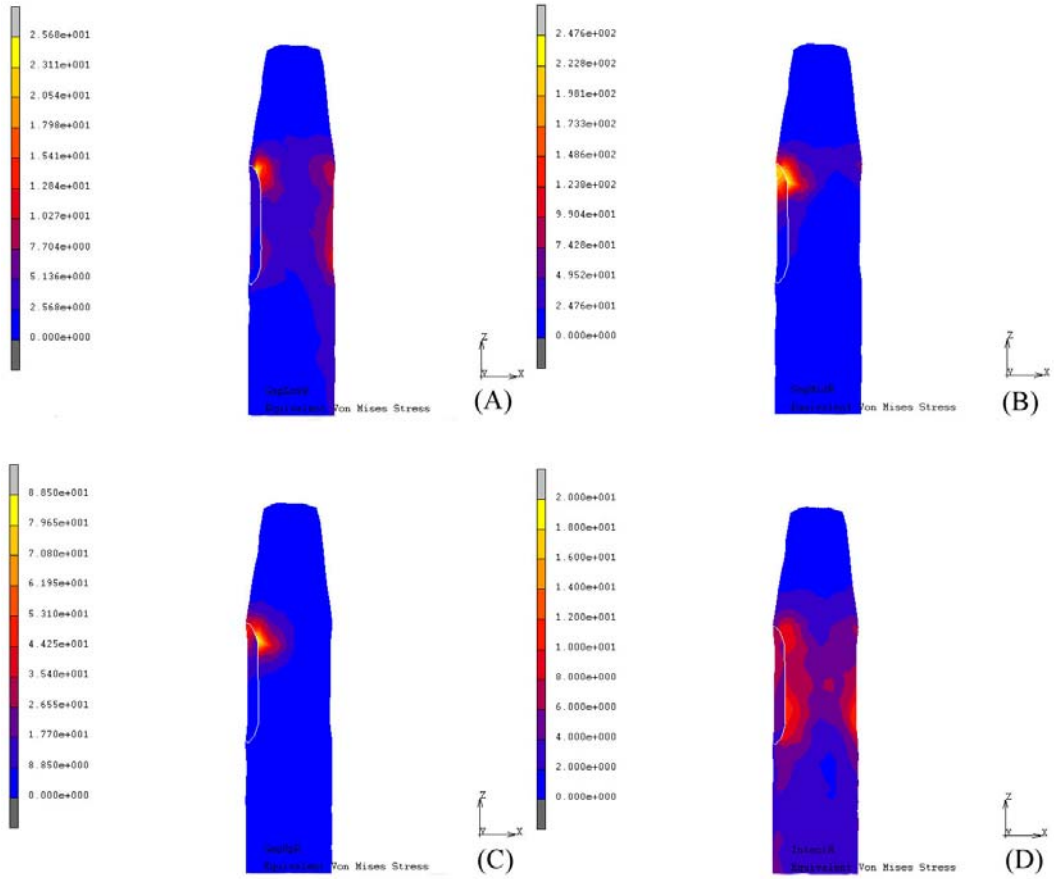

Appendix Figure 11 The von Mises stress on the proximal screw hole on the humeral nail with the retrograde insertion technique at zero degrees abduction: (A) Lower gap, (B) Medium gap, (C) Upper gap, and (D) Intact condition.

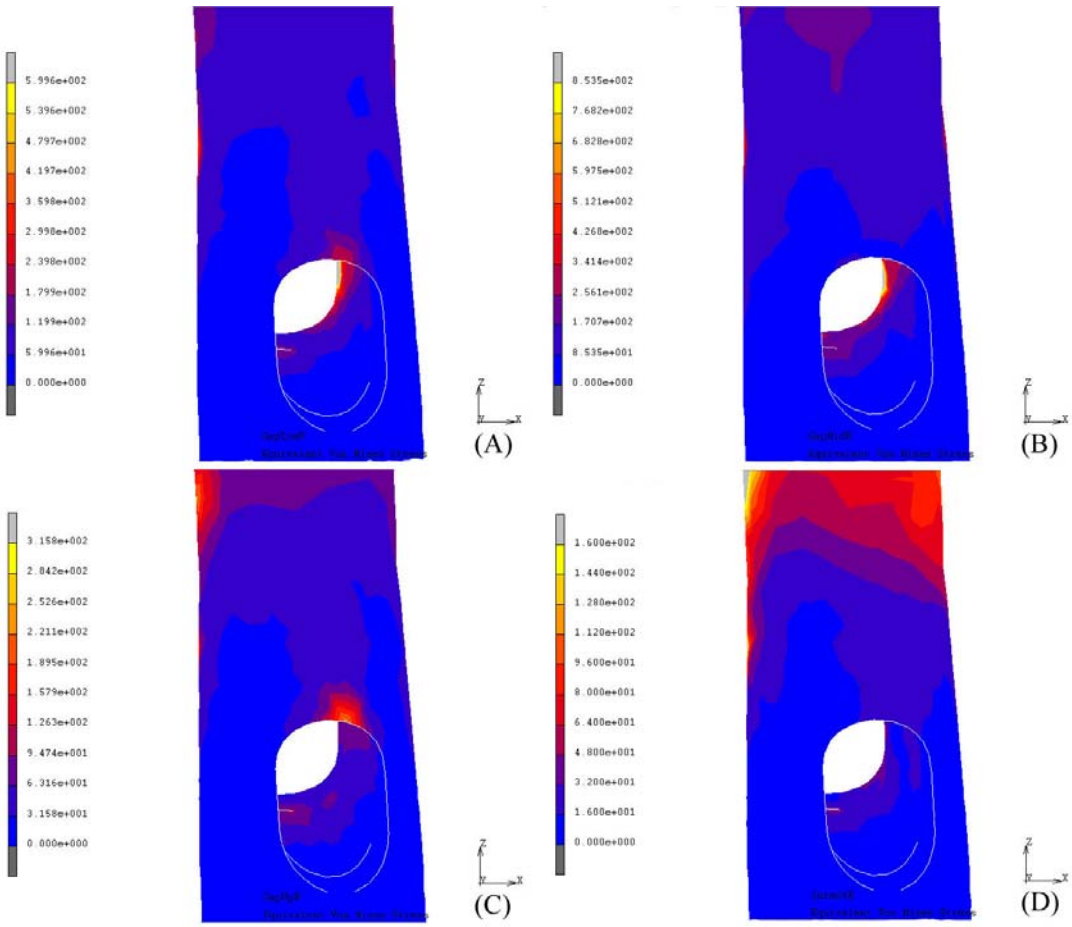

Appendix Figure 12 The von Mises stress on the distal screw hole on the humeral nail with the retrograde insertion technique at zero degrees abduction: (A) Lower gap, (B) Medium gap, (C) Upper gap, and (D) Intact condition.

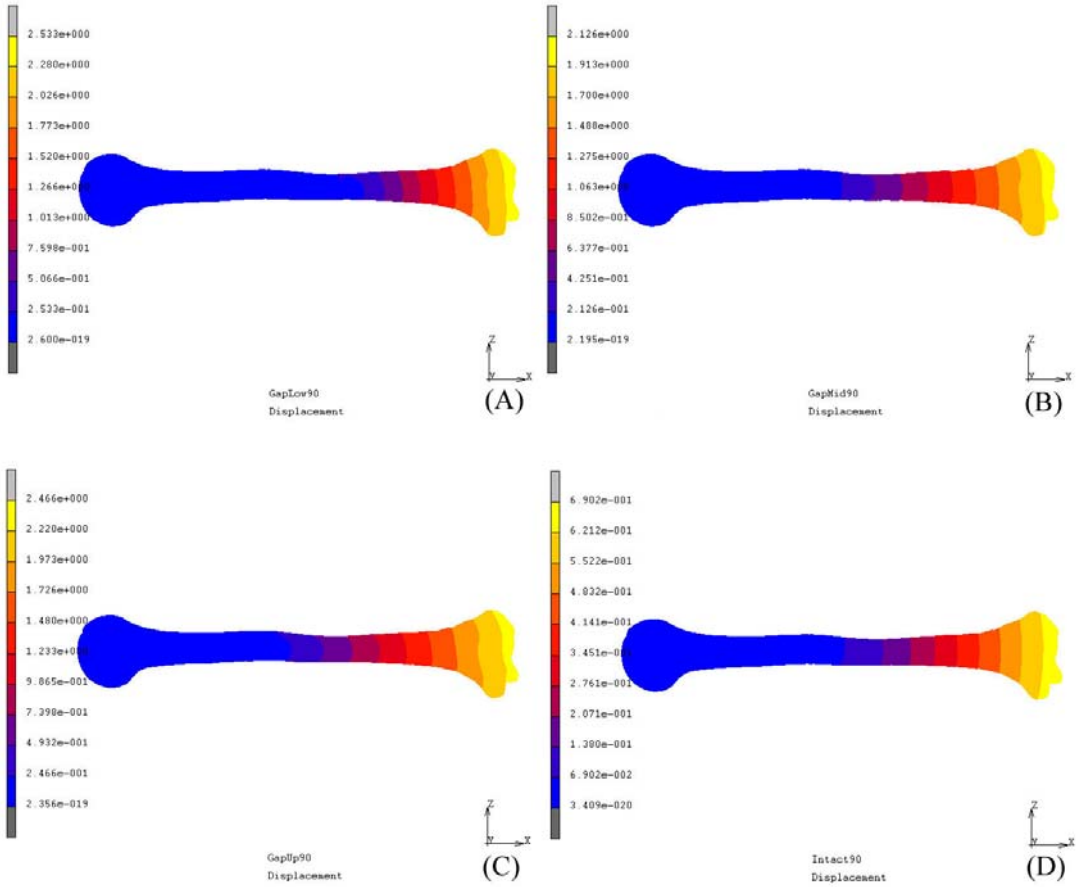

Appendix Figure 13 The displacement of the humeral bone with the antegrade insertion technique at ninety degrees abduction: (A) Lower gap, (B) Medium gap, (C) Upper gap, and (D) Intact condition.

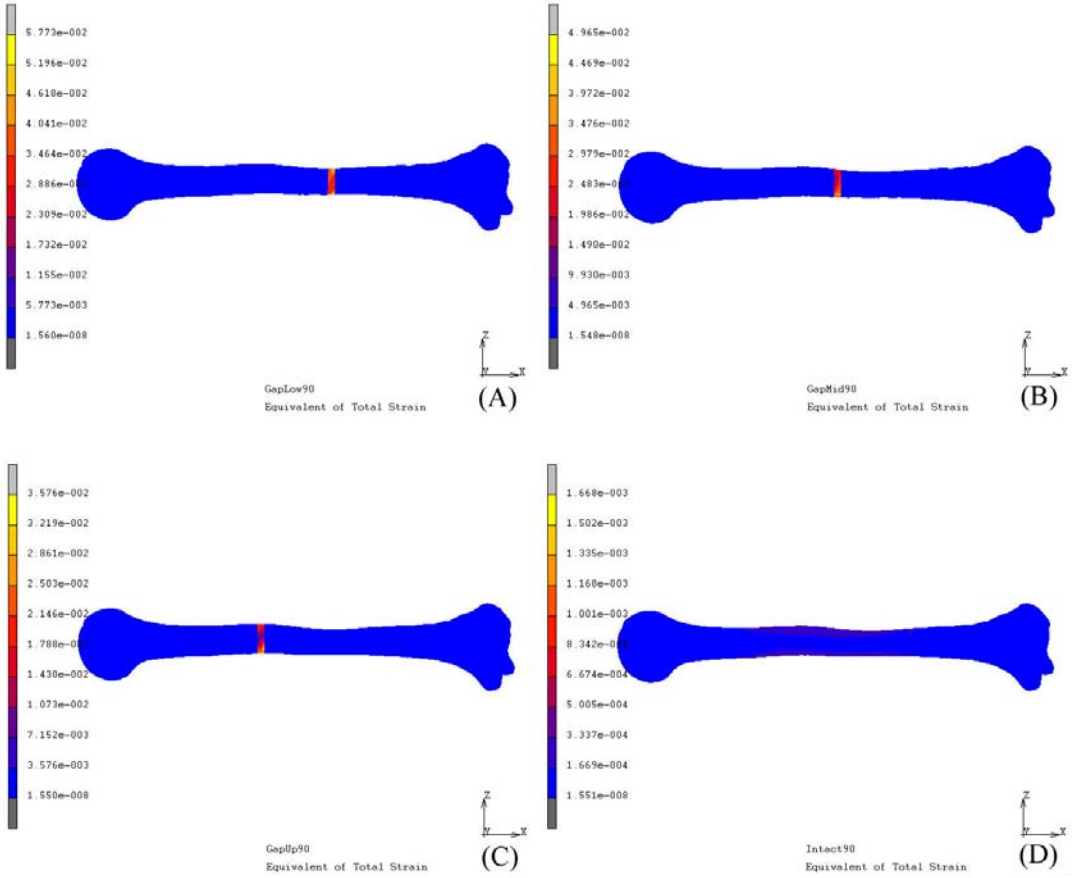

Appendix Figure 14 The total strain on the humeral bone with the antegrade insertion technique at ninety degrees abduction: (A) Lower gap, (B) Medium gap, (C) Upper gap, and (D) Intact condition.

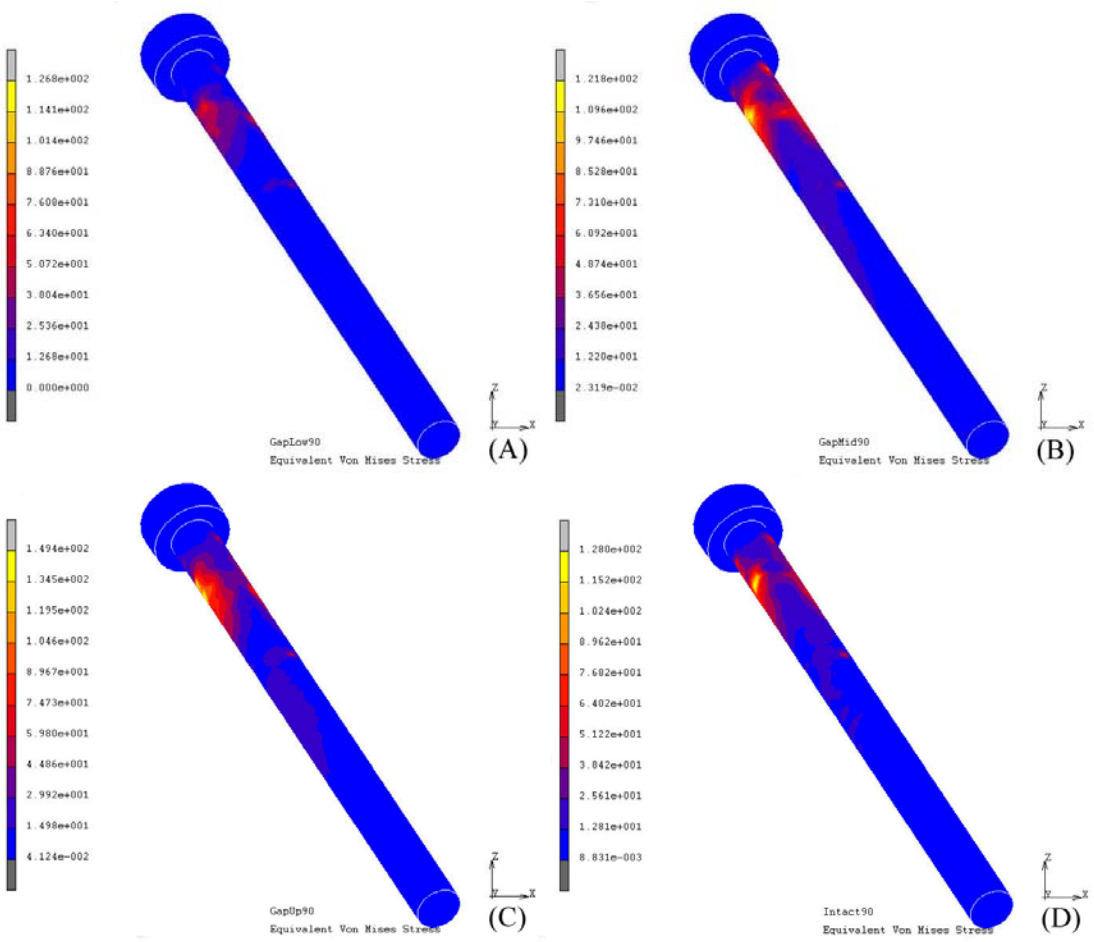

Appendix Figure 15 The von Mises stress on the proximal screw with the antegrade insertion technique at ninety degrees abduction: (A) Lower gap, (B) Medium gap, (C) Upper gap, and (D) Intact condition.

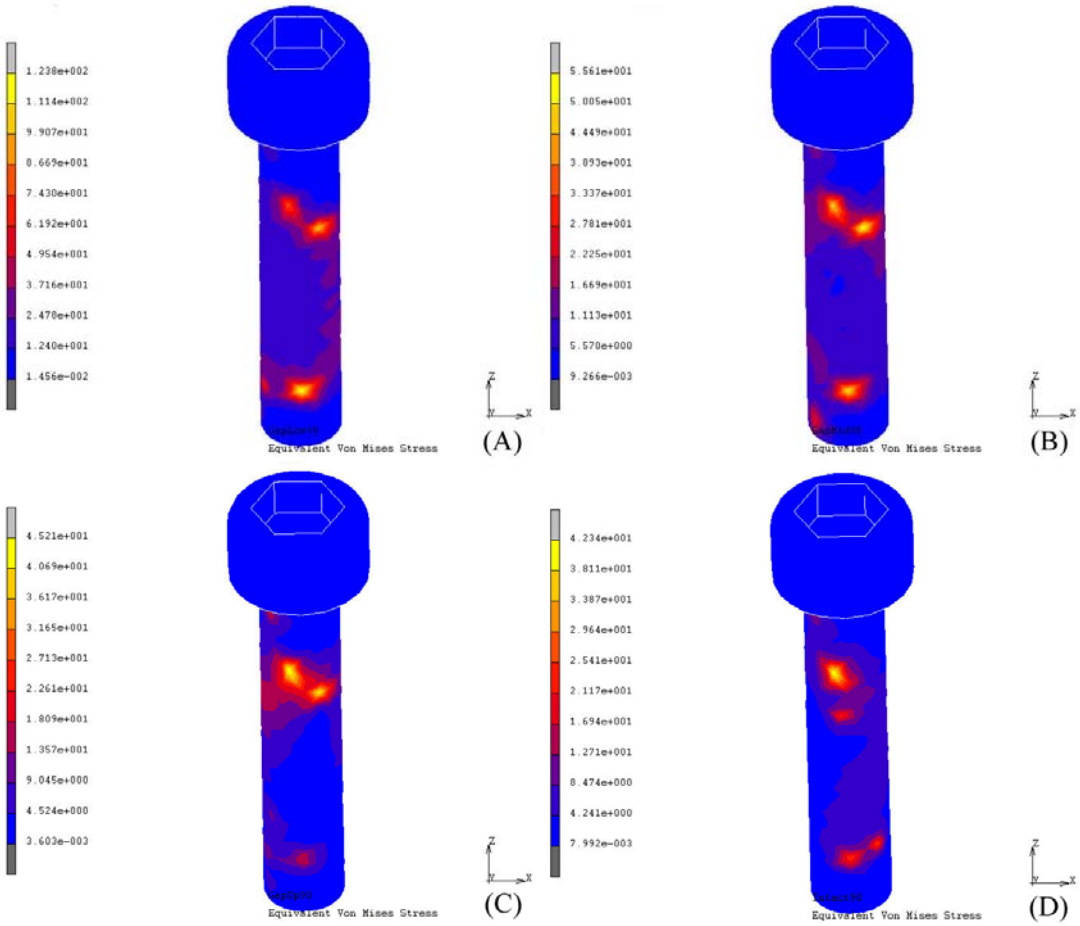

Appendix Figure 16 The von Mises stress on the distal screw with the antegrade insertion technique at ninety degrees abduction: (A) Lower gap, (B) Medium gap, (C) Upper gap, and (D) Intact condition.

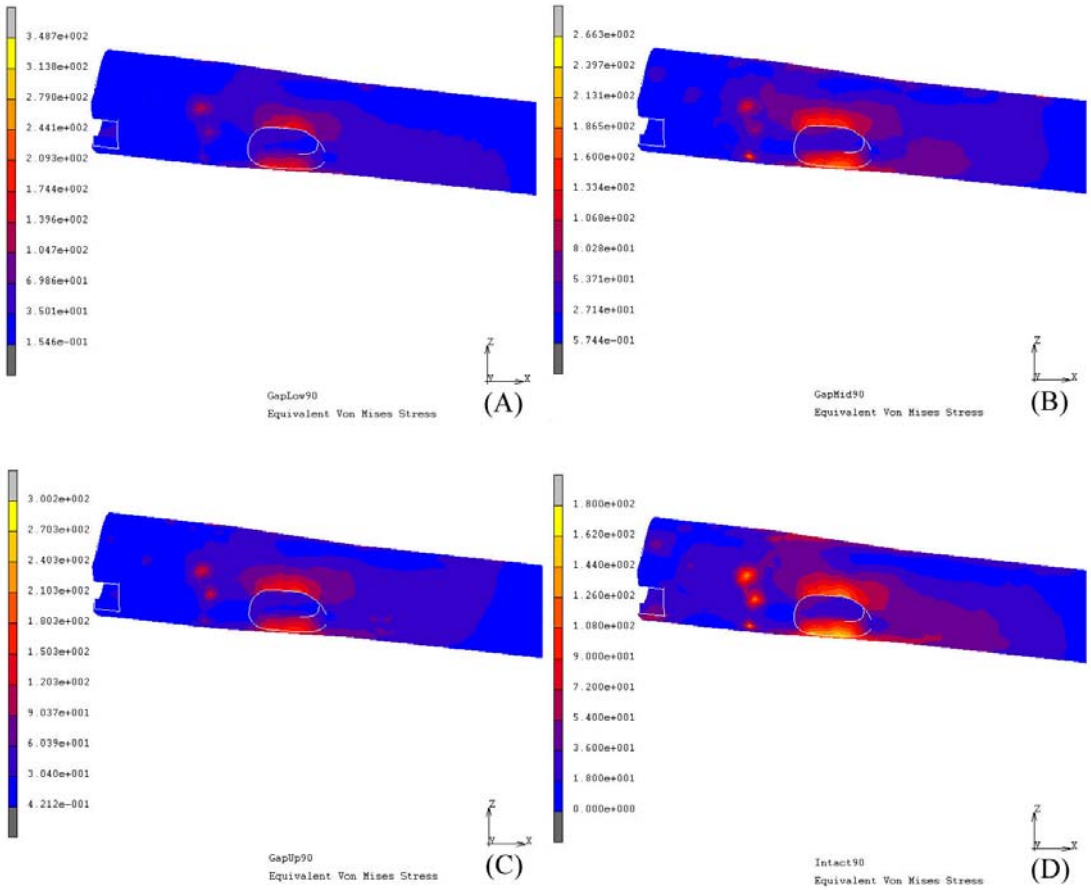

Appendix Figure 17 The von Mises stress on the proximal screw hole on the humeral nail with the antegrade insertion technique at ninety degrees abduction: (A) Lower gap, (B) Medium gap, (C) Upper gap, and (D) Intact condition.

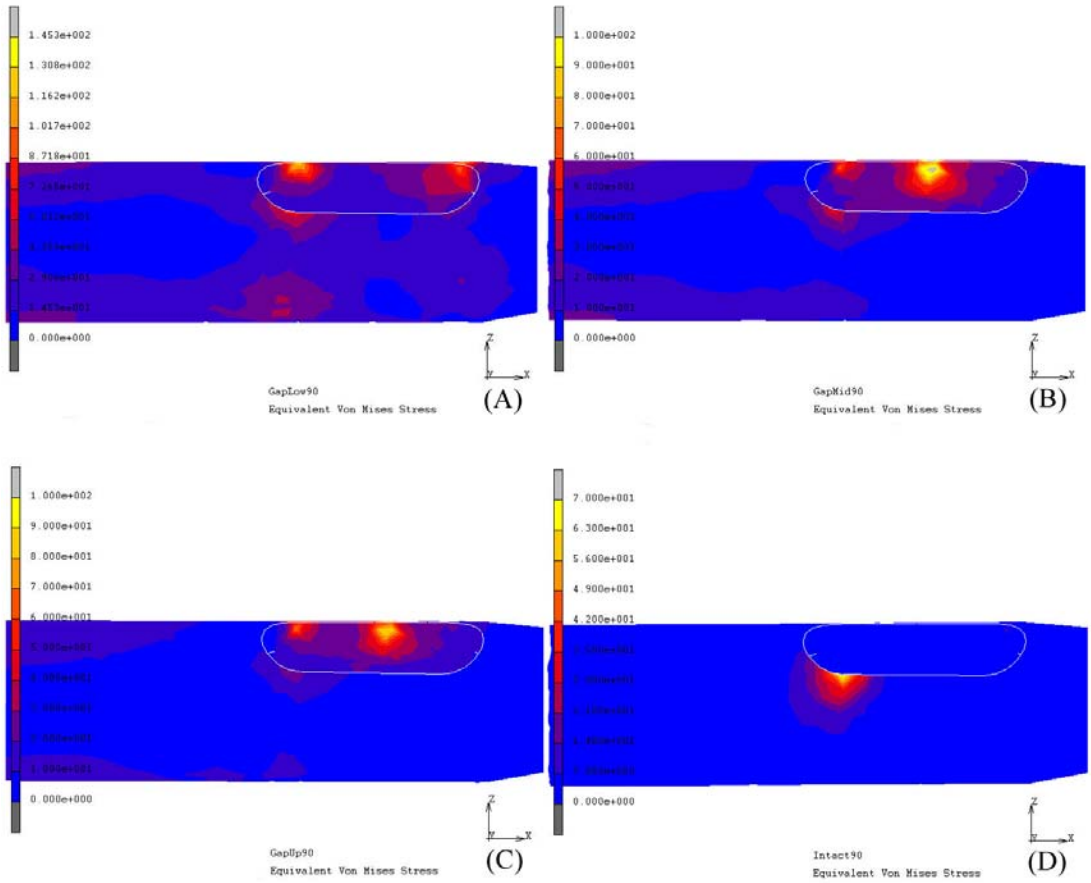

Appendix Figure 18 The von Mises stress on the distal screw hole on the humeral nail with the antegrade insertion technique at ninety degrees abduction: (A) Lower gap, (B) Medium gap, (C) Upper gap, and (D) Intact condition.

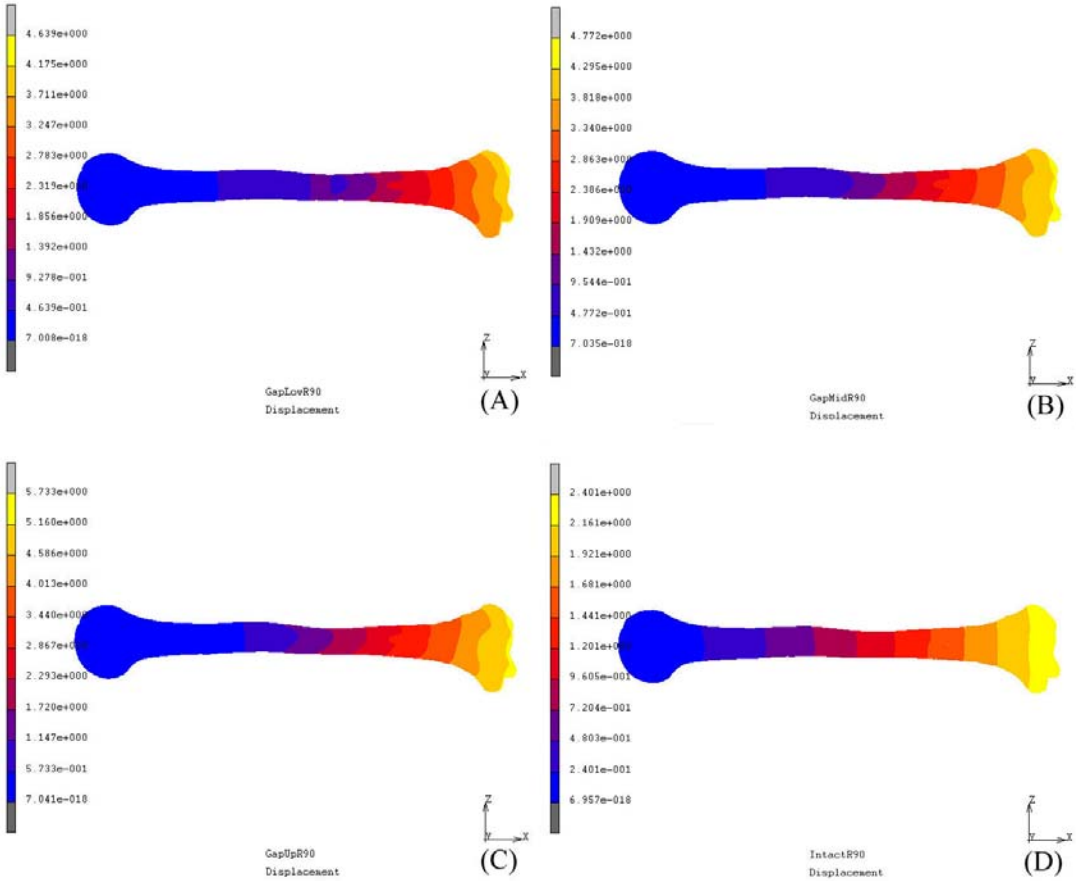

Appendix Figure 19 The displacement of the humeral bone with the retrograde insertion technique at ninety degrees abduction: (A) Lower gap, (B) Medium gap, (C) Upper gap, and (D) Intact condition.

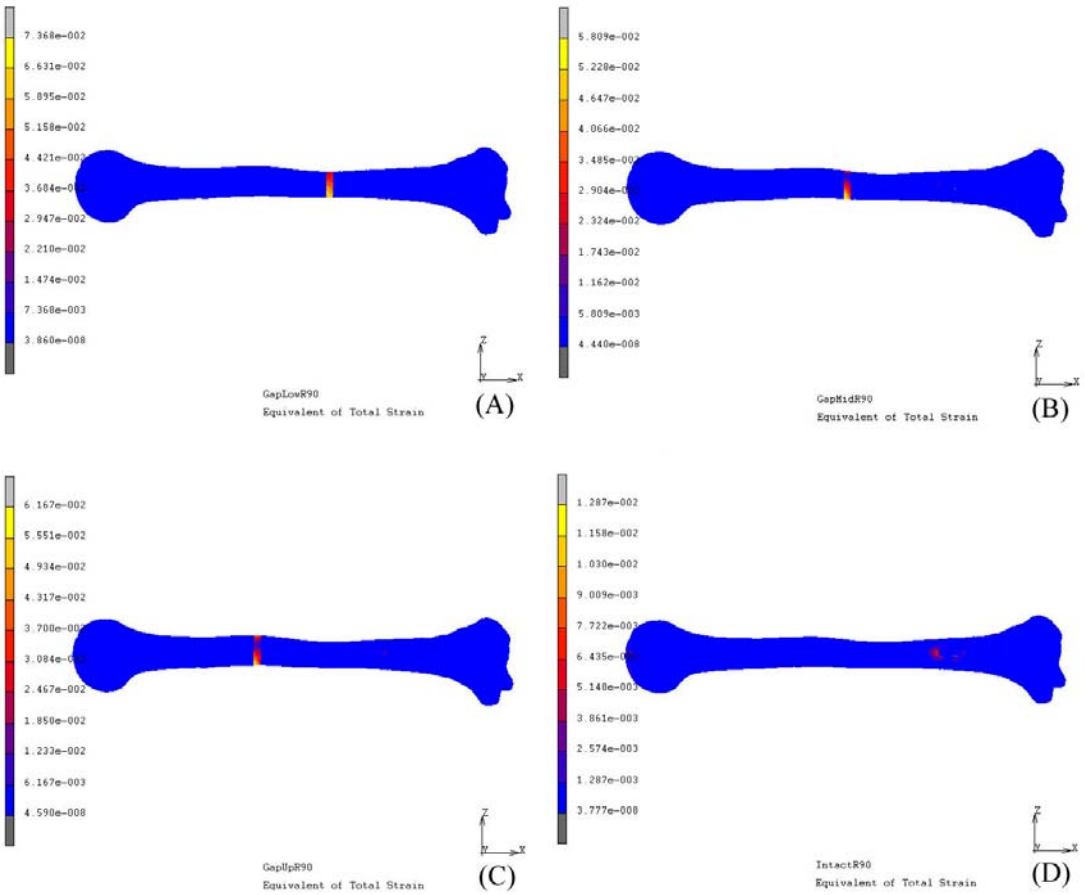

Appendix Figure 20 The total strain on the humeral bone with the retrograde insertion technique at ninety degrees abduction: (A) Lower gap, (B) Medium gap, (C) Upper gap, and (D) Intact condition.

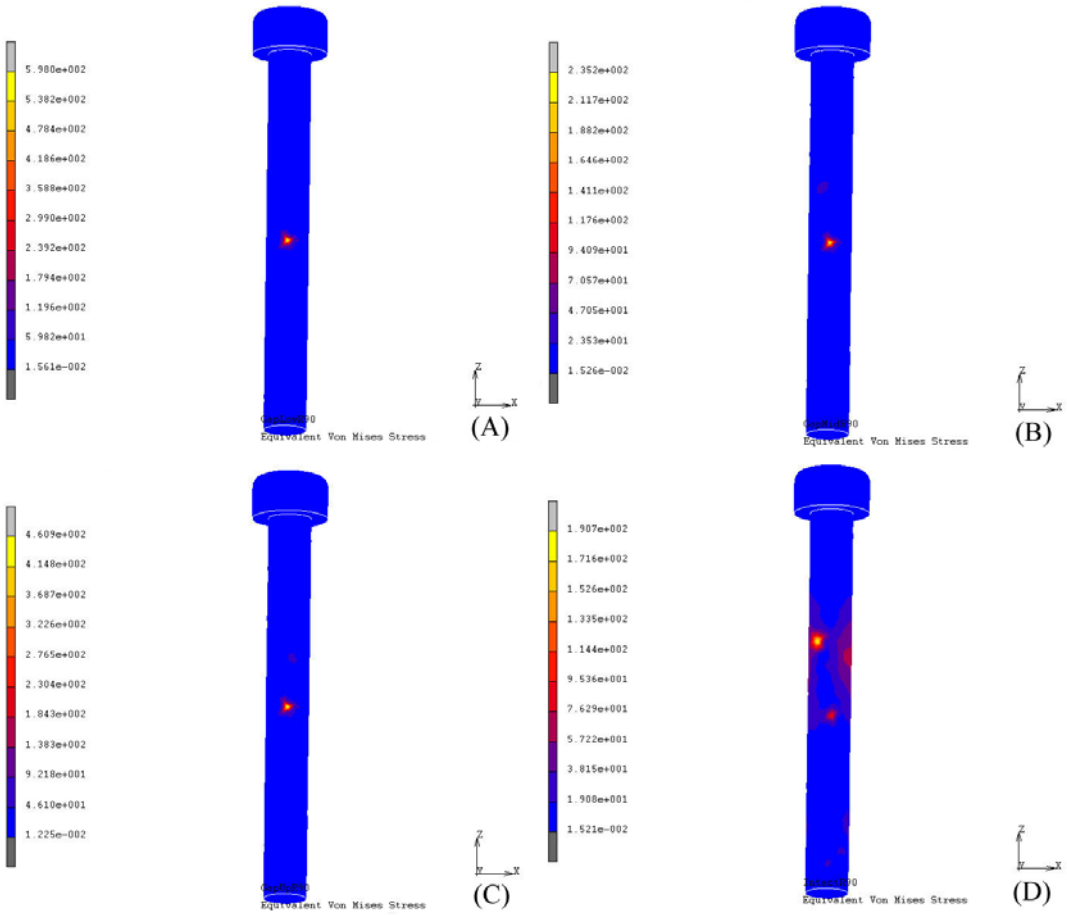

Appendix Figure 21 The von Mises stress on the proximal screw with the retrograde insertion technique at ninety degrees abduction: (A) Lower gap, (B) Medium gap, (C) Upper gap, and (D) Intact condition.

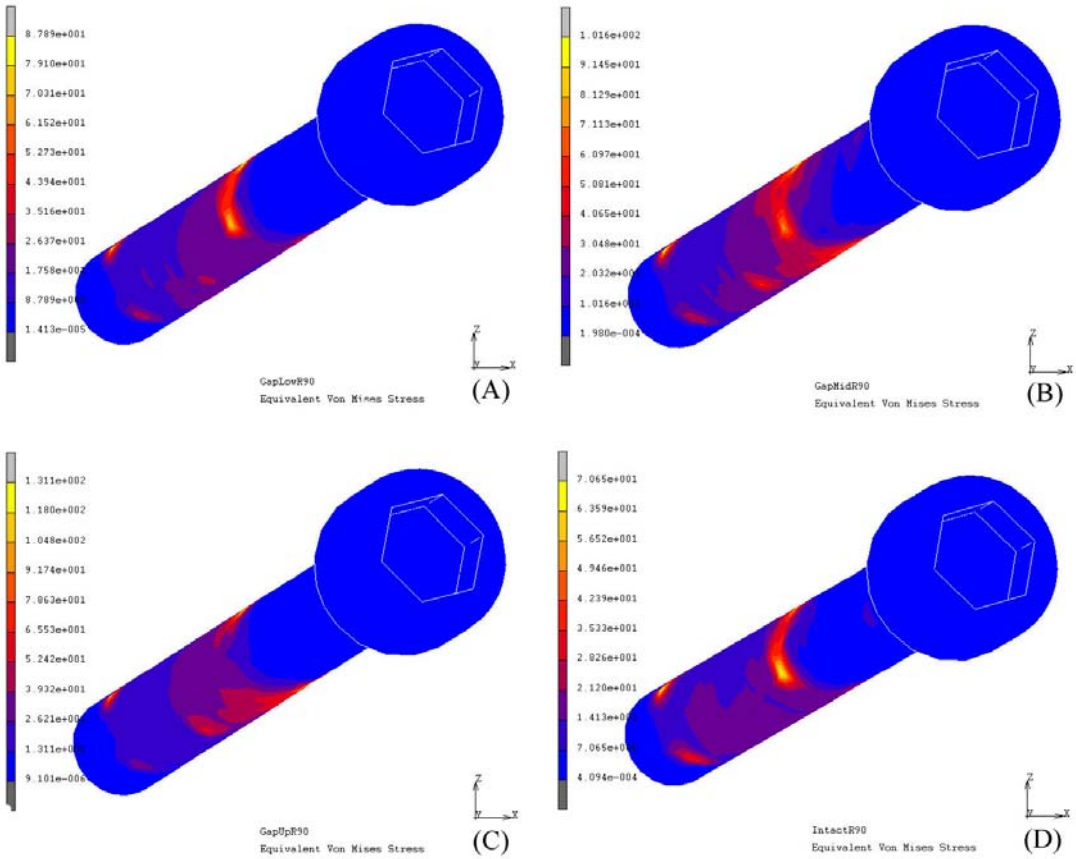

Appendix Figure 22 The von Mises stress on the distal screw with the retrograde insertion technique at ninety degrees abduction: (A) Lower gap, (B) Medium gap, (C) Upper gap, and (D) Intact condition.

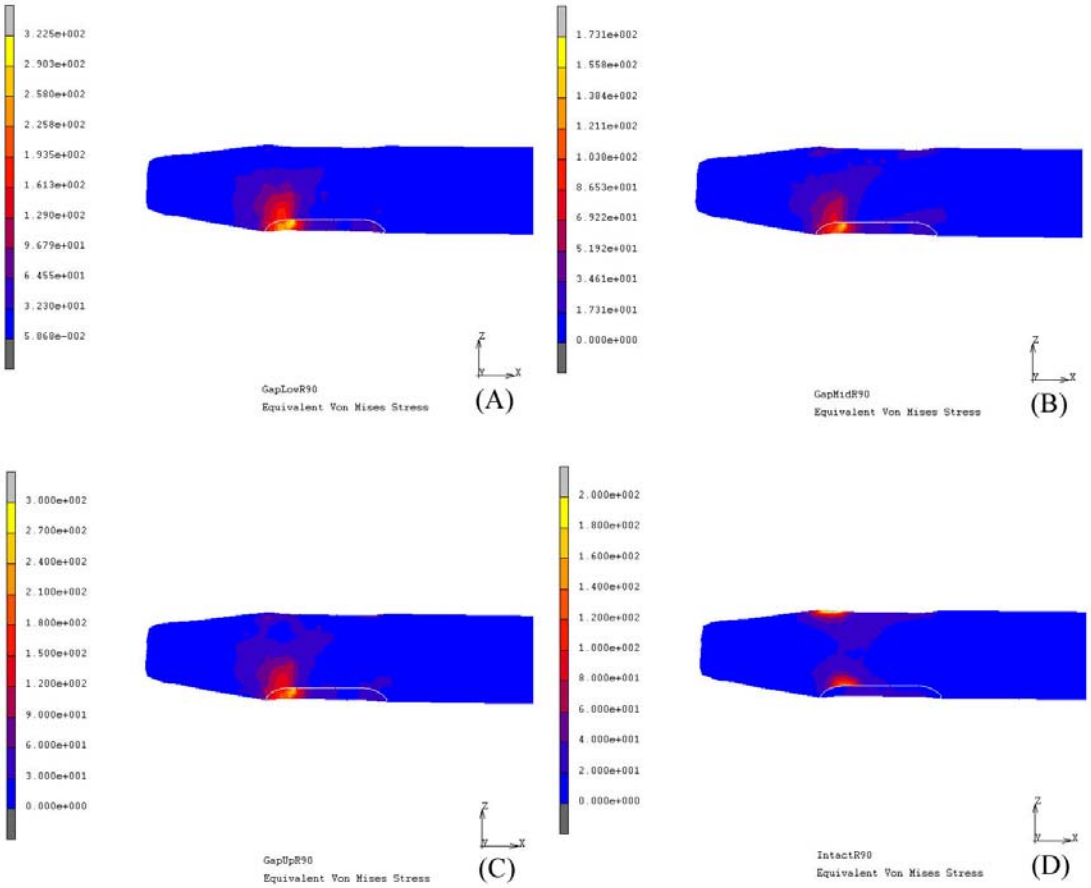

Appendix Figure 23 The von Mises stress on the proximal screw hole on the humeral nail with the retrograde insertion technique at ninety degrees abduction: (A) Lower gap, (B) Medium gap, (C) Upper gap, and (D) Intact condition.

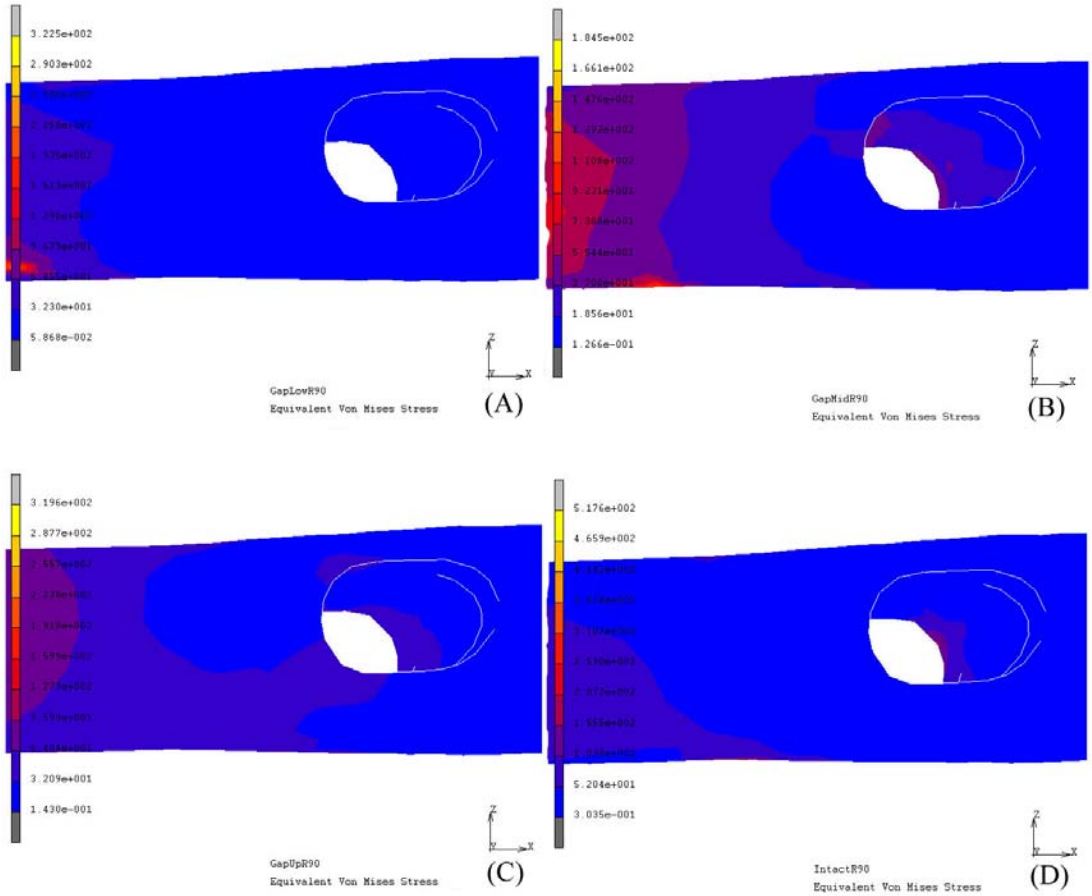

Appendix Figure 24 The von Mises stress on the distal screw hole on the humeral nail with the retrograde insertion technique at ninety degrees abduction: (A) Lower gap, (B) Medium gap, (C) Upper gap, and (D) Intact condition.

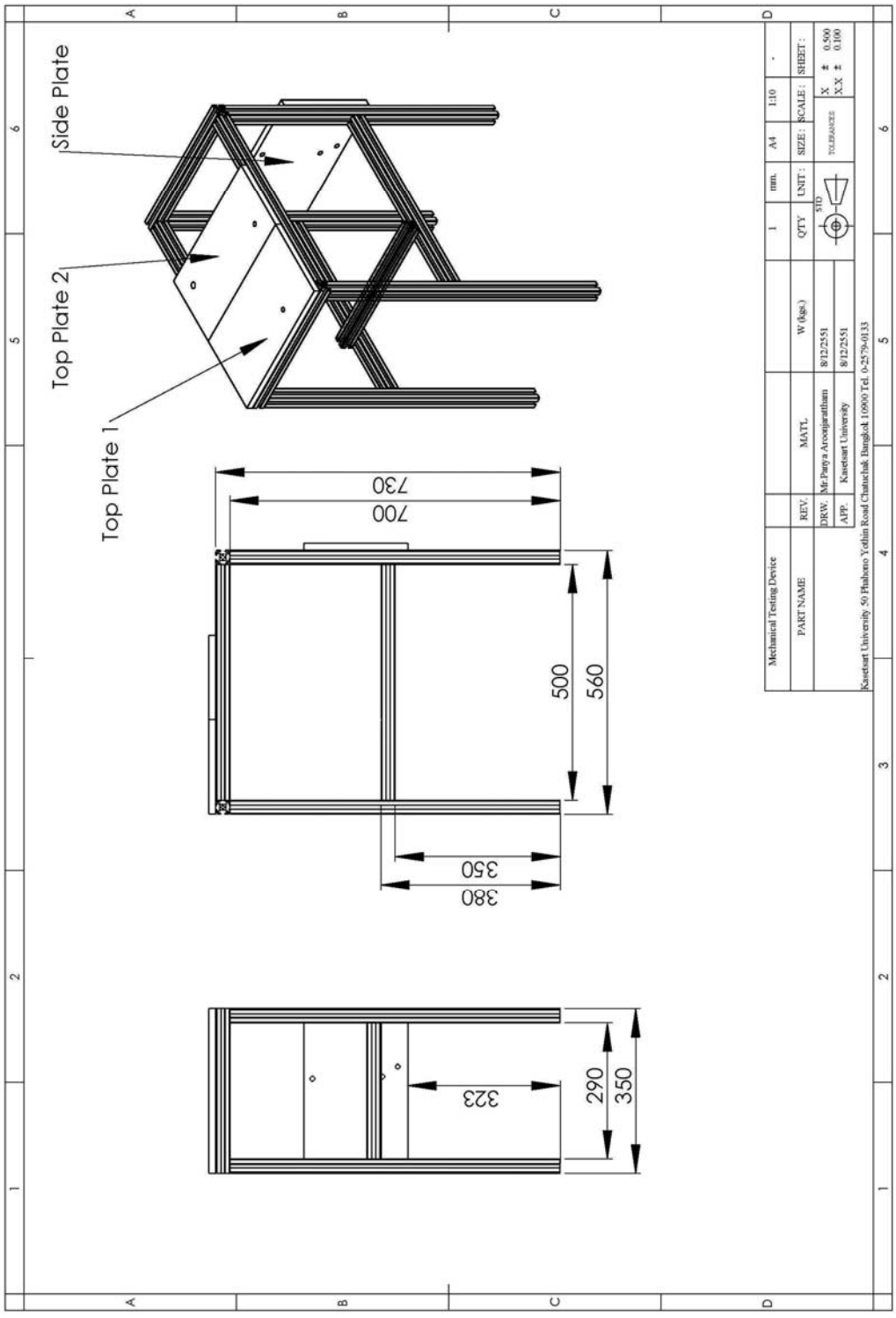

Appendix Figure 25 The dimensions of the mechanical testing device.

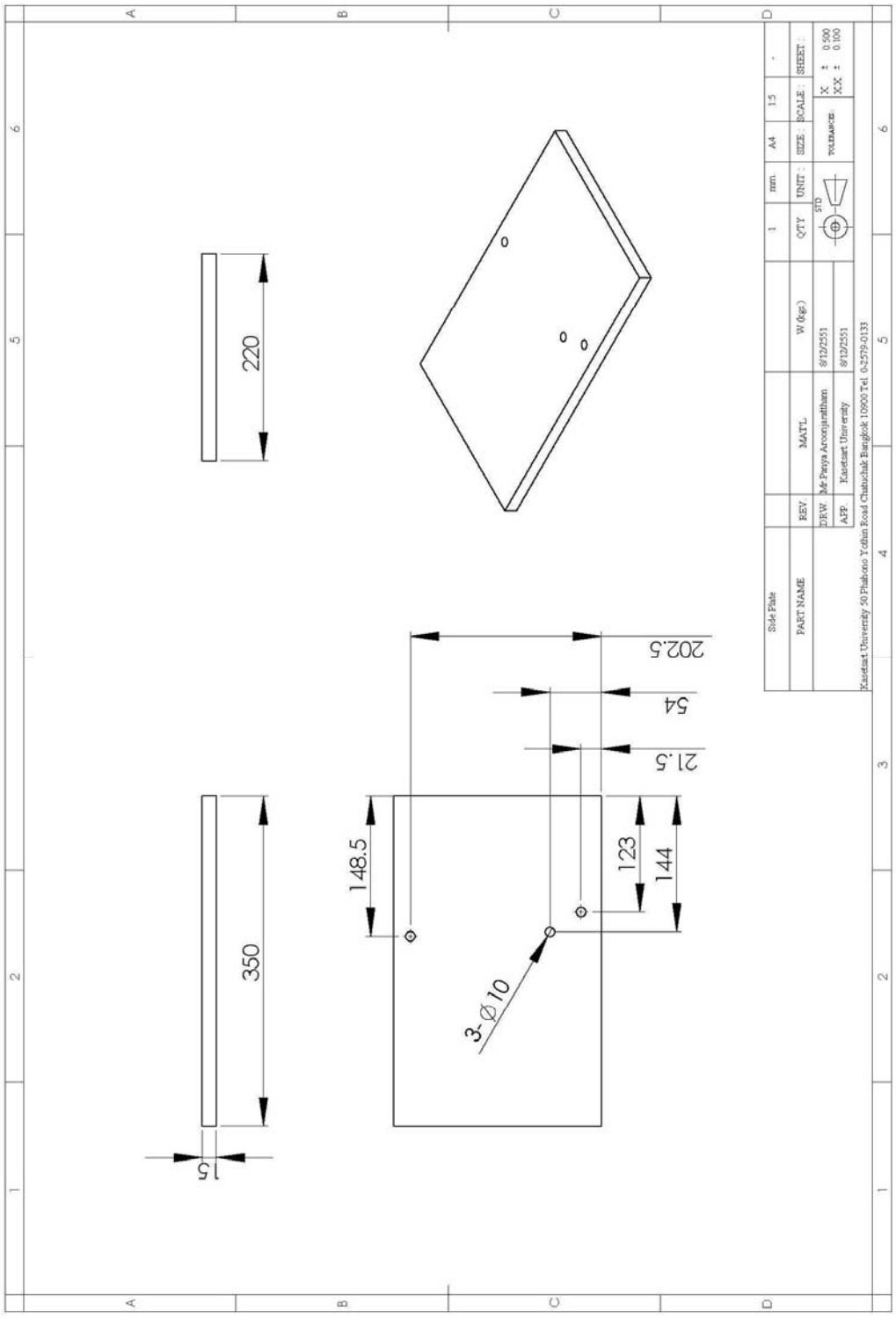

Appendix Figure 26 The dimensions of the side plate.

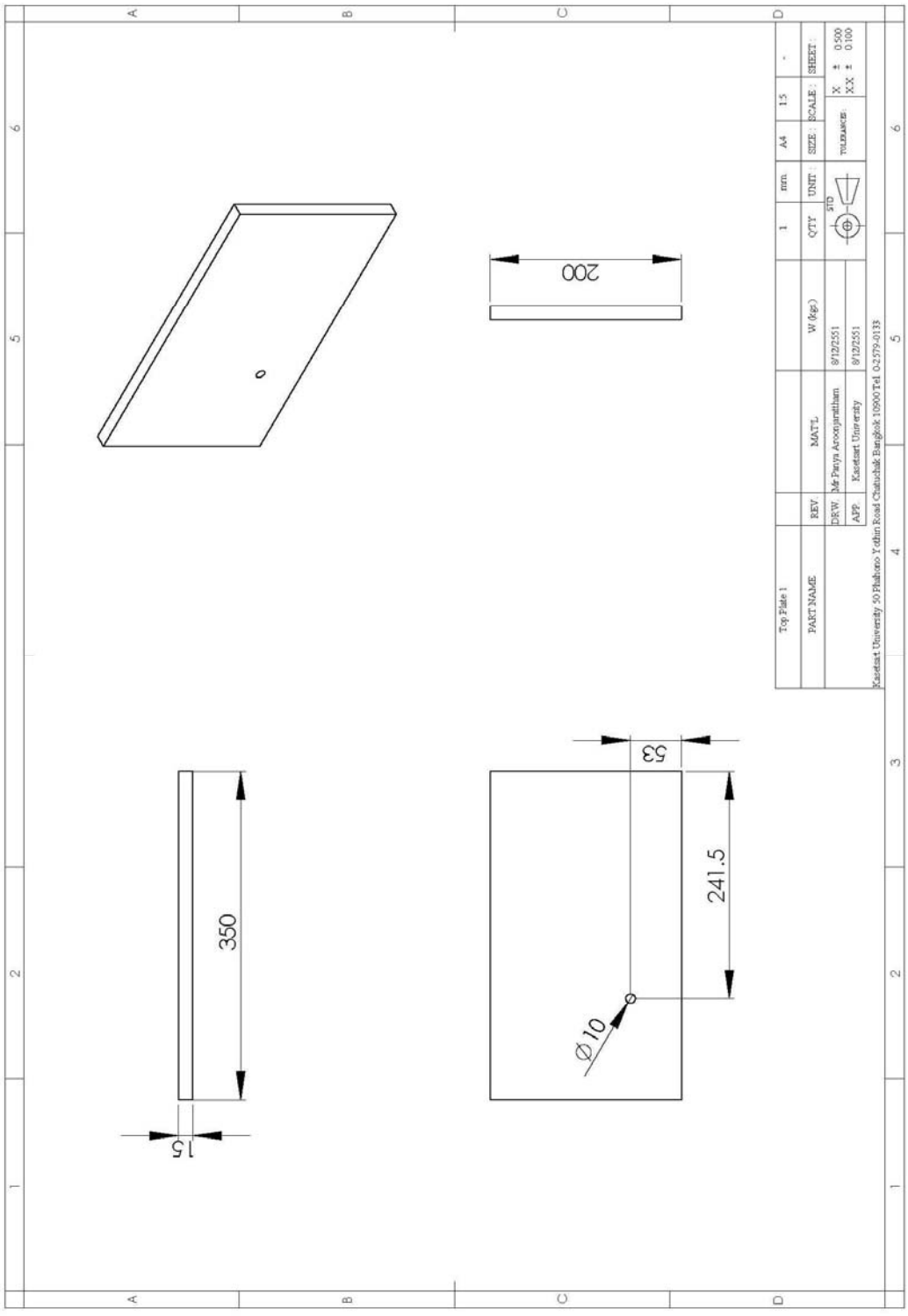

Appendix Figure 27 The dimensions of top plate 1.

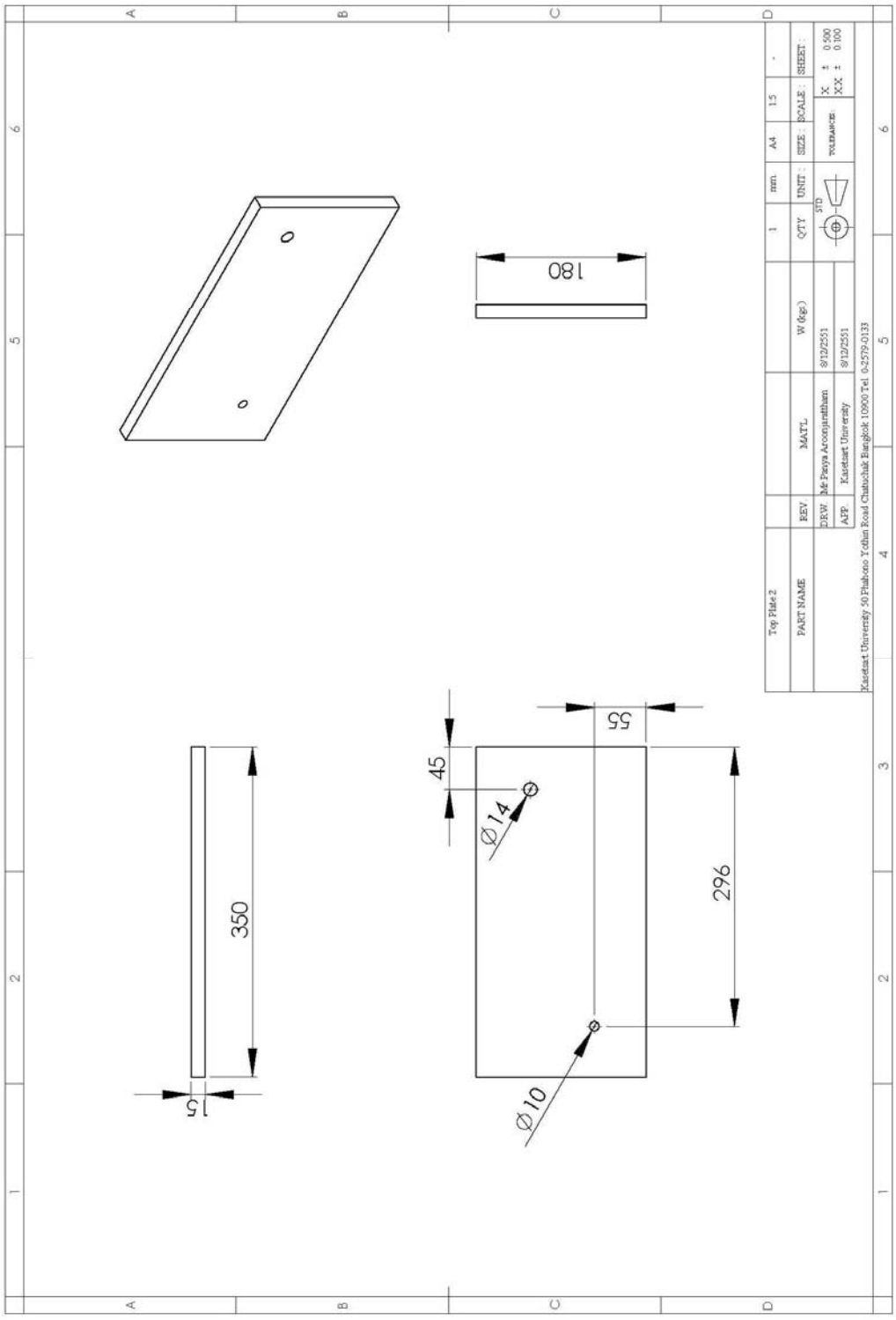

Appendix Figure 28 The dimensions of top plate 2.

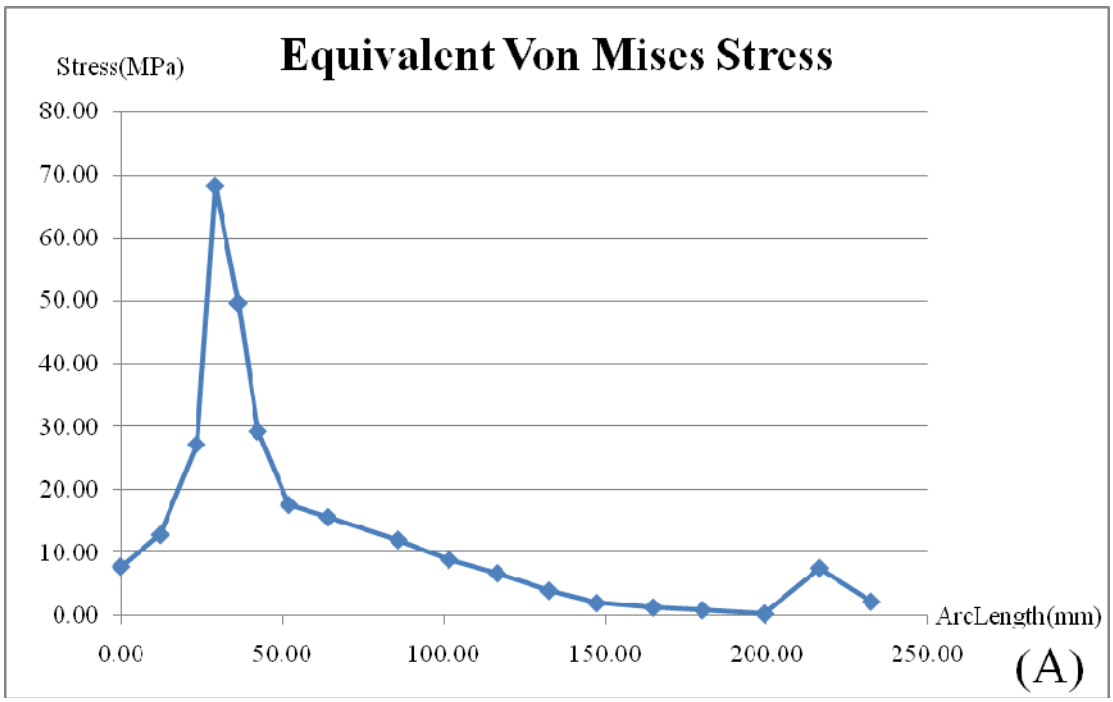

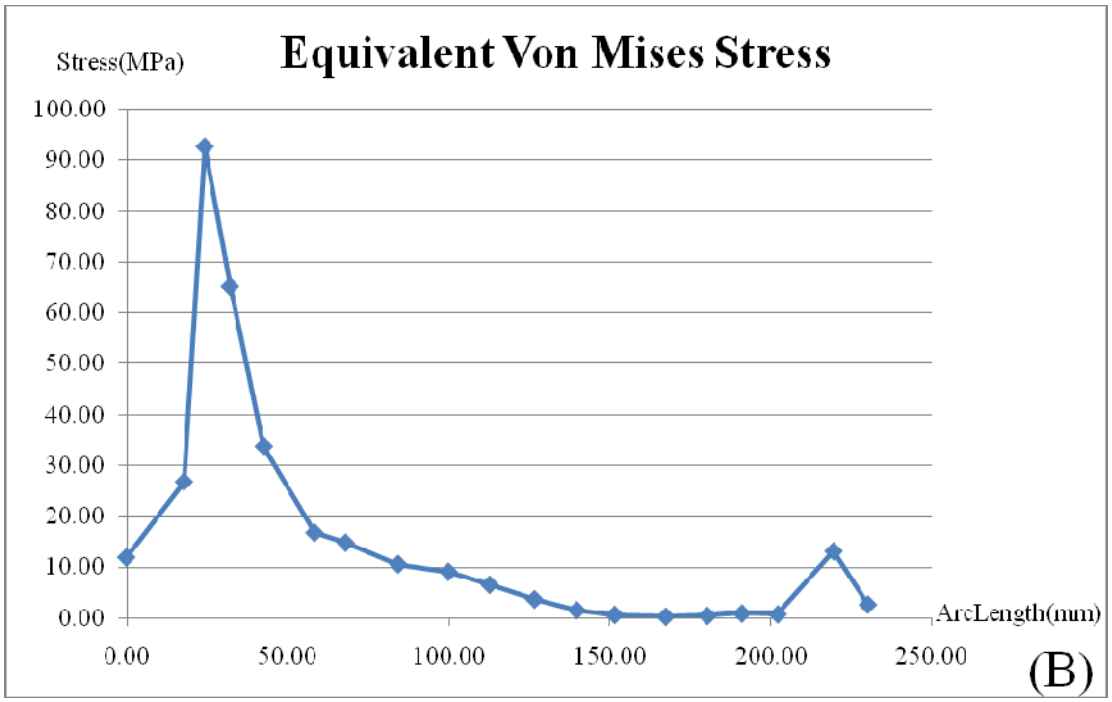

Appendix Figure 29 The Von Mises stress distribution on the standard humeral nail with the antegrade insertion technique and lower gap at zero degrees abduction: (A) Medial side, and (B) Lateral side.

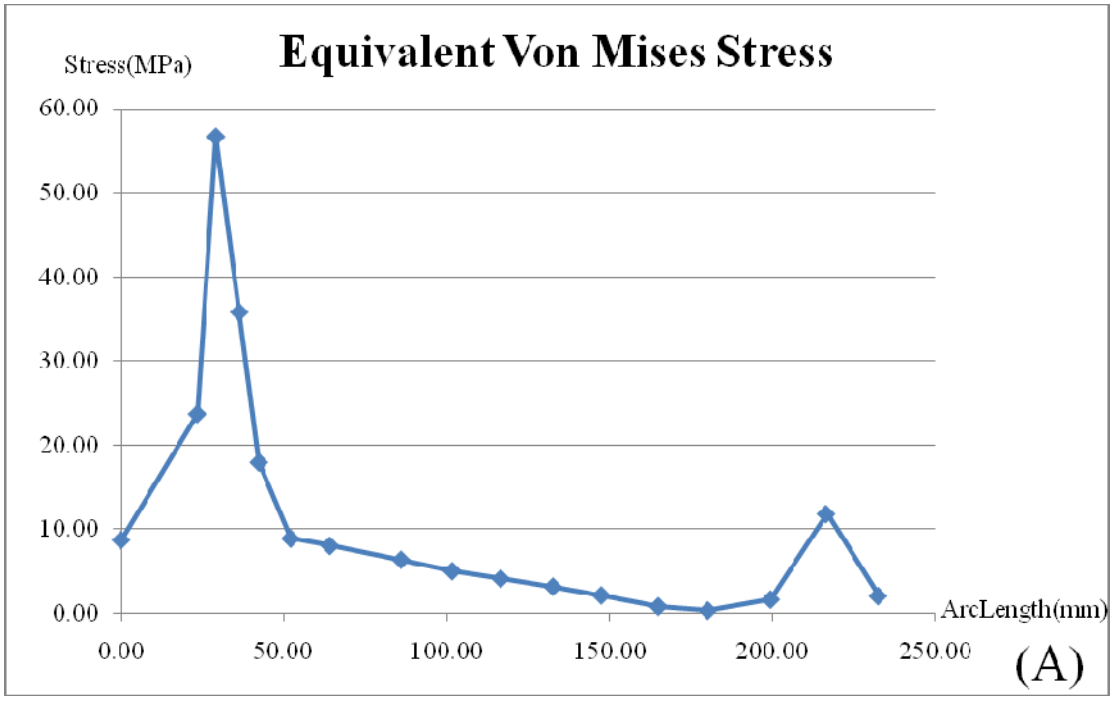

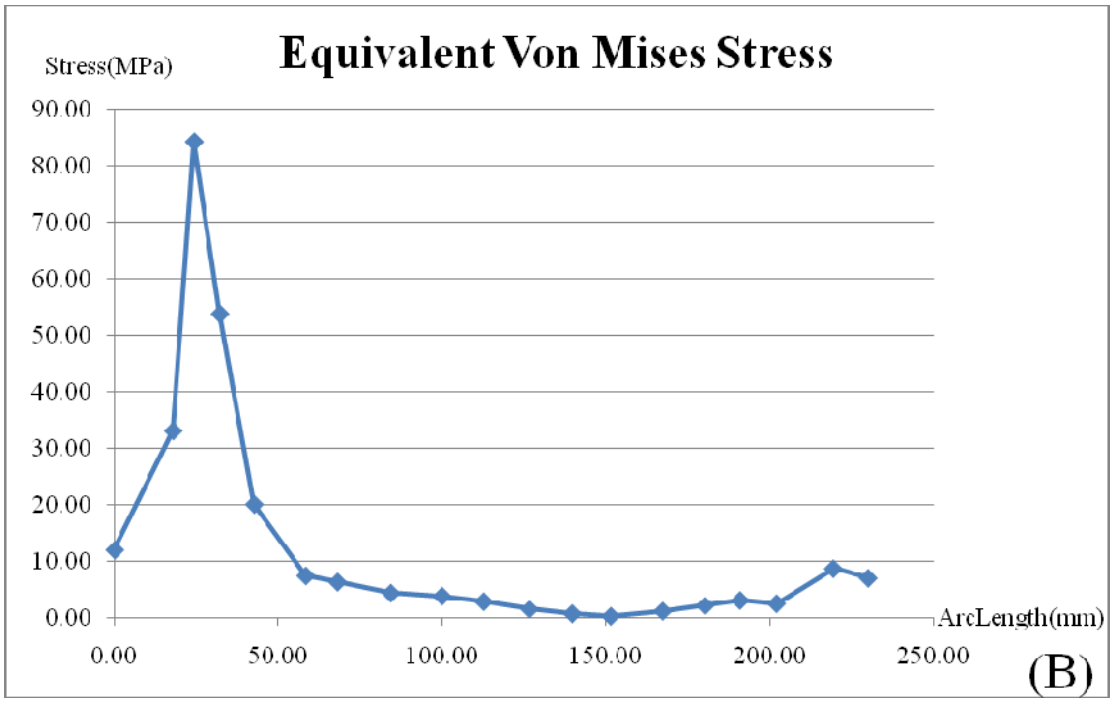

Appendix Figure 30 The Von Mises stress distribution on the standard humeral nail with the antegrade insertion technique and medium gap at zero degrees abduction: (A) Medial side, and (B) Lateral side.

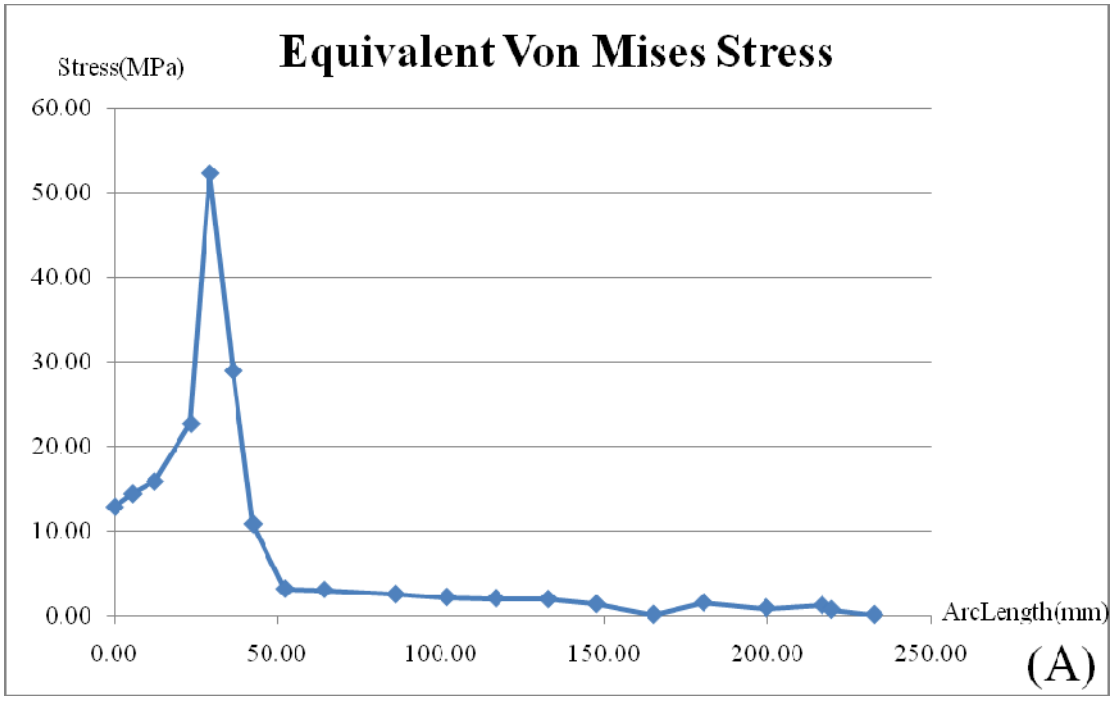

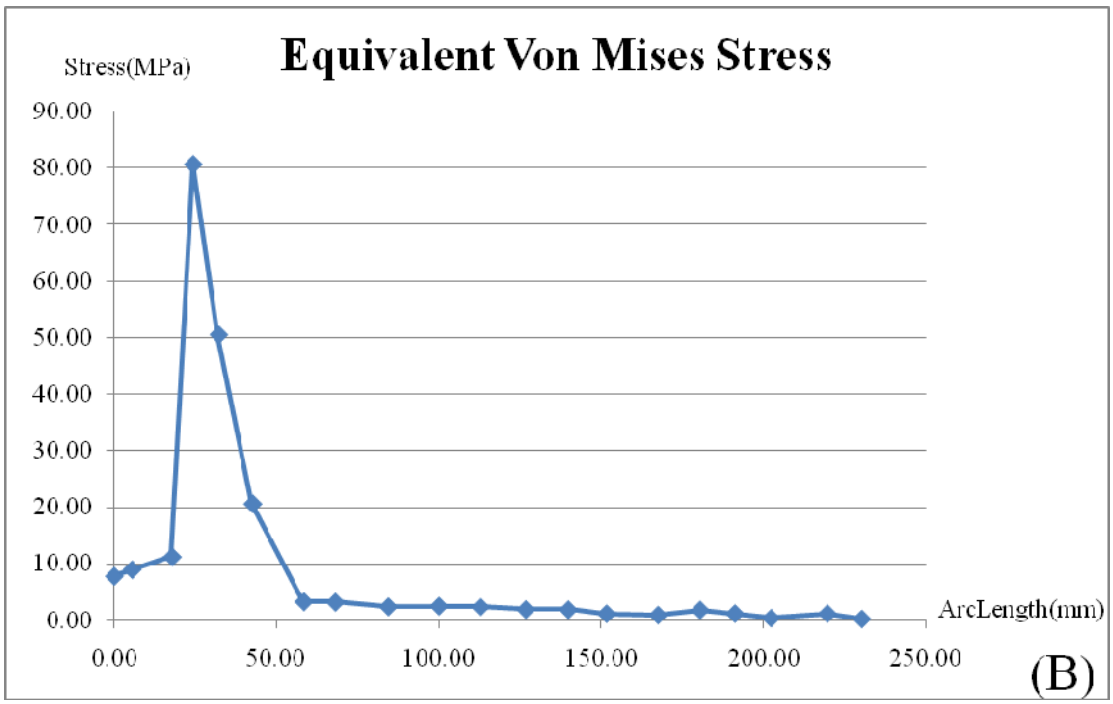

Appendix Figure 31 The Von Mises stress distribution on the standard humeral nail with the antegrade insertion technique and upper gap at zero degrees abduction: (A) Medial side, and (B) Lateral side.

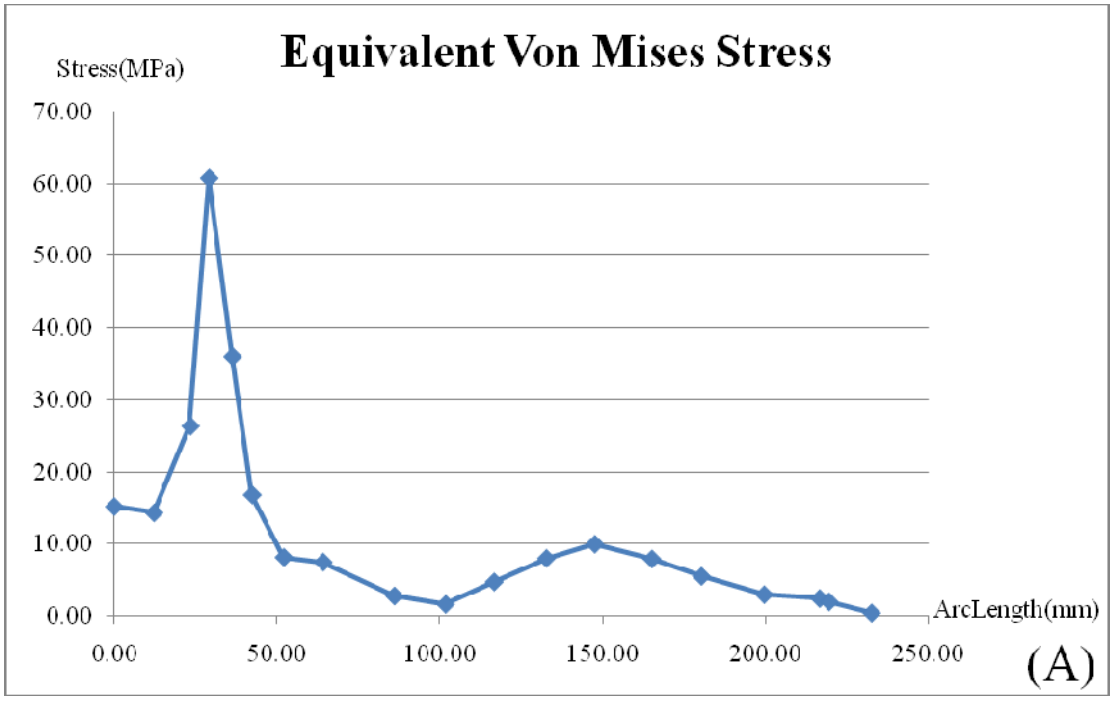

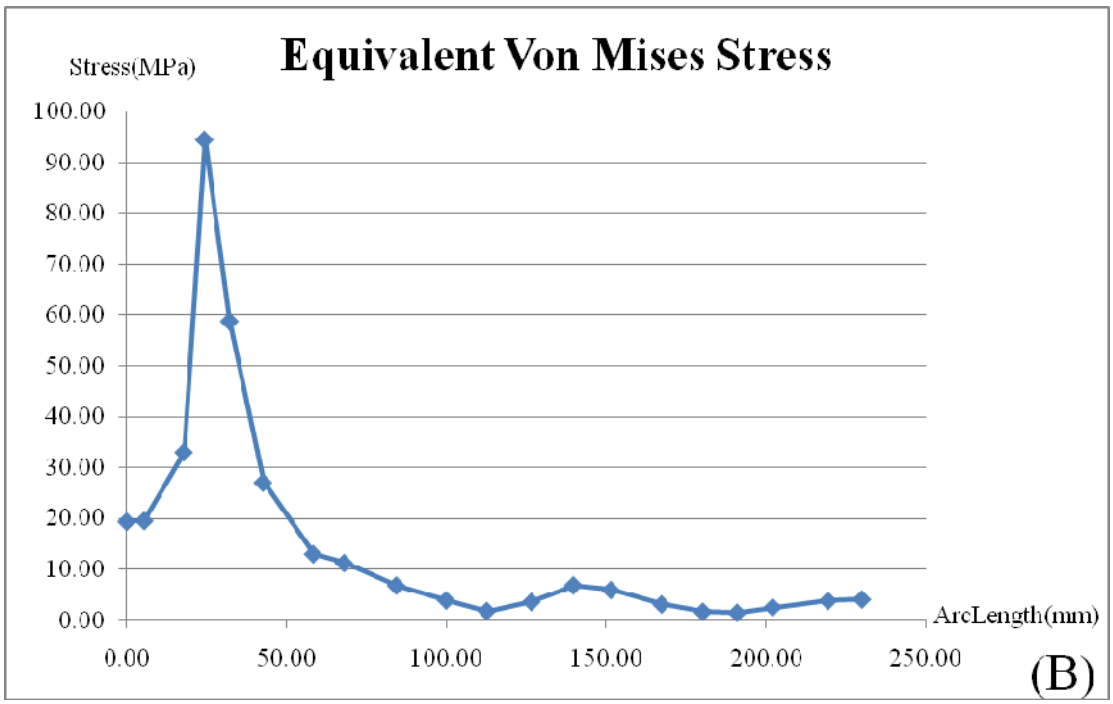

Appendix Figure 32 The Von Mises stress distribution on the standard humeral nail with the antegrade insertion technique and intact at zero degrees abduction: (A) Medial side, and (B) Lateral side.

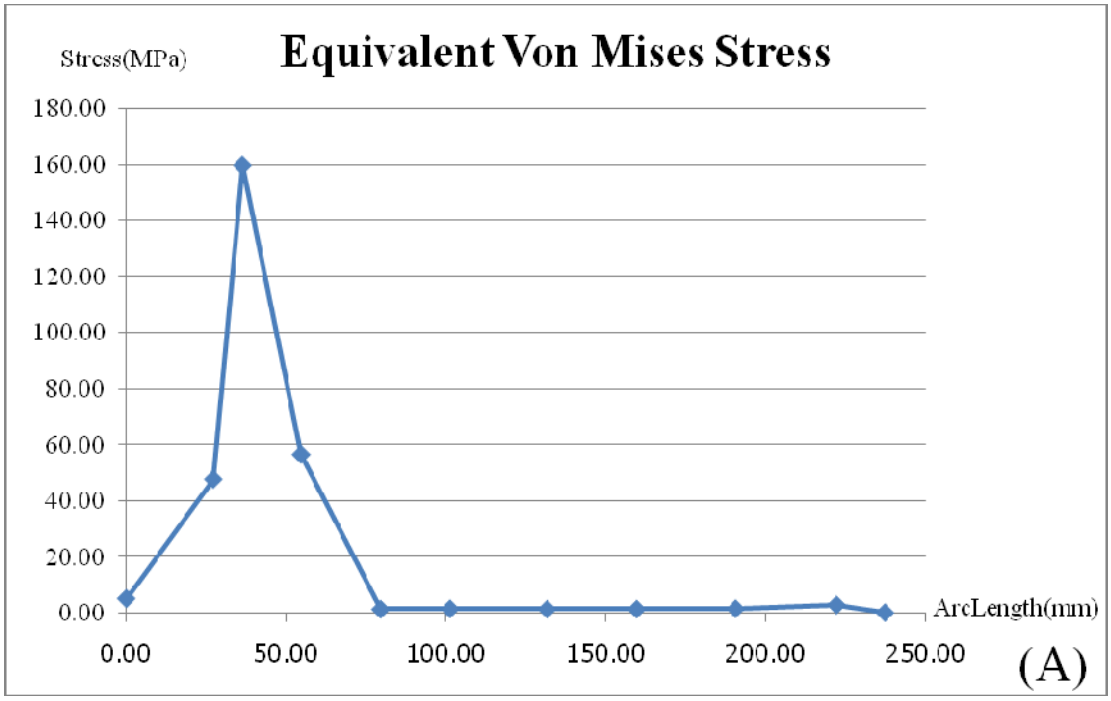

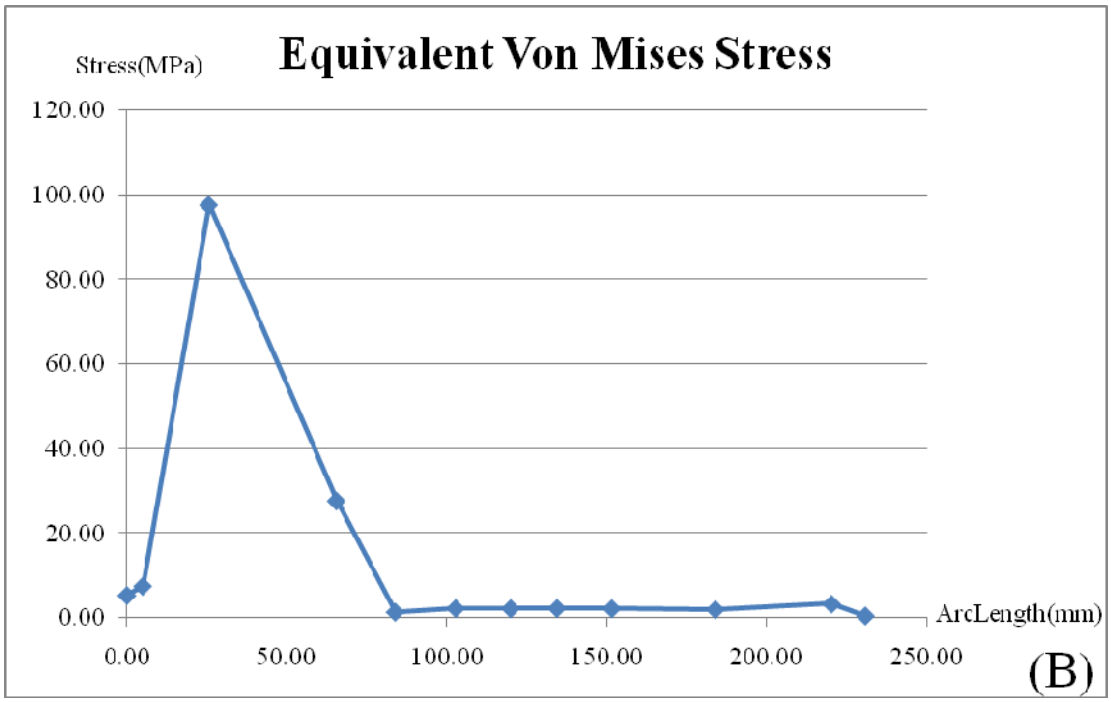

Appendix Figure 33 The Von Mises stress distribution on the standard humeral nail with the retrograde insertion technique and lower gap at zero degrees abduction: (A) Medial side, and (B) Lateral side.

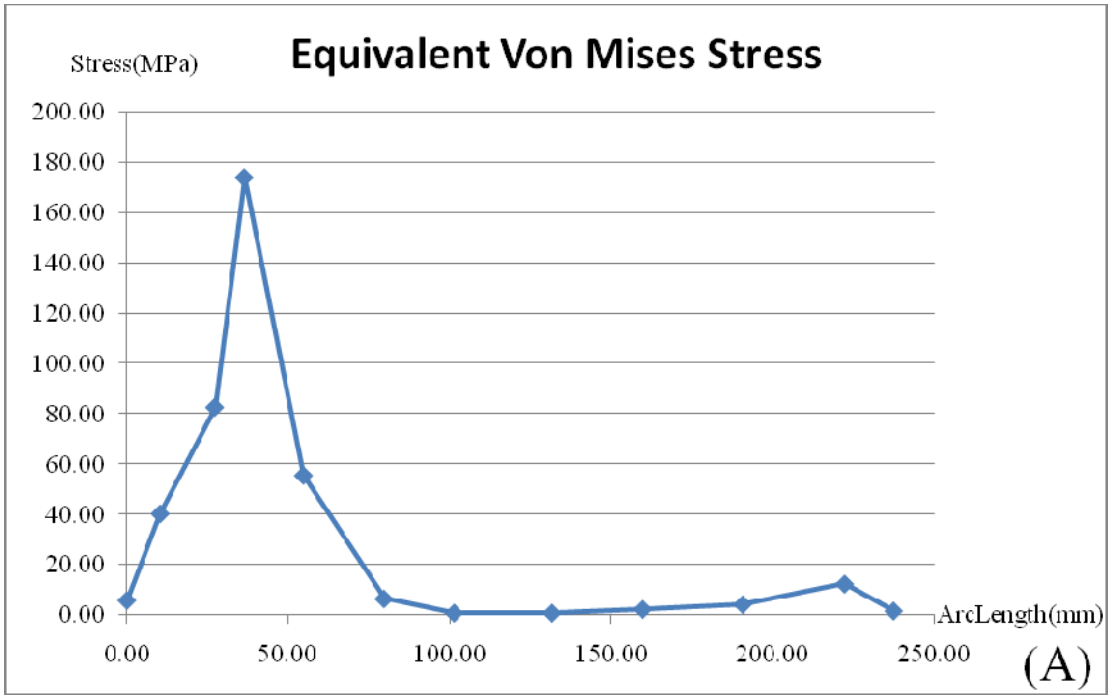

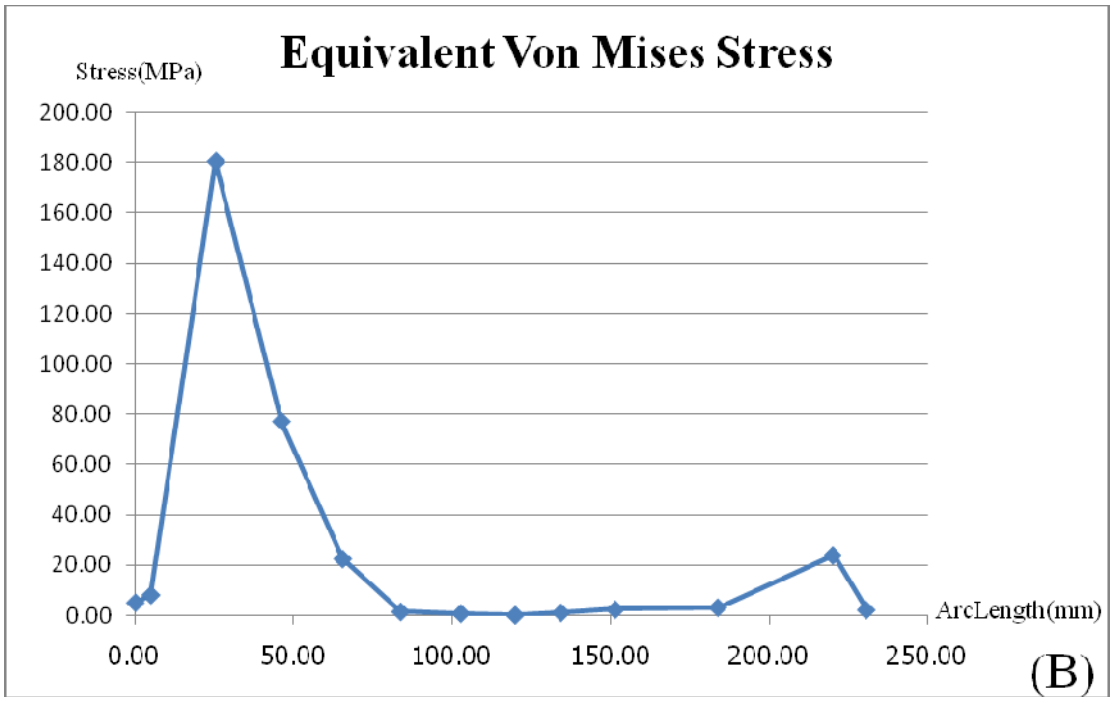

Appendix Figure 34 The Von Mises stress distribution on the standard humeral nail with the retrograde insertion technique and medium gap at zero degrees abduction: (A) Medial side, and (B) Lateral side.

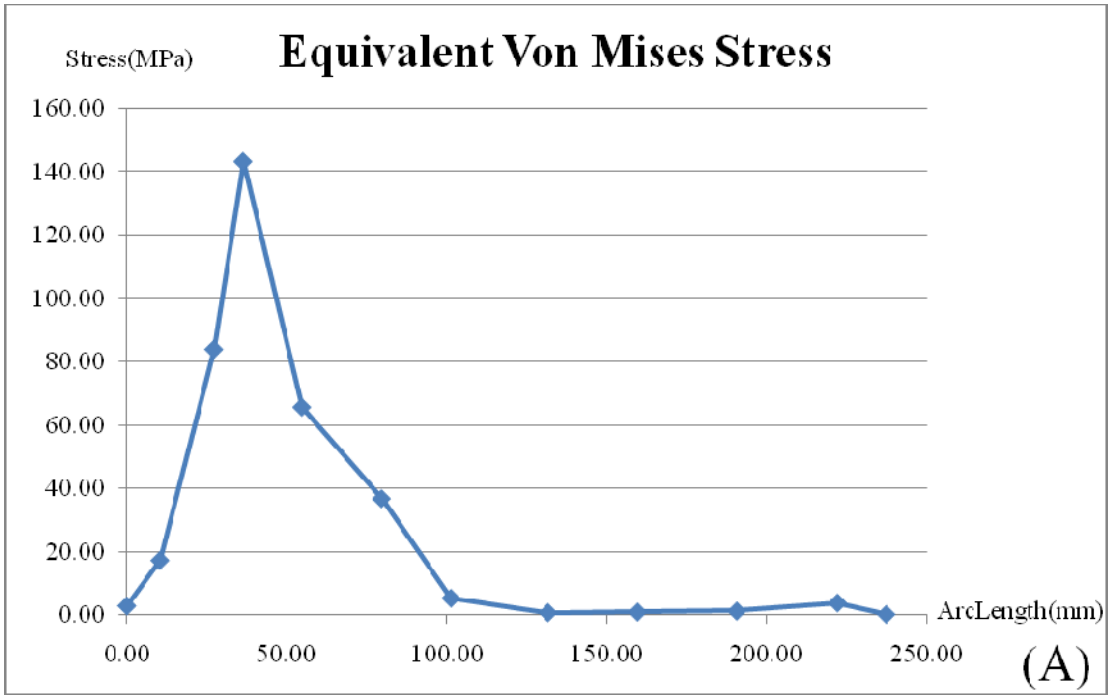

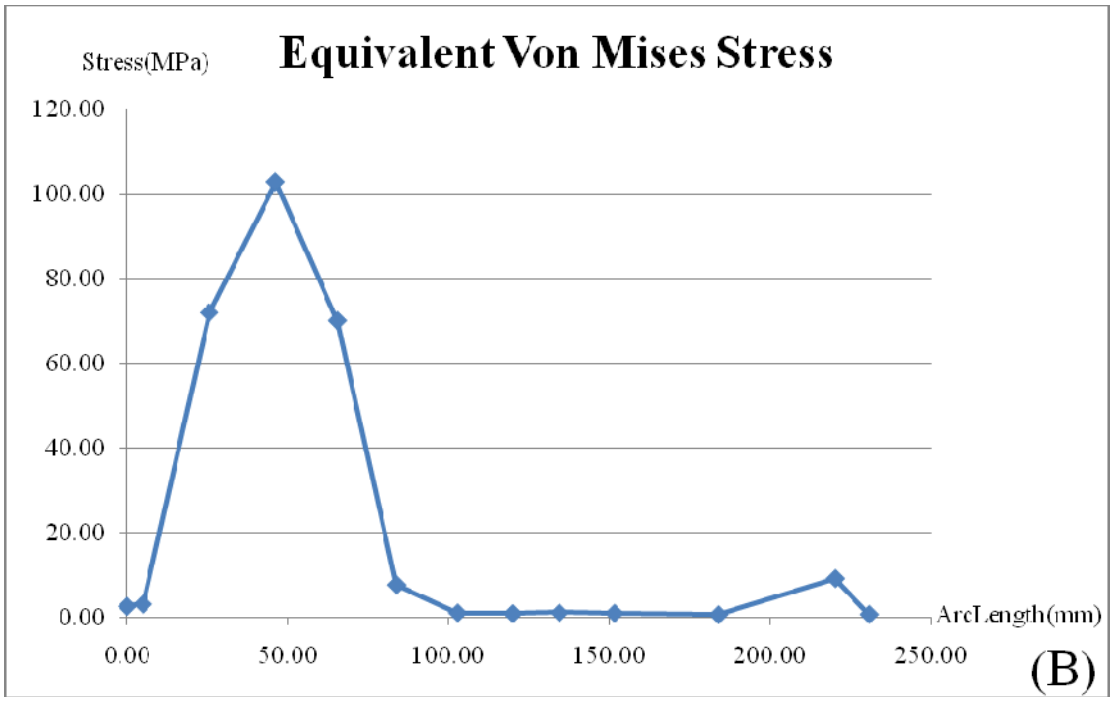

Appendix Figure 35 The Von Mises stress distribution on the standard humeral nail with the retrograde insertion technique and upper gap at zero degrees abduction: (A) Medial side, and (B) Lateral side.

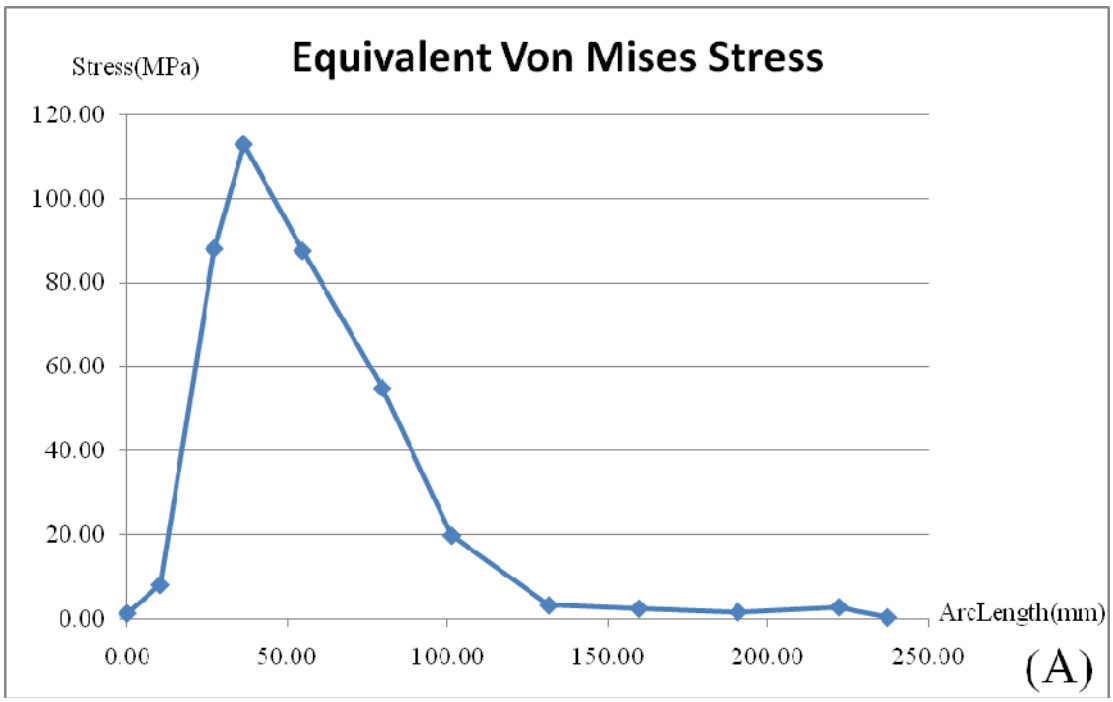

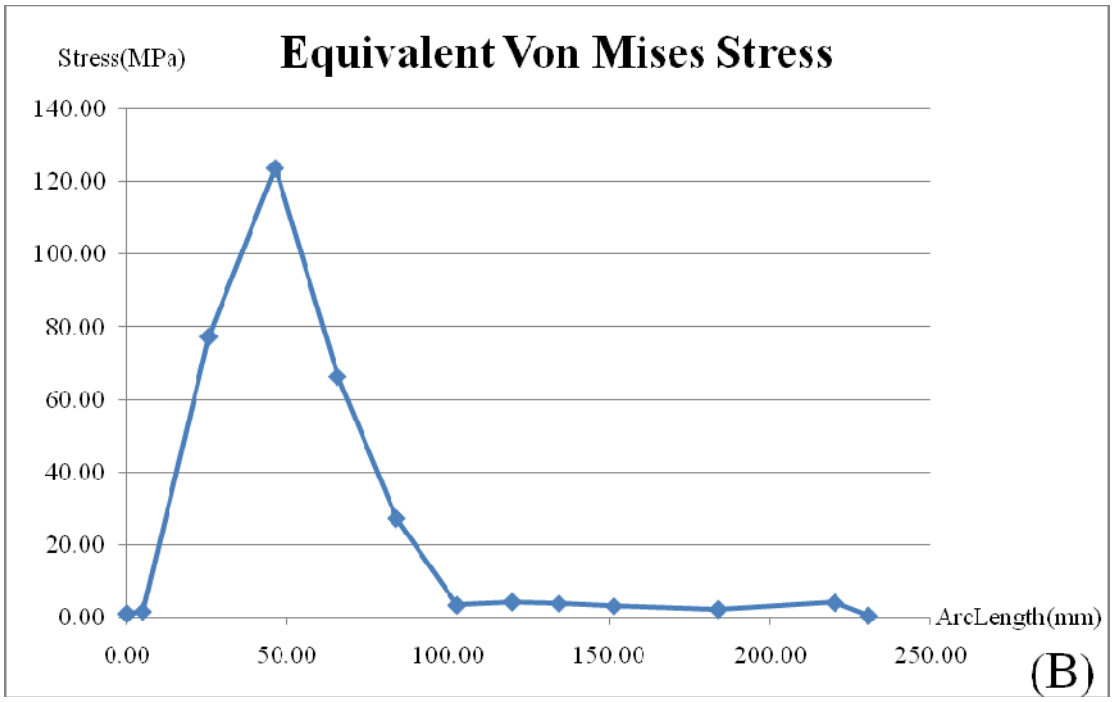

Appendix Figure 36 The Von Mises stress distribution on the standard humeral nail with the retrograde insertion technique and intact at zero degrees abduction: (A) Medial side, and (B) Lateral side.

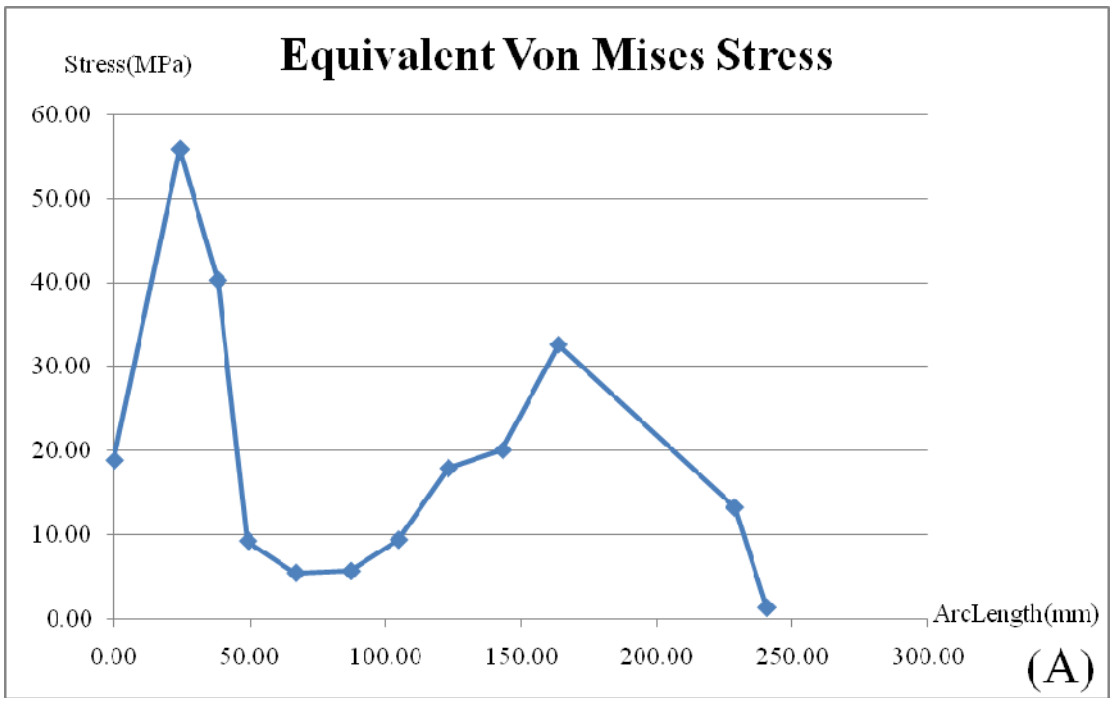

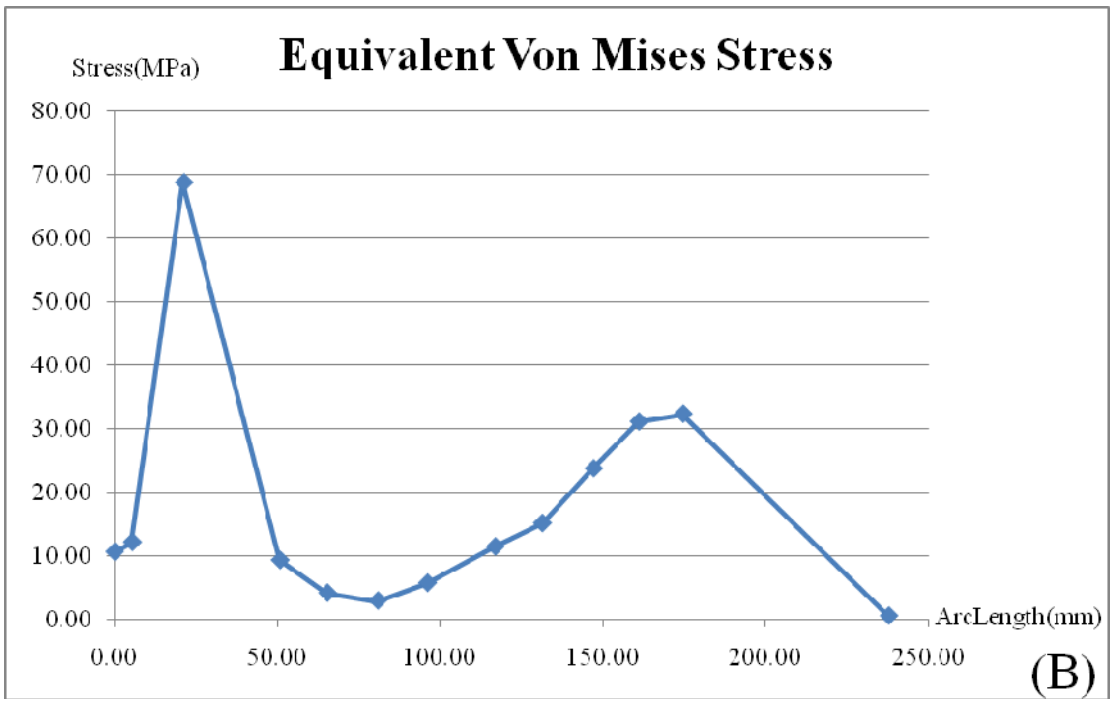

Appendix Figure 37 The Von Mises stress distribution on the standard humeral nail with the antegrade insertion technique and lower gap at ninety degrees abduction: (A) Medial side, and (B) Lateral side.

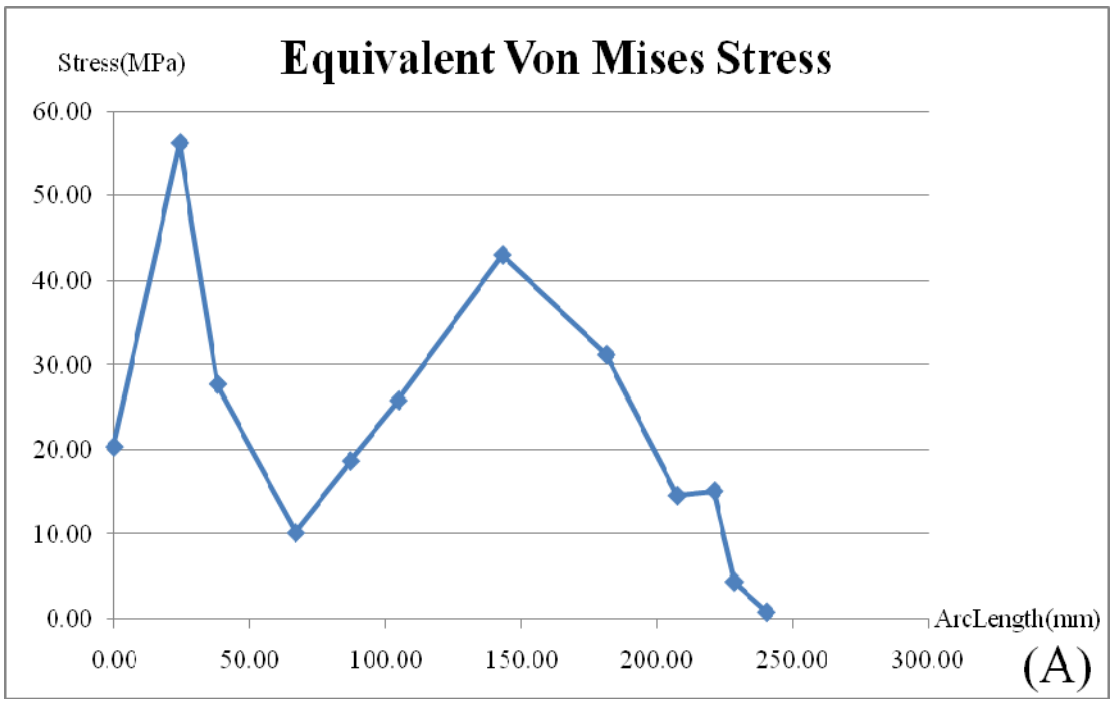

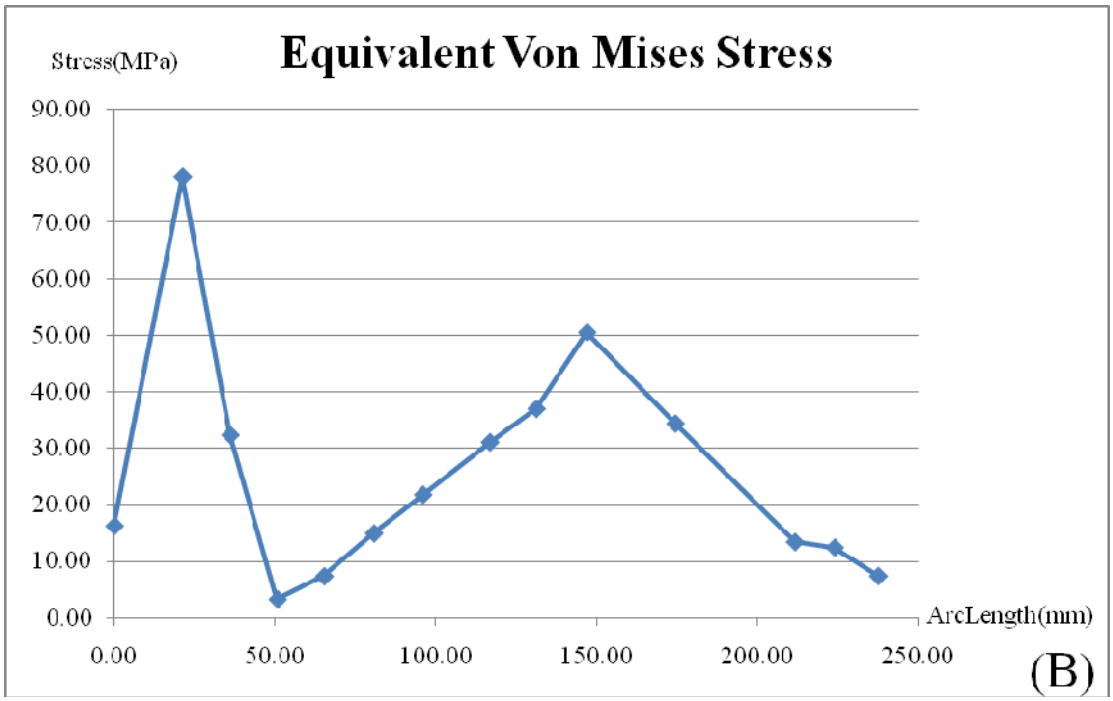

Appendix Figure 38 The Von Mises stress distribution on the standard humeral nail with the antegrade insertion technique and medium gap at ninety degrees abduction: (A) Medial side, and (B) Lateral side.

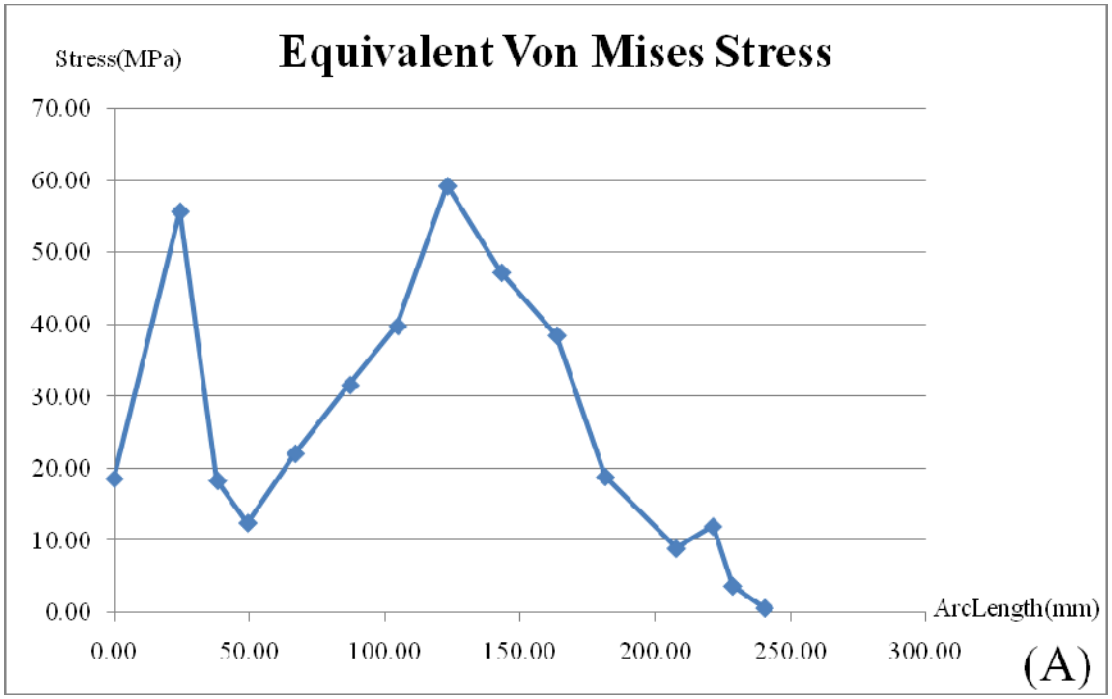

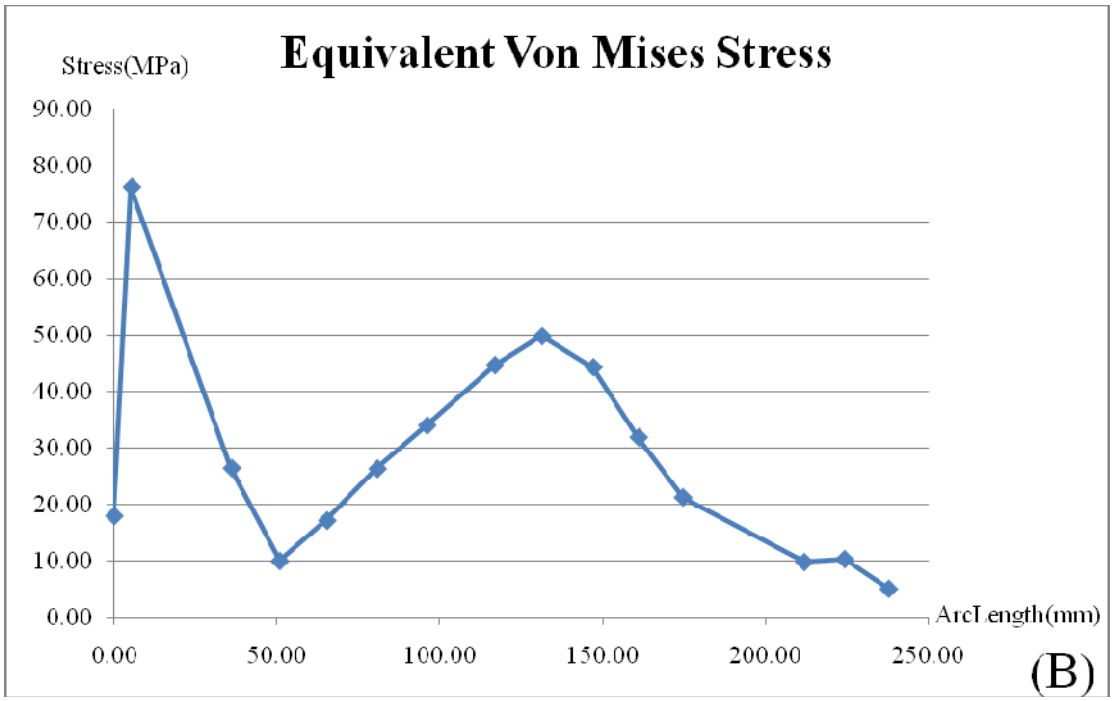

Appendix Figure 39 The Von Mises stress distribution on the standard humeral nail with the antegrade insertion technique and upper gap at ninety degrees abduction: (A) Medial side, and (B) Lateral side.

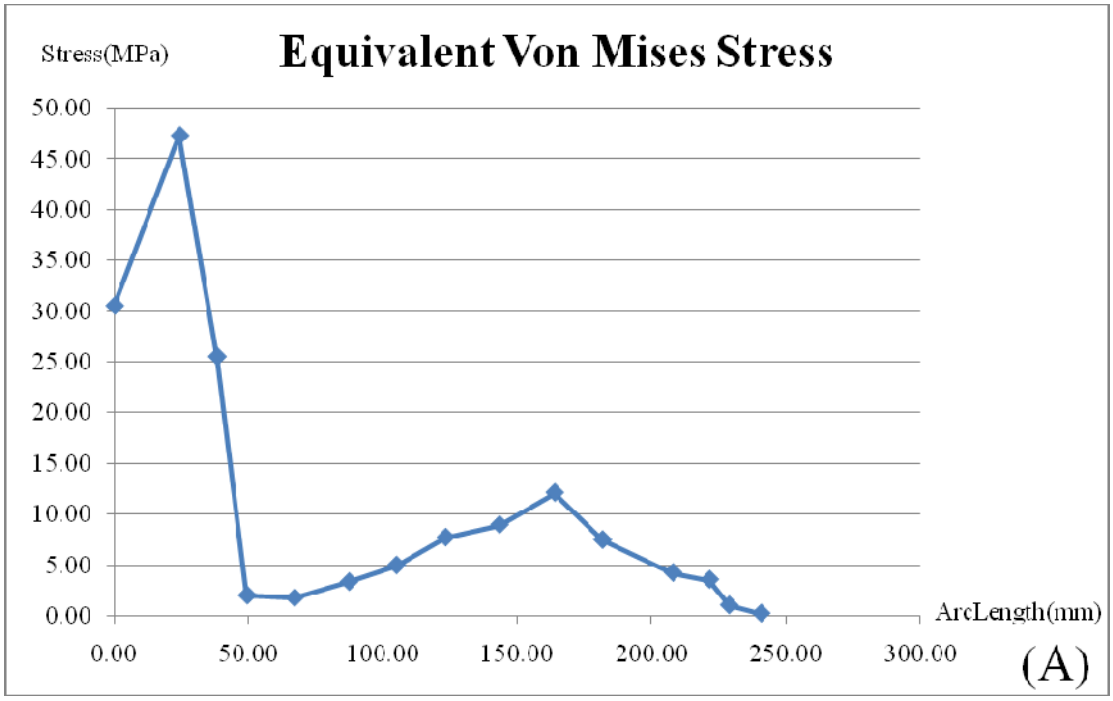

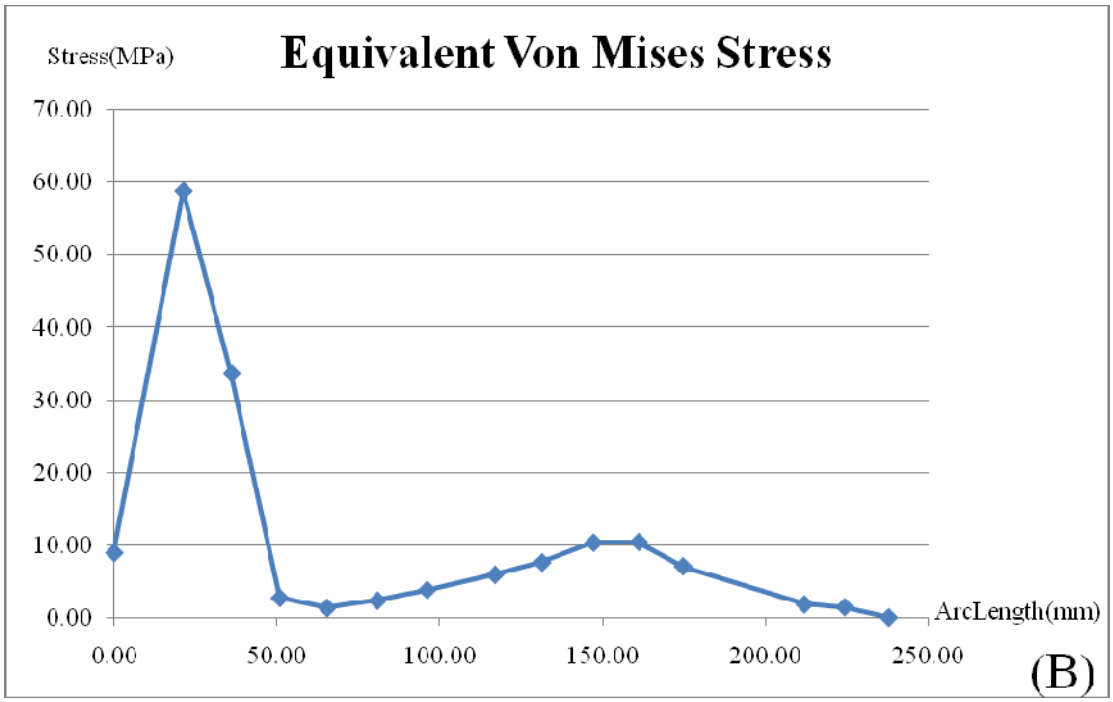

Appendix Figure 40 The Von Mises stress distribution on the standard humeral nail with the antegrade insertion technique and intact at ninety degrees abduction: (A) Medial side, and (B) Lateral side.

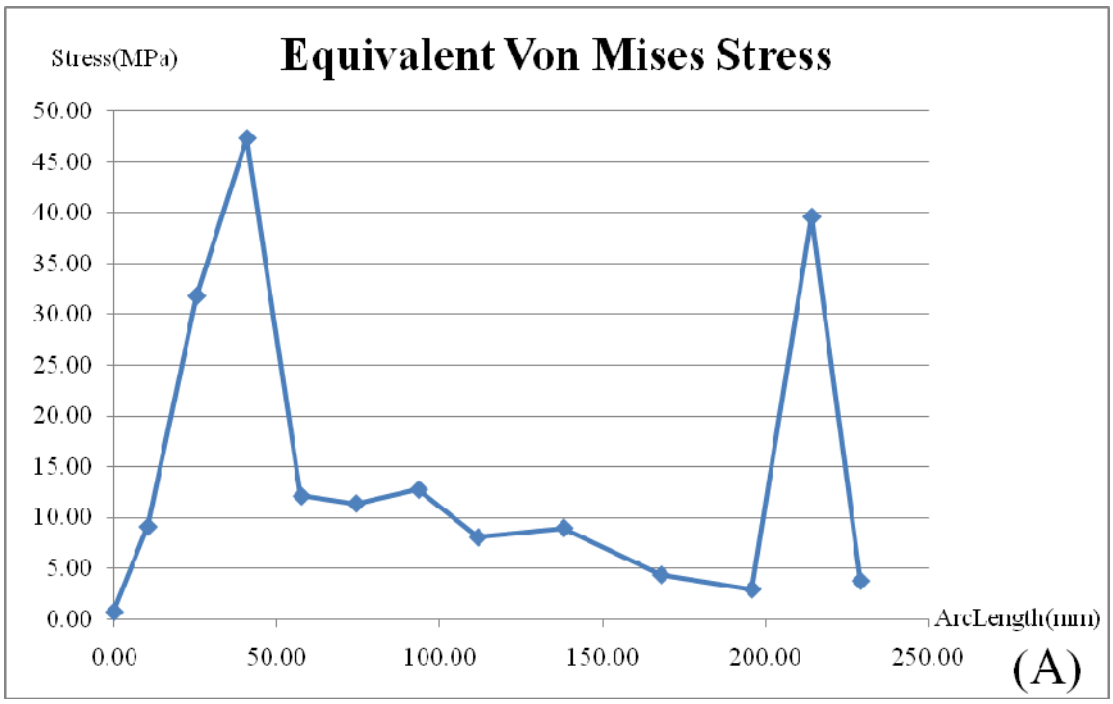

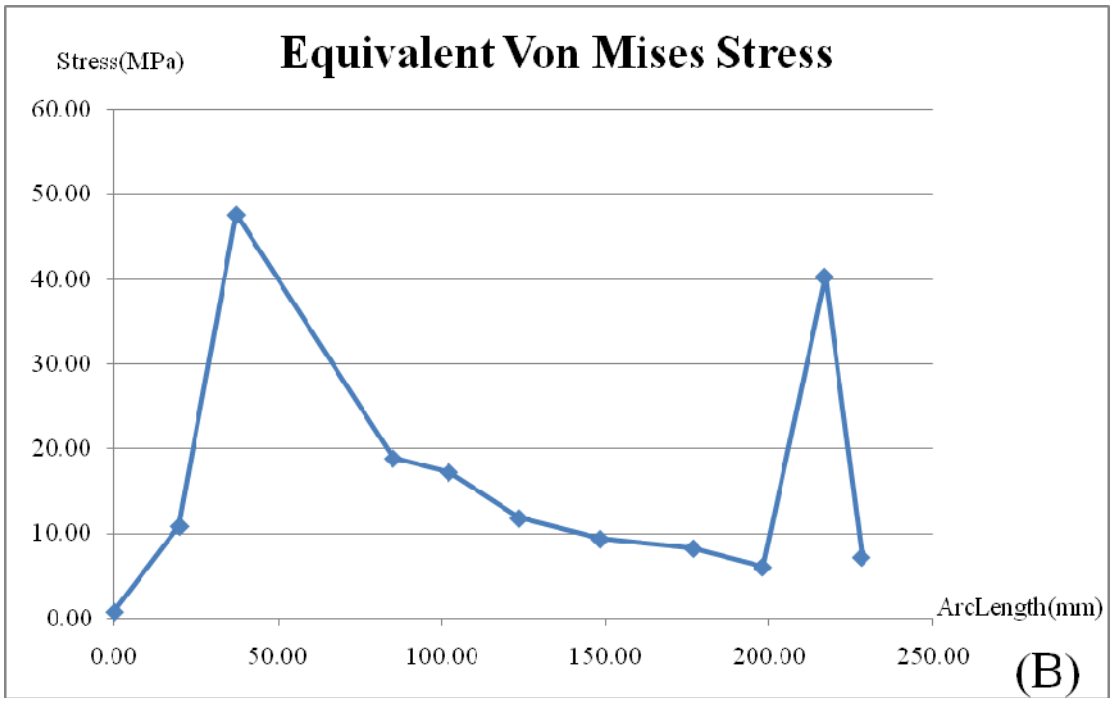

Appendix Figure 41 The Von Mises stress distribution on the standard humeral nail with the retrograde insertion technique and lower gap at ninety degrees abduction: (A) Medial side, and (B) Lateral side.

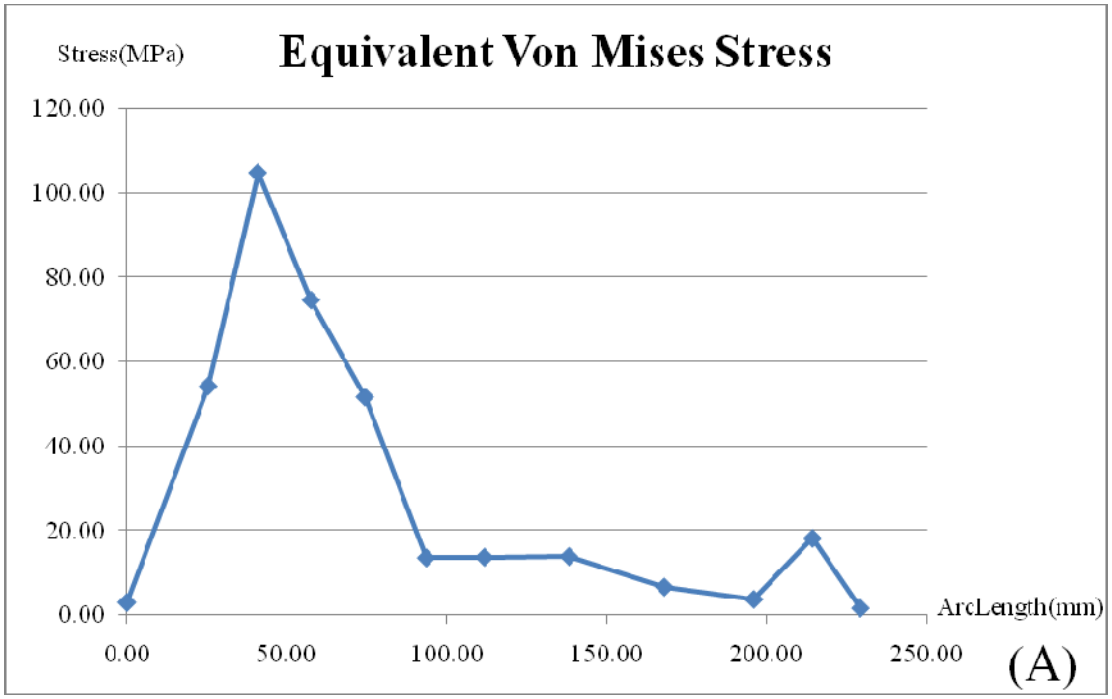

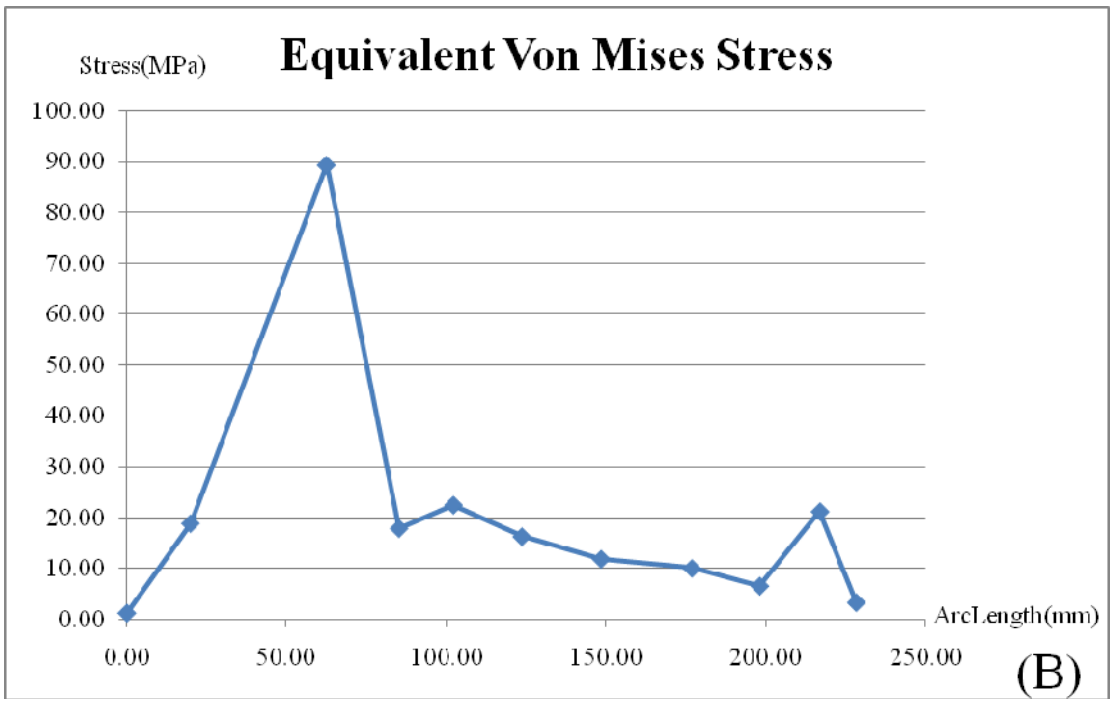

Appendix Figure 42 The Von Mises stress distribution on the standard humeral nail with the retrograde insertion technique and medium gap at ninety degrees abduction: (A) Medial side, and (B) Lateral side.

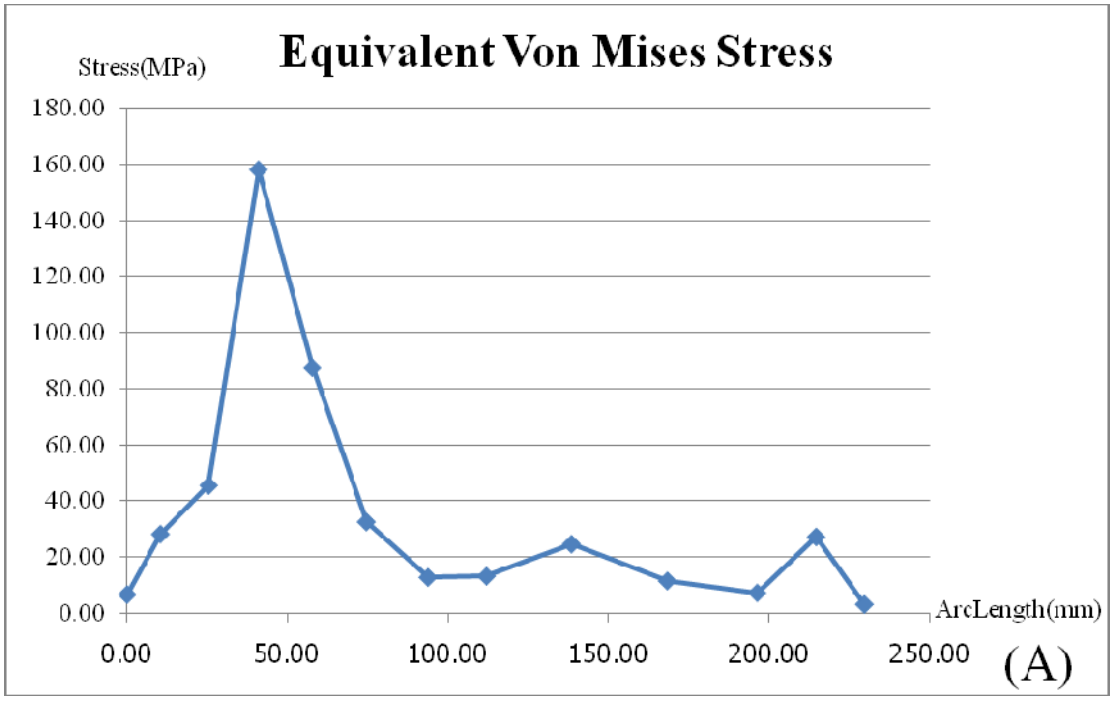

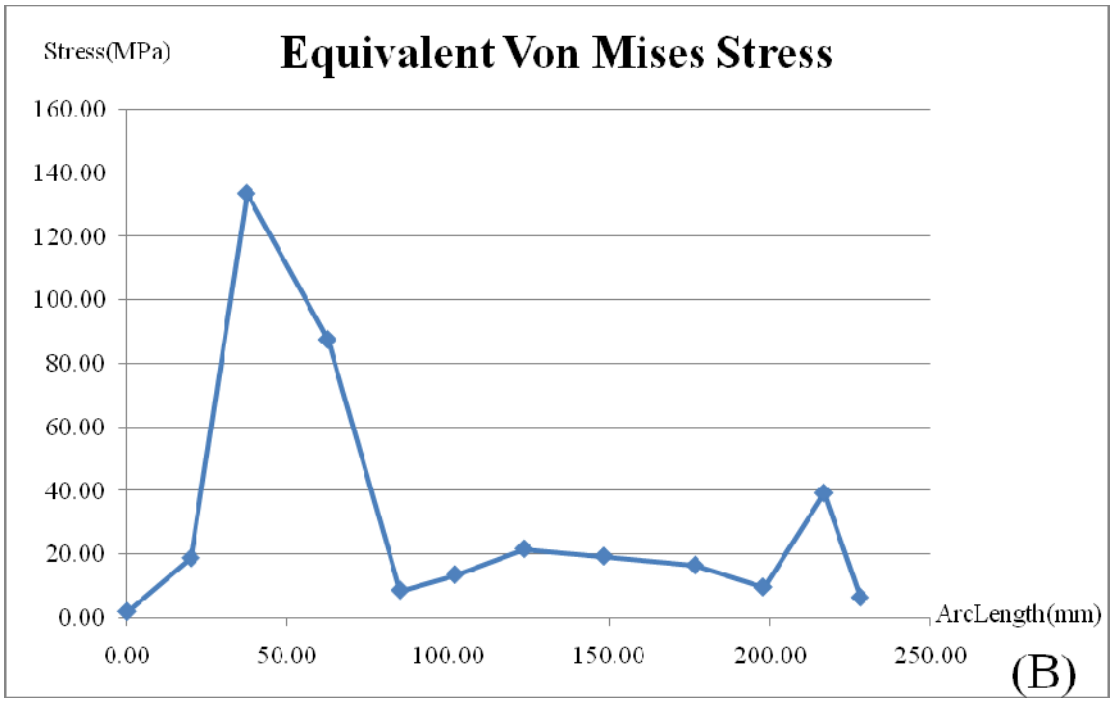

Appendix Figure 43 The Von Mises stress distribution on the standard humeral nail with the retrograde insertion technique and upper gap at ninety degrees abduction: (A) Medial side, and (B) Lateral side.

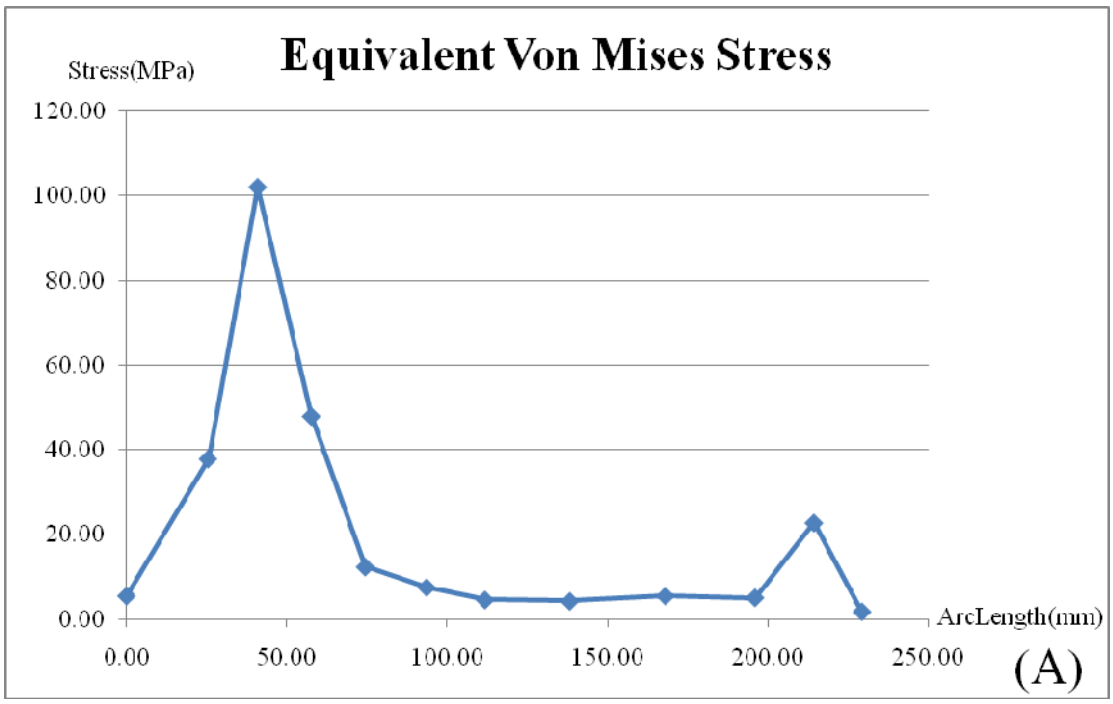

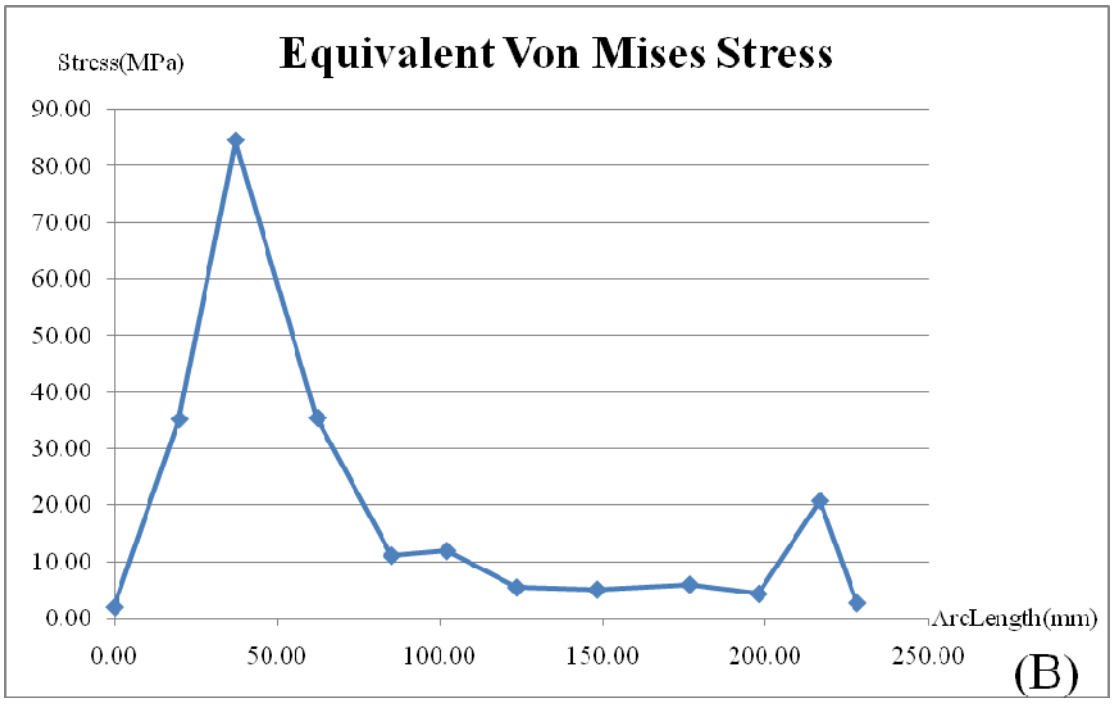

Appendix Figure 44 The Von Mises stress distribution on the standard humeral nail with the retrograde insertion technique and intact at ninety degrees abduction: (A) Medial side, and (B) Lateral side.

CIRRICULUM VITAE

NAME : Mr.Panya Aroonjarattham

BIRTH DATE : April 9, 1976

BIRYH PLAC : Bangkok, Thailand

EDUCATION :

YEAR	**INSTITUTE**	**DEGREE/DIPLOMA**
1998	Mahidol Univ.	B.Eng. (Mechanical Engineering)
2003	Kasetsart Univ.	M.Eng. (Mechanical Engineering)

POSITION/TITLE : Lecturer

WORKPLACE : Mahidol University

SCHOLARSHIP/AWARDS : The financial support for instructor development of information technology campus, Mahidol University